Enhancing Imaging Depth of Handheld LED-Based Photoacoustic Imaging

Master Thesis Biomedical Engineering

Rianne Bulsink

University of Twente
Biomedical Photonic Imaging Group
April 2022

Examination committee:
prof.dr.ir. W. Steenbergen (BMPI)
F. Kalloor Joseph PhD (BMPI)
dr.ir. F. van der Heijden (RAM)

Summary

Handheld LED-based photoacoustic imaging has potential for many pre-clinical and clinical applications, but the imaging depth of approximately 1 cm is a limiting factor. This thesis is aimed to enhance the imaging depth of a LED-based Photoacoustic(PA) system.

For enhancement of the imaging depth, the light delivery into the tissue has been investigated. This is done by investigating the different LED-based illumination configurations of LED arrays used in the PA system, AcousticX (Cyberdyne Inc., Tsukuba, Japan), and simulating the setup of the photoacoustic probe.

With the simulated probe, the optimal configuration for the LED array with respect to the transducer is investigated. This is done for a setup where one LED array is placed on each side of the transducer and also for a setup with 2 LED arrays on each side of the transducer. In every setup, the optimal angle of the LED array with respect to the transducer is determined to find the optimal configuration. Comparing the results, a setup with 2 LED arrays on each side of the transducer, all with an angle of 60 degrees has proven to result in the best light delivery throughout the tissue. These results were validated during experiments and an experiment in chicken tissue showed an improvement in imaging depth from 24 mm with the set up with one LED array on each side, to 29 mm in the set up with two LED arrays on each side.

Next, a new configuration that does not have the limitation of using LED arrays has been investigated. For this, the number of rows with LED elements has been altered and increased from 4 (in the commercially available array) to 10, and a curved array is investigated. The optimal configuration was found to be a configuration with a planar configuration with 10 rows of LED elements, at an angle of 60 degrees with respect to the transducer.

Another way to investigate the possibility that is used is the enhancement of the photoacoustic signal. For this, a deep learning algorithm is trained with two datasets, converted into synthetic photoacoustic images at varying noise levels from 10 to 50 dB. The results are compared to a fluence compensation method. The result shows

that the use of the trained algorithm can improve the visibility of structures in a noisy image with respect to fluence compensation, especially at high noise levels of 10 and 20 dB.

For the validation, a set of experiments were performed, where images from the datasets are converted into a physical phantom. This phantom was imaged in water and a tissue-mimicking medium. The image in the tissue-mimicking medium is tested in the algorithm.

The metric scores are lower for the generated images than from the original images, however, when observing the images, the predicted image is matching closer to the image in the water, and more original structures were observed than the image in the tissue-mimicking phantom solution.

Finally, the photoacoustic system is used to investigate the possibility of blood oxygen saturation imaging using the system with respect to the golden standard oximeter. For this, experiments were executed in a tissue-mimicking phantom, in a mouse thigh, and on a human subject. The results show that blood oxygen saturation imaging using a dual-wavelength LED-based photoacoustic system has potential for use in clinical and preclinical applications. Using fluence compensation in this method improves the accuracy of the blood oxygen saturation levels by 12-15%. The improvement of the imaging depth would be beneficial for the usability of this method.

Samenvatting (NL)

Handzame LED-gebaseerde fotoakoestische beeldvorming heeft potentieel voor vele preklinische en klinische toepassingen, maar de beeldvormingsdiepte van ongeveer 1 cm is een beperkende factor. Deze thesis is gericht op het vergroten van de beeldvormingsdiepte van een LED-gebaseerd fotoakoestisch systeem.

Om de beeldvormingsdiepte te vergroten, wordt de lichtafgifte in het weefsel onderzocht. Dit wordt gedaan door de eigenschappen van LED-arrays te onderzoeken die worden gebruikt in het fotoakoestische systeem, AcousticX (Cyberdyne Inc., Tsukuba, Japan), en door de opstelling van het fotoakoestische probe te simuleren.

Met de gesimuleerde probe wordt de optimale configuratie van de LED-array ten opzichte van de transducer onderzocht. Dit wordt gedaan voor een opstelling met één LED-array aan elke kant van de transducer en ook voor een opstelling met twee LED-arrays aan elke kant van de transducer. In elke opstelling wordt de optimale hoek van de LED-array ten opzichte van de transducer bepaald om de optimale configuratie te vinden. Bij vergelijking van de resultaten is gebleken dat een opstelling met 2 LED-arrays aan elke kant van de transducer, allen onder een hoek van 60 graden, de beste lichtopbrengst in het weefsel oplevert. Deze resultaten werden gevalideerd tijdens experimenten en een experiment in kippenweefsel toonde een verbetering van de beelddiepte van 24 mm met de opstelling met één LED-array aan elke kant, tot 29 mm in de opstelling met twee LED-arrays aan elke kant.

Vervolgens is een nieuwe configuratie onderzocht die niet de beperking heeft van het gebruik van LED-arrays. Hiertoe is het aantal rijen met LED-elementen gewijzigd en verhoogd van 4 (in de commercieel beschikbare array) tot 10, en is een gebogen array onderzocht. De optimale configuratie bleek een planaire configuratie te zijn met 10 rijen LED-elementen, onder een hoek van 60 graden ten opzichte van de transducer.

Een andere manier om de mogelijkheid van de verbetering van het fotoakoestische signaal te onderzoeken, is gedaan. Hiervoor wordt een deep learning-algoritme getraind met twee datasets, omgezet in synthetische fotoakoestische beelden bij variërende ruisniveaus van 10 tot 50 dB. De resultaten worden vergeleken met een

fluentiecompensatiemethode. Het resultaat toont aan dat het gebruik van het getrainde algoritme de zichtbaarheid van structuren in een ruisig beeld kan verbeteren ten opzichte van fluentiecompensatie, vooral bij hoge ruisniveaus van 10 en 20 dB.

Voor de validatie is een set van experimenten uitgevoerd waarbij beelden uit de datasets zijn omgezet in een fysiek fantoom. Dit fantoom werd afgebeeld in water en een weefsel-imiterend medium. Het beeld in het weefselnabootsende medium wordt getest in het algoritme.

De metrische scores zijn lager voor de gegenereerde beelden dan voor de originele beelden, maar bij het observeren van de beelden komt het voorspelde beeld dichter bij het beeld in het water, en zijn meer originele structuren te zien dan het beeld in het weefselnabootsende medium.

Tenslotte wordt het fotoakoestische systeem gebruikt om de mogelijkheid te onderzoeken van beeldvorming van de zuurstofverzadiging in het bloed met behulp van het systeem ten opzichte van de standaard oximeter. Hiertoe zijn experimenten uitgevoerd in een weefselnabootsend medium, in een dijbeen van een muis, en op een menselijk proefpersoon. De resultaten tonen aan dat beeldvorming van de zuurstofverzadiging in het bloed met een fotoakoestisch systeem op basis van LED's met twee golflengtes potentieel heeft voor gebruik in klinische en preklinische toepassingen. Het gebruik van fluentiecompensatie in deze methode verbetert de nauwkeurigheid van de bloedzuurstofverzadigingsniveaus met 12-15%. De verbetering van de beeldvormingsdiepte zou gunstig zijn voor de bruikbaarheid van deze methode.

Contents

Chapter 1

Introduction

The photoacoustic effect or optoacoustic effect is discovered by Alexander Graham Bell in 1880 [1]. In this effect, the absorbance of light causes the generation of a sound wave. He discovered that using a pulsed light source, with using a chopped light beam, the sound is emitted which has the same frequency as the frequency by which the light beam is pulsated. Later, the thermoelastic effect was discovered, where tissue heats due to a short excitation pulse and cools down, rapidly after heating [2]. This heating causes the tissue to expand, resulting in a pressure pulse that can travel through a medium. With these techniques, a new imaging modality has been developed, namely photoacoustic imaging.

1.1 Photoacoustic imaging

In photoacoustics, typically a pulsed laser of the desired wavelength is used as an excitation source to illuminate the tissue. The light propagates through the tissue where it is scattered and absorbed. The absorption of the light causes thermoelastic expansion, resulting in a pressure wave that can be detected using an ultrasound transducer. Optical techniques, like microscopic techniques, cannot reach deep into the tissue, due to the combination of scattering and absorption of light. This limits the imaging depths in these techniques to 1 mm [3]. What makes photoacoustic imaging (PAI) different from many other imaging techniques that use the detection of the pressure waves instead of using light, acoustic scattering is far less than optical scattering resulting in a high resolution imaging at deep tissue with PAI. Due to this, in comparison to other optical imaging techniques, a high imaging depth and better resolution inside the tissue can be achieved. [1]

In photoacoustic imaging, typically lasers are used as excitation sources, where the laser produces pulses of 5-10 ns width, with excitation energy of tens to hundreds mJ per pulse with a repetition rate of around 10-100 Hz.

In PAI a short (ns) light (laser) pulse is used for elimination. Chromophores in the tissue absorb the light and thermoelastic expansion occurs, this expansion generates pressure waves. The pressure wave originating from the absorbing tissue location is detected by an ultrasound probe and a map of the location of these absorptions can be made. PAI has proven to be sensitive to absorption contrast in lipids and hemoglobin in arteries and veins. [4]

With the current techniques, there is no rapid characterization of tissue function and molecular composition. Photoacoustic imaging provides the opportunity for accurate diagnostics. PAI can achieve microscopic (µm) resolution beyond the optical transport mean free path (1 mm) and it can provide structural, functional, and molecular information about tissues.

Photoacoustic imaging uses optical absorbance of tissue for specified wavelengths to obtain an image. With the optical absorbance maps, the presence of components with absorption that corresponds with the excitation wavelength can be explored, which can for example be: hemoglobin, oxy-hemoglobin, lipids, melanin, bilirubin, and water [5] [6]. In photoacoustic imaging, the detection is done using an ultrasound probe, and it is combined with an illumination source like a laser therefore the advantages of acoustic imaging using an ultrasound transducer are combined and the system can give structural, molecular, and functional information of the tissue [3]. Photoacoustic imaging has potential in many fields, due to this, for example; dermatology [7] [8], vascular biology [9] [10], oncology [11] [12], and many more

1.1.1 Signal generation

Photoacoustic imaging uses optical absorbance of tissue for specified wavelengths to obtain an image. The absorbed energy is described as:

$$E_\alpha = \mu_a \, \phi \tag{1.1}$$

Where E_α is the absorbed optical energy, μ_a is the absorption coefficient and ϕ is the light fluence.

The absorbed light generates a pressure wave due to thermoelastic expansion. Pressure generation after the absorption of light is described by the following formula:

$$P_0 = \Gamma E_\alpha \tag{1.2}$$

Where P_0 is the initial pressure and with Γ, the Grüneisen coefficient, described by:

$$\Gamma = \frac{\beta c^2}{C} \tag{1.3}$$

With the thermal expansion coefficient: β, the speed of sound c and the specific heat capacity C

The pressure wave propagates towards the tissue surface, which can be detected using acoustic detectors. By knowing the acoustic properties of the tissue, the location of the absorbing target can be located. A condition for the generation of a pressure wave, originating from a thermoelastic process, is that the light shone on the target has a sufficiently short pulse length. This ensures that the thermal and stress confinement regimes are not exceeded. This means that the pulse duration must be shorter than the time it takes for the mechanical stress to dissipate into the surroundings (the stress relaxation time) [13]. It also must be shorter than the time it takes for energy to dissipate to the surroundings via thermal diffusion. A light pulse duration in the nanosecond range will satisfy both confinement conditions for imaging in biological tissue [1]. Photoacoustic imaging is a very promising technique to non-invasively image biological tissues [14] since it combines the best of both worlds: the high optical contrast of optics and high spatial resolution and relatively large imaging depth of ultrasound.

1.1.2 Detection

The pressure wave that is originating from the absorber is propagating through the tissue and will reach the surface of the tissue where it is detected. The propagating pressure wave is described in the following formula:

$$p(\vec{r}, t) = \frac{1}{4\pi}\frac{\partial}{\partial t}\left(t \int_{|r-\vec{r}|=c_0 t} p_0(\vec{r}) dr\right) \tag{1.4}$$

Where r is the location and t the time.

At the surface, the pressure wave is detected using acoustic detectors. Piezoelectric materials, placed in an ultrasound transducer are used to detect the pressure wave. An ultrasound transducer has multiple elements containing piezoelectric materials, which obtain a profile that can be used to determine the size and the location of the absorber when the properties of the medium are known. How the time-dependent signal received by the transducer elements are reconstructed is shown in figure 1.1 [15]. The image reconstruction used is, described in Jaeger et. al. [16] which uses a Fourier method for transforming the time-dependent signal into an image. The signal is transformed from the space-time domain to the spatial-temporal

frequency domain:

- Rearranging Fourier coefficients using the wave vector mapping law, transforming frequencies into vectors.
- With inverse Fourier transformation, the data is transformed back to the spatial domain.
- An imaging line is reconstructed for each element and to reduce the artifacts, the data is zero-padded in all directions.

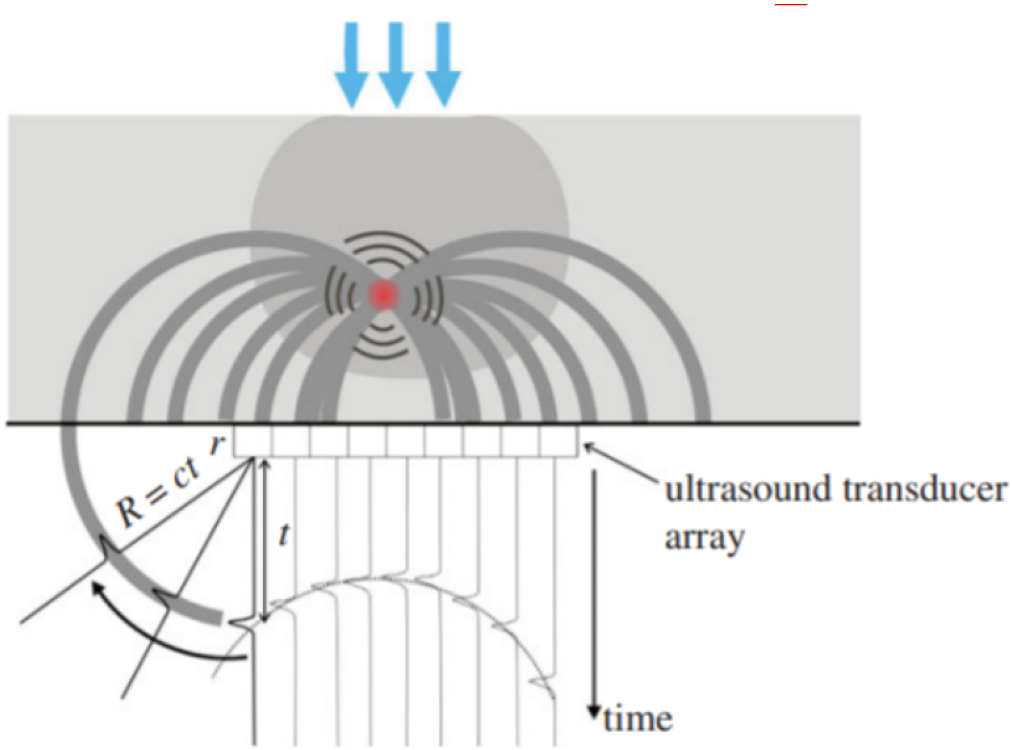

Figure 1.1: Image reconstruction method of the signal originated from an absorber, detected by an ultrasound transducer with piezoelectric elements to detect the pressure wave [15].

1.2 LED based photoacoustic imaging

The use of lasers in PAI does have some limiting factors for the transition from the laboratory to a clinical setting. Lasers are bulky, expensive, high maintenance and many safety concerns come with the use of them. An alternative for the use of laser as an excitation source is the use of Light Emitting Diodes (LEDs). [17] [18]
With the use of pules lasers, high energy pulses (mJ) with a short pulse duration (ns)

are used, with the uses of LEDs for excitation, these energies are much lower (µJ). Due to the lower excitation power and higher signal-to-noise ratio (SNR) averaging of multiple frames is done to obtain a better SNR. This is possible because LEDs have a higher repetition rate of around 16 kHz, a lower excitation energy decreases the penetration depth. For LED-based imaging, a penetration depth of 10-15 mm is found [3]. Higher depths of 25- 32 mm with strong absorbers can also be found in literature [18]. In LED-based PAI the Axial resolution is 268 µm and the lateral resolution is 550-590 µm. This could be improved with decreasing pulse width and higher frequency ultrasound transducers. [18]

1.3 Potential applications

1.3.1 Carotid artery

With annual mortality of about 5.5 million, stroke is the second leading cause of death worldwide. Not only the lethality numbers are high, but also the impact on the survivors is high. 50 % of the survivors are chronically disabled due to a stroke [19]. There are 2 categories of strokes, hemorrhagic stroke, and ischemic stroke. Hemorrhagic stroke is caused by the rupture of a blood vessel while with an ischemic stroke the blood supply is interrupted by a cloth for example. Ischemic strokes represent about 80% of all strokes. [19]

A risk factor of ischemic stroke is carotid artery disease. The carotid artery lies on each side of the neck and supplies oxygen-rich blood to the head from the external carotid artery and oxygen-rich blood to the brain from the internal carotid artery. In carotid artery disease plaques are built up inside of these arteries, which can hamper the blood flow. Carotid artery disease can cause ischemic strokes, in which the blood flow to the brain is cut off. Within a few minutes of blocked blood flow, the tissue starts to die, this can cause (severe) brain damage or death. The carotid artery affected by atherosclerosis shows the degradation of the collagen structure, thickening of the intima, and formation of complex plaques. Carotid artery disease is a major cause of strokes, hardened plaques narrow arteries, hampering the blood flow to the head. [20]

Also, blood clots formed in the carotid arteries can be the cause of a stroke. If the plaque in an artery ruptures or cracks, platelets stick to it and may form a blood clot by clumping together. When a plaque or a blood clot breaks away from the wall, this can travel through the bloodstream and block one of the smaller arteries in the brain, causing a stroke. [21] [22]

With the suspicion of carotid artery disease, the doctor start with examining the

medical history and listening to the carotid artery for a whooshing sound called a bruit, which may indicate reduced or changed blood flow. For diagnosing carotid artery disease, carotid ultrasound (sonography) is most used. Standard, US shows the structure of carotid arteries, Doppler shows the blood flow trough arteries. When the ultrasound does not give enough information, carotid angiography can be used. For this, contrast is injected in the veins and an X-ray, CT, or MRI scan is taken [21]. Most procedures for the treatment of stenosis in the carotid artery, stenting and removing of the plaque, are ultimately unnecessary. The composition of the plaque can give the necessary information to determine the risk factors attached to it. [23]

Photoacoustics can give structural, molecular, and functional information of the tissue [3], which can provide the information of the plaque, resulting in better treatment. The limiting imaging depth and relative high Signal to noise ratio are limiting factors with imaging of the carotid artery because the carotid artery is at a depth of 23.5 +/- 6.9 mm from skin [24]. Therefore, there is a need for the improvement of the imaging depth in PAI for imaging of the carotid artery.

1.3.2 Breast cancer

Breast cancer is one of the most occurring forms of cancer with 11.7 % of the total diagnosed cases in 2020, which is equal to 2.3 million incidences [25]. Detection plays an important role in the detection and treatment. [26]. In breast cancer imaging, different modalities are used, namely x-ray mammography, MRI, and ultrasound. X-ray mammography is the technique that is most often used [27], but it also has disadvantages. This technique uses ionizing radiation and is not optimal in the sensitivity and specificity of the detection of a tumor. For the patient, it is also not ideal. the breast is placed between two plates and this is painful for women, while in a woman with a large breast the imaging quality is limited. Ultrasound provides structural and morphological information in real-time with a good resolution, but this technique is highly dependent on the operator and the rate of false positives is relatively high [28]. In the use of MRI, a contrast agent is used to examine the vasculature in the breast. MRI provides high resolution but there are contrast agents required in the use and the technique is expensive with low specificity [29]. Early detection for breast cancer is important for the treatment process, a relatively low cost and widely available breast scanner with high specificity and sensitivity is therefore desired. A system that can be used with low resources can have a big effect on the treatment of breast cancer globally [30]. In cancers, the tumor can grow blood vessels to sustain itself, which causes a characteristic of tumors. Therefore in and around tumors, high density of blood vessels and low blood oxygen saturation levels can be observed [31]. Pho-

toacoustic imaging offers the possibility to use the optical properties of hemoglobin and oxy-hemoglobin to investigate the vasculature in a breast with a relatively high imaging depth and the resolution similar to that in ultrasound [32]. Therefore breast cancer imaging is a highly interesting application for the use of the photoacoustic system [33].

Chapter 2

Research Question

The main objective of this thesis is to enhance the imaging depth for a handheld LED-based photoacoustic imaging system. By enhancing the imaging depth, the LED-based photoacoustic imaging can be used for a wider range of applications [3] [34]. For the improvement of imaging depth, different routes can be taken, namely software or hardware improvements. This thesis focuses on the improvement of the hardware, where the configuration of the setup is evaluated and improved to enhance the imaging depth. Afterward, a method for signal enhancement will be investigated using a algorithmic approach.

LED based PAI has the advantage of the use of LED instead of laser. The use of LED decreases the cost and there are no safety measures needed as there would be with the use of LASER. but with the use of LED the signal to noise ratio deeper in the tissue decreases and improvement of this is necessary. The improvement of imaging depth for LED-based photoacoustic imaging(PAI) will be the focus of this project. The main research question is:

- Can the imaging depth for LED-based photoacoustic imaging be increased?

This problem can be viewed from different sides, hardware, and a software approach.

Due to scattering and absorption in the tissue, the light for excitation does not penetrate deep into the tissue and the amount of energy absorbed by the tissue to produce a pressure wave is reduced deeper in the tissue. This is a limiting factor in LED-based PAI. By increasing the number of LED arrays for excitation, a higher fluence deeper in the tissue might be obtained resulting in an improved imaging depth.

Research questions for the hardware approach are:

- Can the imaging depth of a LED-based photoacoustic system be improved by altering the illumination of the setup?
  - Do multiple LEDs used for excitation increase the imaging depth?
  - What would be the best configuration for the LEDs?

The imaging depth can also possibly be improved during post processing using algorithmic approach. With this, the PA image obtained from an acquisition in combination with the corresponding ultrasound image can be used to increase the imaging depth. Therefore research questions for a software approach are:

- Can the imaging depth be increased by software-based solutions?
  - Deep learning concerning: Can a deep learning algorithm be trained to detect signals from deeper in a photoacoustic image and with that improve the imaging depth of a LED-based photoacoustic system?

2.1 Thesis overview

This thesis will first focus on optimizing the light delivery of the the photoacoustic imaging system. In chapter 3, a LED array that is used in a LED-based photoacoustic imaging system is analyzed to determine the characteristics of this LED array. In chapter 4 this LED array is modeled using Monte Carlo simulations [35] [36] and a model of the PAI setup is created to find the optimal angles and investigate the influence of multiple LED arrays. In chapter 5, the results of the simulations will be validated in an experimental setup and in chapter 6 a new configuration for the PAI probe is investigated.

For the investigation of the possibility for the enhancement of the PAI information using deep learning, experiments with two datasets are performed in chapter 7. Chapter 8 research for the use of photoacoustic imaging for blood oxygen saturation is described.

Chapter 3

LED characterization

In this chapter, a LED array that is used in a LED-based photoacoustic imaging system is analyzed to determine the properties of this LED array. This is done as a base to use the properties to simulate a LED array in the following chapters, to enhance the imaging depth.

3.1 Background

The aim is to enhance the imaging depth in LED-based Photoacoustic Imaging (PAI). One method for enhancing the imaging depth is by investigating the influence of the illumination configuration on the light distribution inside the tissue. This influence of illumination may guide a route for the enhancement of the imaging depth. To investigate the possible enhancement of the imaging depth in LED-based PAI a model of the PAI setup is created, so this setup can be altered to allow efficient investigation of a range of configurations.

For Modeling the PAI set up in the following chapters, Monte Carlo Simulations(MCXlab) [35] [36] is used, where LED arrays are simulated and placed in a configuration, similar to the set up in the photoacoustic system. In the set up of the photoacoustic system, two LED arrays are placed, one on either side of the transducer, shown in figure 3.1

In this chapter, experiments with a LED array are performed, so the properties of the LED array are investigated and can be implemented in simulations of a photoacoustics system. This simulated LED element will be used in later simulations to investigate the possibility for enhancement of imaging depth.

Figure 3.1: The set up of the photoacoustics probe, where two LED arrays are placed, one on either side of the ultrasound transducer.

3.2 Method

The system used in this thesis is the LED-based PA imaging system: AcousticX (Cyberdyne Inc., Tsukuba, Japan). A LED array used in the photoacoustic setup, is shown in figure 3.2 and 3.3. One LED array has 4 rows of 36 LED elements. The used LED array has a wavelength of 850 nm, other wavelengths are also possible to use, which can be chosen dependent on the preferred optical spectra. In MATLAB, Monte Carlo simulations(MCXlab) [35] [36] are used to create a model of a single LED array. LED arrays are used in these simulations, therefore the properties of a LED array are investigated during experiments, to make sure the simulations match with reality and are representative.

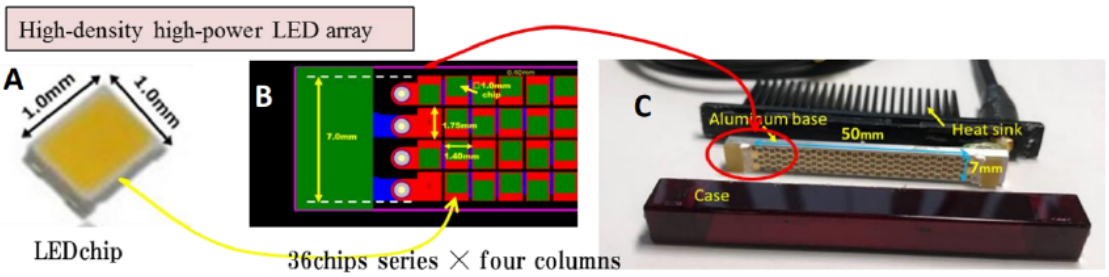

Figure 3.2: High-power LED array which is used in the set up of of the LED based photoacoustics system, existing of four columns with 36 LED chips embedded in a casing [37].

For the quantification of the characteristics of the LED array, different experiments were performed. The properties which are used to compare the simulations

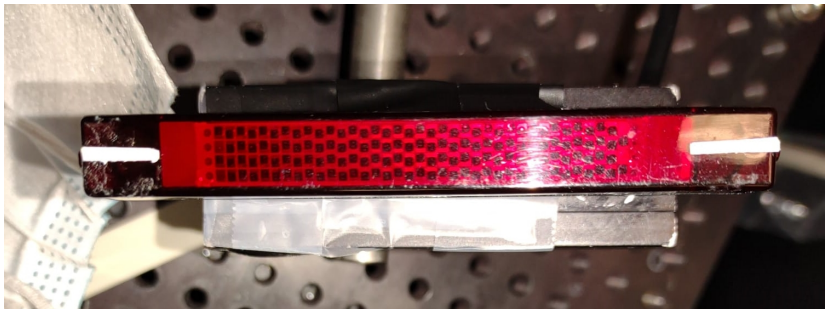

Figure 3.3: High power LED array which is used in the photoacoustics set up. The LED chips are clearly visible.

with the physical LED array are the opening angle, the decay of signal intensity of the signal over distance, and the beam profile. With these results, the optimal values in the simulations will be determined in the following chapter.

3.2.1 Beam profile

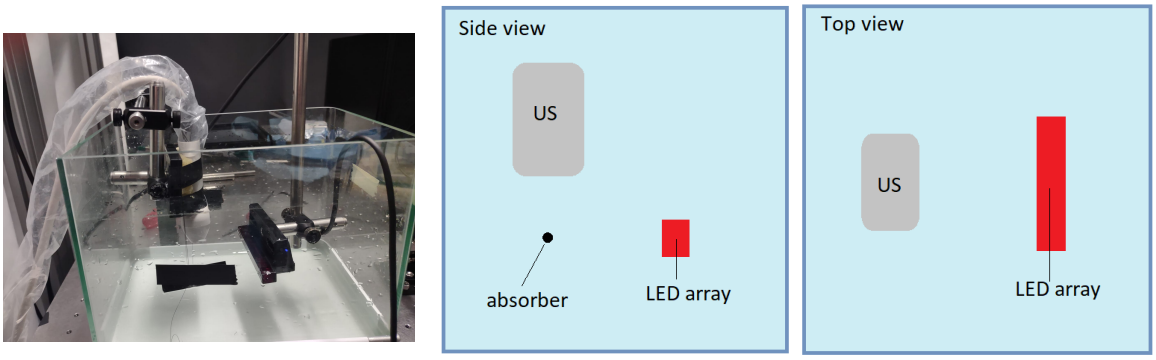

(a) *(b)*

Figure 3.4: (a) Set up to determine the beam profile of the LED array. (b) Schematic of the set up for determining the beam profile of the LED array, where the LED illuminates the absorber.

For determining the beam profile, the setup shown in figure 3.4 was used. A surgical thread (vetsuture, black nylon, USP 4/0 metric 1.5), which is used as the optical absorber, is placed in a tank filled with water. An ultrasound transducer (linear, 128 elements, 7 MHz) is used to detect the signal originating from the thread. The transducer is placed above the surgical thread, with the transducer placed so the thread is located in the focus of the transducer, at a distance of 15 mm. A LED array is placed parallel to the thread and perpendicular to the imaging plane of the transducer. This LED array is mounted on motors (Kinesis, ThorLabs, USA) to move them with precision, with an error of up to 0.003 mm. The LED array can be

moved towards and away from the thread and upwards and downwards, parallel to the imaging plane.

The LED array illuminates the surgical thread, resulting in a photoacoustic signal obtained by the transducer. This photoacoustic signal is obtained and the signal of the center of the thread is used to determine the Intensity of the signal used in the analysis of results. During the measurements, the LED array is moved upwards and downwards, parallel to the imaging plane, with steps of 2.5 mm and away from the transducer in steps of 5 mm. In this way, a grid is measured, in which the profile of the light intensity at different locations of the LED array is obtained.

In the same way, a profile of the illumination of the LED array on the absorber can be obtained from a set distance. The LED array is placed at a set distance from the absorber and the LED array is moved up and downwards, parallel to the imaging plane, with steps of 2.5 mm to obtain a profile of the light originating from the LED array.

Another important factor that is investigated is the change of intensity of the signal over distance, especially to enhance the imaging depth. With the same setup and experiment as described above, the signal intensity change over distance can be determined. This measurement is done by doing measurements with the LED array perpendicular to the imaging plane at the exact height of the absorber and moving the LED array away from the absorber with steps of 5 mm and doing measurements until a distance of 35 mm is reached.

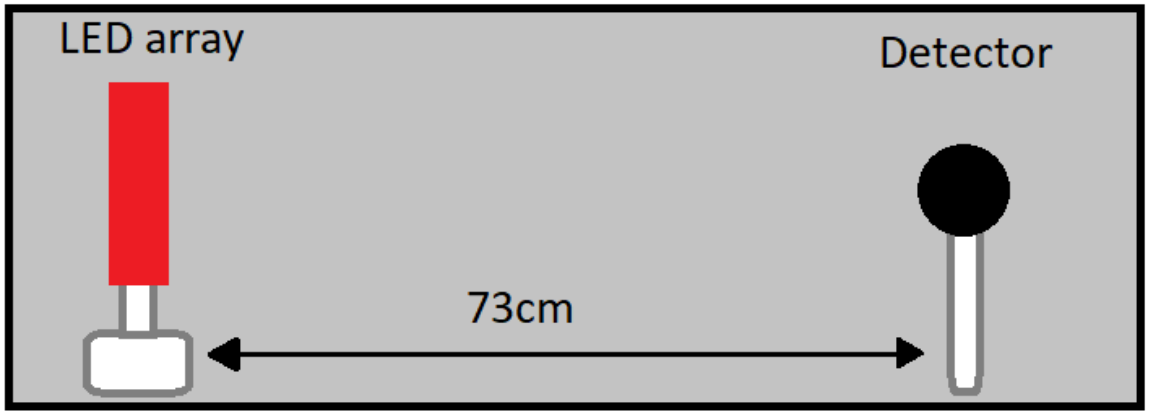

Figure 3.5: The set up used to measure the opening angle of LED array, the LED array is placed in a turnable circular stage, a S121C Si photodiode is placed on a distance of 73 cm from the center of the LED array.

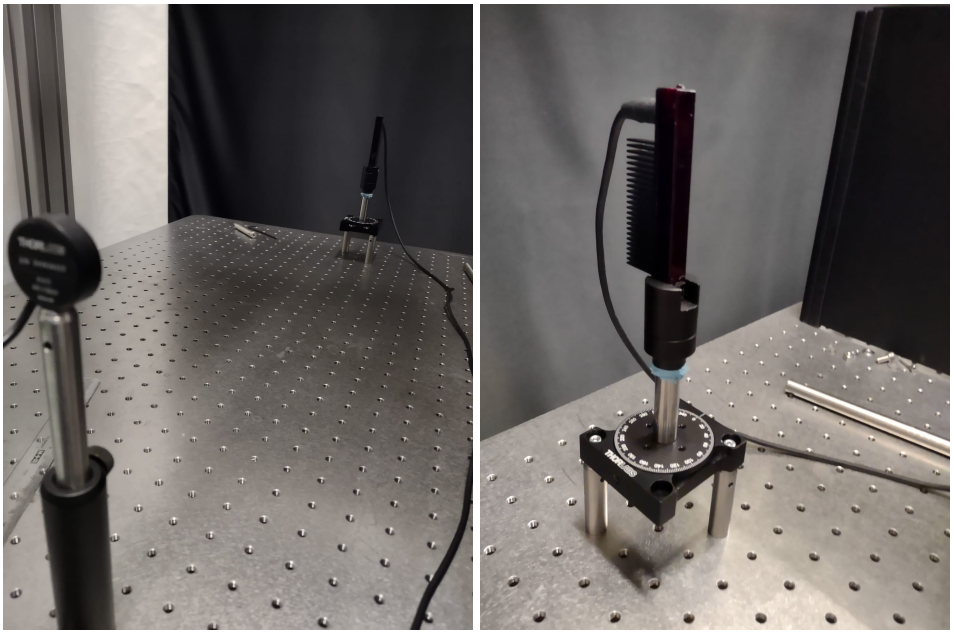

(a) *(b)*

Figure 3.6: For determining the opening angle, the LED array is placed in a circular stage which can turn. A S121C Si photodiode is placed at 73 cm from the LED array.

3.2.2 Opening angle

For measuring the opening angle of the LED array, a different setup was used, shown in figure 3.5. This experiment was executed for a reliable measurement of the opening angle. The experiment is executed in air, due to the spatial limitations in a water tank. The mismatch in refractive index is also investigated in the model in later comparison because the model should work in different media. In this set up the LED array is placed in a holder which can turn 360 degrees, shown in the figure 3.6. A S121C Si photodiode power sensor (ThorLabs, USA) is placed at 73 cm from an LED array at the height corresponding with the height of the center of the LED array, as shown in figure 3.6. The LED was rotated in steps of 10 degrees from -120 to 120 degrees and the incoming light of the LED array was measured with the photodiode, the setup is placed in a dark room.

3.3 Results

3.3.1 Beam profile

Using the setup in the water tank, a profile of the signal intensity of the photoacoustic signal originating from the LED array is obtained. The beam profile is shown in

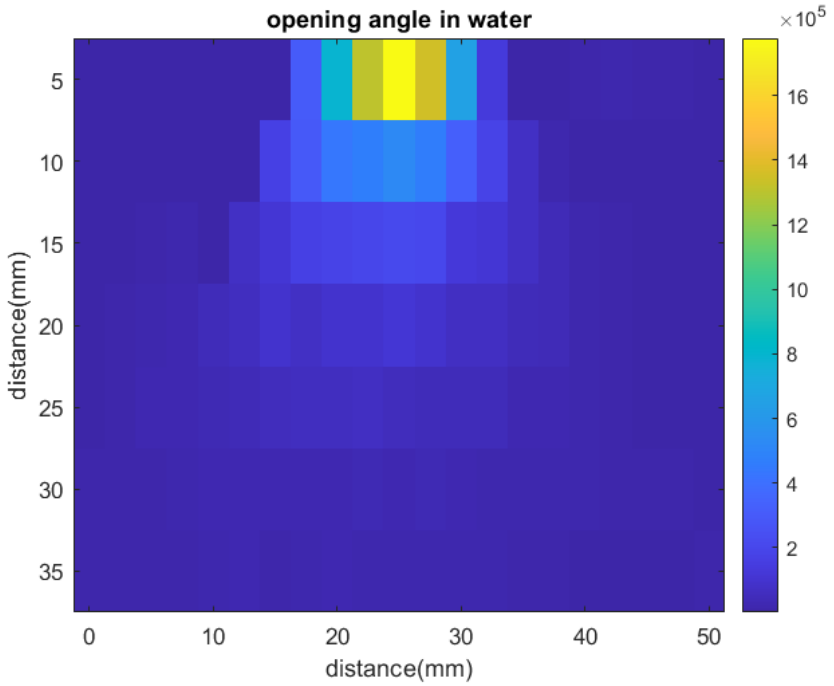

Figure 3.7: Opening angle of the LED in water, the LED array is places at the top, with the small side of the LED in the plane.

figure 3.7. The LED array is placed at the top, with the center of the LED array in the middle at 25 mm.

Placing the LED array at a depth of 20 mm from the absorber, a profile of the beam is obtained, shown in figure 3.8. The center of the LED array is located in the middle at 22.5-25 mm. It can be observed that the peak of the signal intensity is located at the center, between 20 mm and 27.5 mm. The peak in the signal intensity corresponds with the location of the LED array in the setup. The shape of the profile is close to what could be expected; namely a broad high signal at the center, where the LED array is placed. This originates from the shape of the LED array, where multiple LED chips in the LED array result in an illuminating surface instead of a point source. In the center of the high signal, a dip can be observed, this dip is not as would be expected, but might be explained by measurement inaccuracies.

In figure 3.9, the change of signal intensity with distance is displayed. The signal intensity is measured while moving the array away from the absorber in 5 mm steps. The signal originating from the absorber is decaying, which is expected. The light originating from the LED array is divergent and is propagating through a large area, therefore the further away the absorber is placed, the less light is reaching the surface of the absorber.

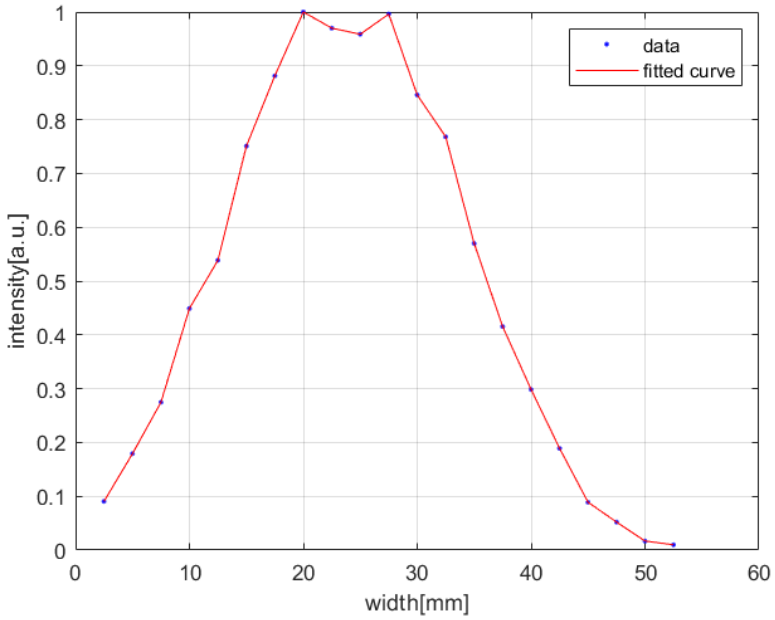

Figure 3.8: Beam profile of the absorber illuminated by the LED array placed 20 mm from the absorber.

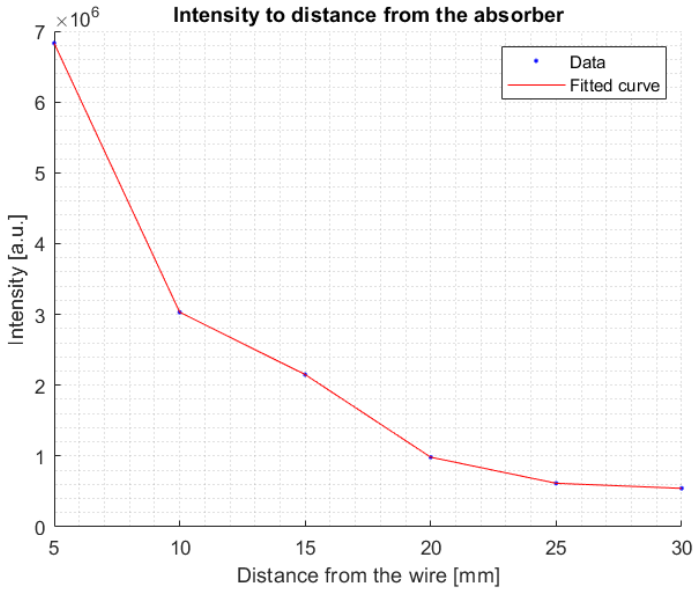

Figure 3.9: The line profile of photoacoustic signal intensity of the absorber, where the LED array is moved away from the absorber, showing the fluence decay over distance.

3.3.2 Opening angle

Of the final experiment for determining the opening angle, the measured signal is shown in figure 3.10. Two measurements were performed, the first from 0 to 120

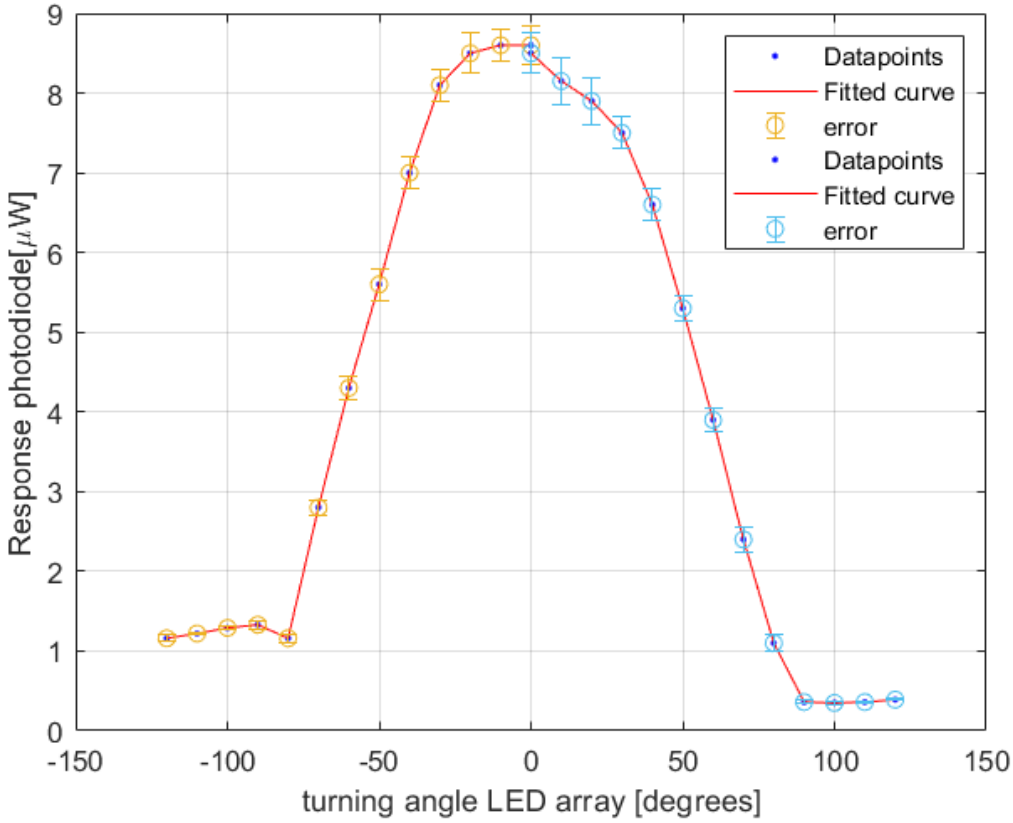

Figure 3.10: The signal detected by the photodiode by measuring the opening angle of the LED array in air. The LED array is placed 73 cm from a photodiode and is rotated.

degrees, the second measurement from 0 to -120 degrees. The left side of the measured signal intensity is slightly higher, this originates from a white curtain located left of the transducer, while on the right side there was no reflector. The signal is not returning to 0, because the darkroom was not completely dark and still some light was present. For comparison to the simulations in the following chapters, the Full-Width Half Maximum (FWHM) was determined to be: 22.5 degrees

3.4 Conclusion

In this chapter, the results of experiments with a single LED array in water and air are shown. The LED array has an opening angle with a FWHM of 22.5 degrees of the beam profile. A decay of signal intensity measured at the absorber has decreased with a factor of 7 from 5 to 30 mm for m the LED. The results of the experiment are under influence of noise and external factors which may have influenced them, therefore a 100% match of the results to the actual values is not to be expected.

Chapter 4

Monte Carlo based modeling of the LED illumination

In this chapter, simulations model of a photoacoustics setup are created. The parameters obtained from experiments in chapter 3 are used to create the representative in chapter 3 are used to create a representative model of the LED arrays. With the use of multiple arrays, the photoacoustics probe is mimicked and the best configuration of LED arrays is investigated for a set up with two LED arrays and four LED arrays to investigate the possibility of enhancing the imaging depth.

4.1 Method

4.1.1 Model of LED array

For enhancing the imaging depth, the influence of a change in the configuration of the illumination of the tissue is investigated. To investigate the influence of changes of the illumination set up, a model of the PAI setup is created, using Monte Carlo Simulations [35] [36]. In the Monte Carlo simulations, the LED arrays are simulated and validated. When a representative configuration is found, the simulated LED arrays are placed in a configuration, similar to the setup in the photoacoustics system.

In this chapter, a model of the photoacoustics setup is created and this will be simulated and adjusted so the simulations correspond with the experiments, in the previous chapter. When a good model of a LED array is obtained, position and angle of the illumination will be varied to obtain the best imaging depth, mimicking a photoacoustics setup so this can be altered to investigate the possible enhancement of imaging depth.

A model of a LED array is created using Monte Carlo simulations in MATLAB, MCXLAB. Monte Carlo simulations, simulate the path of the photons and use this to determine how the light behaves inside a medium. The light source is defined to be

the LED array, mimicking the LED array used in the experimental setup.

When simulating light propagation in photoacoustics set-ups, the light source is thoroughly defined. In the simulations used, the LED array is defined as the exact number of LED elements as individual sources, located in the same positions as in the physical LED array. One array consists of 4 rows with 36 LED elements, so one array has 144 separate LED elements. The LED elements are placed with the distances shown in figure 4.1, resulting in the simulation of an entire LED array, shown in figure 4.2a. The total number of photons, emitted power, and wavelength used in each simulation, shown in table 4.1 is set before executing the simulation.

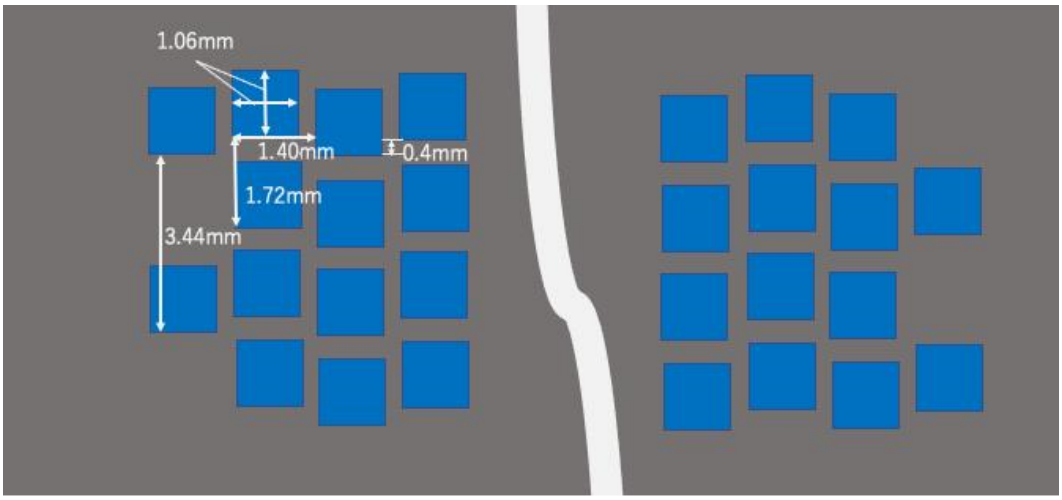

Figure 4.1: Dimensions and locations of single LED elements inside the LED array.

A LED array does not only consist of LED elements, but a casing is surrounding the LED array. Therefore, a surrounding of the LED array is simulated by placing the LED elements in the geometry, with a surrounding mask mimicking the casing, the geometry is displayed in figure 4.2. The LED casing consists of a mask of 1.0 x 1.0 x 8.5 cm, which corresponds to the dimensions of the LED array used in the experiments. The mask of the LED array consists of two layers, a base layer in which the LED elements are placed and an absorbing layer at the back of the LED array, behind the LED elements to prevent unwanted reflections. Around the casing a medium with the preferred optical properties, described in table 4.2, is placed with an absorber, for example, a line absorber as used in the experiments in chapter 3.

The area that is simulated has dimensions of 6.5 x 6.5 x 4.8 cm, which in pixels is: 878 x 878 x 647 pixels, with a pixel size of 74 μm. This pixel size corresponds to the resolution that is reached with the ultrasound transducer, used in the experiments. The values displayed in table 4.1 are used as an input in the model.

Inside the entire geometry, the simulated LED array is placed and the position of the arrays can be adjusted to any location in the geometry. Furthermore, the LED array can be turned to obtain the angle preferred in the research.

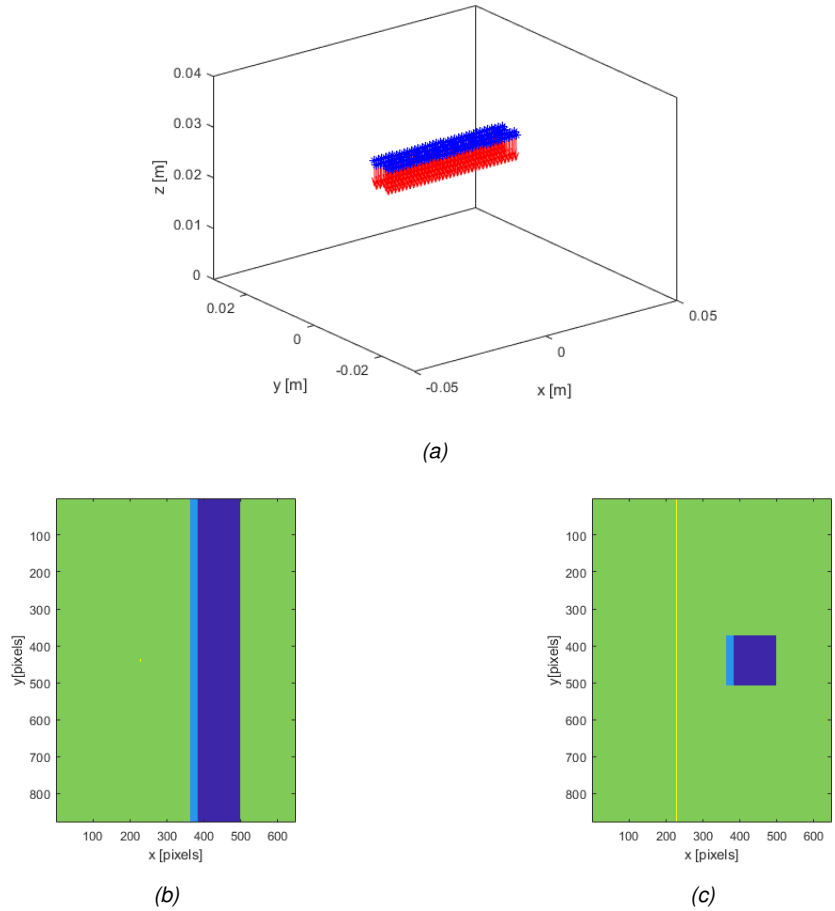

Figure 4.2: Simulation setting: (a) location of the LED elements (blue x) with the direction it is pointing to (red arrow), (b) showing side view of the LEDs (blue) and (c) top view, with the casing (light blue) with the medium having water properties (green) and an absorbing wire (yellow).

4.1.2 Set parameters and verify created model

The created model of the LED array needs to closely match the LED array that is used in a photoacoustics system, to create a reliable model of which the results would correspond with experimental results. For the verification of the model and the fine-tuning of parameters, the experiments in chapter 3 are modeled in simulation using Monte Carlo simulations and the results are compared.

The simulations using 1 LED array are performed, to determine the best settings of the light sources. The decay of light fluence over distance is important for the

Table 4.1: Values used in the simulations

Spatial resolution [μm]	74
Pixels x direction	878
Pixels y direction	647
Number of photons	1e6
Laser power[J]	1e-6
Tomography radius[m]	3.8e-2
Opening angle [$\circ$]	120

comparison of the simulated LED array to the physical LED array. The decay of fluence is one of the most important factors when determining the best setup for increasing imaging depth.

For the first experiment, done in the water the situation of the experimental setup is mimicked in the simulations. An absorber, mimicking the line absorber used in the experimental setup is placed in the configuration, shown in figure 4.2, where the LED array is placed in the configuration, perpendicular to the line absorber, surrounded by water. The LED array illuminates the absorber and the information of the fluence profile is used to compare with the results obtained during the experiments in a similar way. This comparison can be done because in photoacoustics the absorbed light is converted to a pressure wave and detected using the ultrasound transducer. The two parameters are therefore directly linked to each other.

With this set up the line absorber is moved away from the LED array from 5 mm to 30 mm with steps of 5 mm, similar to the way the measurements were done in the experiments in chapter 3. The signal from the center of the absorber will be used to obtain a profile of the fluence over distance, which will be compared to the experimental data. Furthermore, the fluence over the absorber will be used to compare the beam profile from the simulation with the beam profile obtained in the experimental setup.

For the final experiment, where the opening angle was investigated, the setup will be mimicked as well as possible in the simulated configuration. The LED array is placed in a surroundings with the properties of air. The absorber will be placed in the configuration and the LED array is placed as far as the configuration allows it from the absorber, which is 30 mm. This distance is far shorter than the 73 cm used in the experimental setup, however, because the simulations do not have external factors influencing the results, the accuracy of a bigger distance in the simulations should not make much difference, except for the relative size of the detector. The LED array in the simulations will be turned from -100 to 100 degrees with steps of 10 degrees, and the signal from the center of the absorber will be obtained to compare

the results with the results from the experiment.

The main variable that needs to be determined within the model is the opening angle in degrees in which the LED elements sent out the light. With these simulations, the optimal opening angle is investigated.

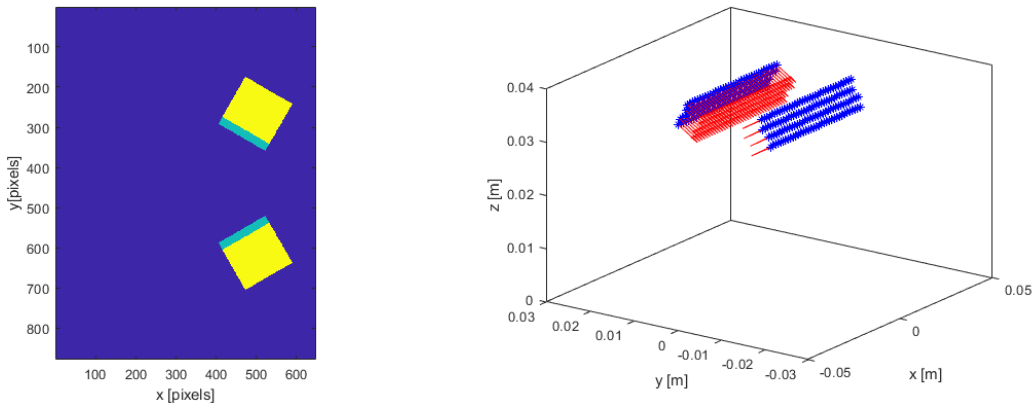

(a) *(b)*

Figure 4.3: The set up used during the simulations of the 2 LED array set up. (a) The configuration used in the two LED array set up with the different masks used, with blue: surrounding tissue, green: base mask of the LED array, yellow: absorbing mask of LED array. (b) The LED elements, which are located in the green part of the configuration in a.

When the best variables are found for the LED array simulations, to resemble the LED array used in the PA system, the optimal configuration is investigated. In the PAI system, two LED arrays are placed, one on each side of the transducer. During the simulation of the PAI system, the LED arrays are implemented in the model in the same configuration as they would be in the photoacoustic setup. The LED arrays are placed 14 mm apart, so an ultrasound transducer would fit in between the arrays. The US transducer is not implemented in the simulations because only the light delivery is investigated. In the simulations mimicking the PAI setup, the optimal angle of the LED arrays with respect to the transducer is investigated by altering this angle. The simulated probe is placed in the geometry containing tissue-mimicking properties, shown in table 4.2, and the signal from the center of what the imaging plane would be, is obtained and used for investigating the optimal angle to obtain the best light delivery at a deeper depth.

The experimental setup of the photoacoustics system is mimicked with the simulations with 2 LED arrays, shown in figure 4.3. The LED arrays with the settings as found for 1 LED array are used. They are placed next to an imaginary ultrasound probe, which has a width of 1.4 cm. The LED array is placed so the inner side of the LED array touches the side of the ultrasound transducer.

4.1.3 Simulate PAI system with additional LED arrays

After the optimal angle of the setup with the two LED arrays is found, two more LED arrays are implemented into the model. The model of the single LED array is duplicated and the LED arrays are placed so the edge of the outer LED array touches the casing of the inner LED array which is placed next to the transducer, at 14 mm appart, at 38 mm from the bottom of the configuration. The angles of the arrays with respect to the transducer can be altered so different set ups can be simulated. In this way, the arrays are always placed next to each other, with the illuminating side of the LED aligned. In the simulations with the four LED arrays, the optimal angle is investigated by varying the angle of the LED array, similar to the previous setup.

First, the angle with respect to the transducer of the LED arrays is altered and the LED arrays on one side of the transducer are kept parallel to each other, to find the optimal angle for the highest light distribution at a greater depth.

Next, the angle of the first set of LED arrays, closest to the transducer, is different from the angle of the second set of LED arrays. This is done because possibly a focus can be created using two different angles. Using a geometric approach (appendix) the angles with the potential to improve the imaging depth are chosen and tested in the simulations. From the simulations, the optimal configuration for improvement of the imaging depth will be determined.

The simulations are preformed is a medium of tissue-mimicking properties, which are the same as used in the simulations before. The optical properties of the materials used in the simulations can be found in table 4.2

Table 4.2: Optical properties used in simulations.

	Absorption coefficient $\mu_a[mm^{-1}]$	Scattering coefficient $\mu_s[mm^{-1}]$	Anisotropy $[g]$	Refractive index $[n]$
Surrounding	1	0	1	1.33
Tissue	0.03	0.667	0.99	1.33
Water	10e-10	10e-10	0.99	1.33
Casing	10e-10	10e-10	1	1.5
Back Casing	100	10e-10	1	1.5

The last type of simulations preformed, are the simulations of the 4 LED arrays, with two different angles, where a layer of water is placed between the transducer and the tip of the LED elements. This is done because during measurements, sometimes the tissue will not fit between the LED arrays but only below it, so a coupling medium will be used between the tissue and the ultrasound transducer. To mimic this, a layer of water is used in between the LED arrays.

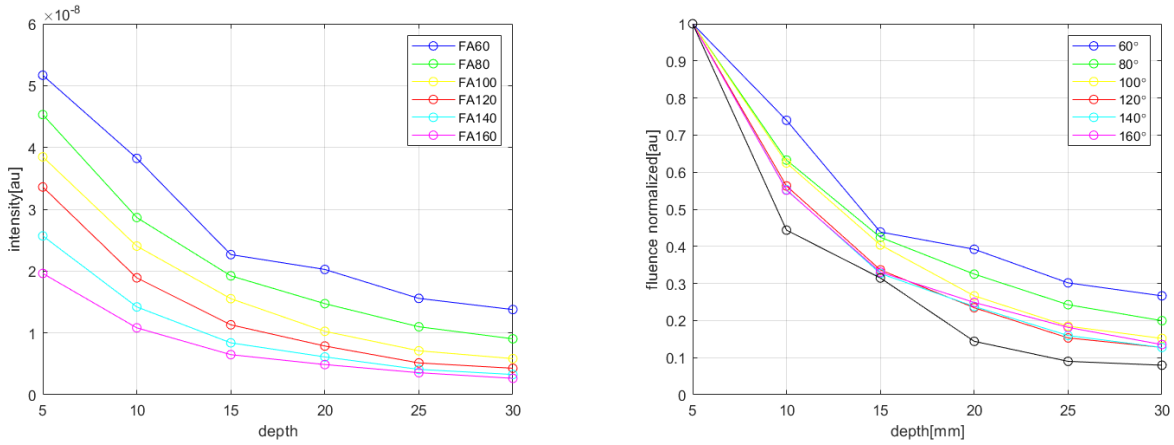

(a) *(b)*

Figure 4.4: Simulations for determining the fluence profile of a LED over depth. (a) Decay in the fluence of the PA signal over distance. (b) Normalized decay.

4.2 Results

4.2.1 Set parameters and verify the created model

In the first simulation, the change of fluence of the fluence is determined, when the LED array is moved away from the transducer, the results of this are displayed in figure 4.4. The opening angle of every single element is altered from 80 to 160 degrees with steps of 20 degrees. The results of the experiments cannot be compared directly with the results of the simulations due to a conversion factor of the conversion from light to photoacoustics signal. To be able to compare them, the results are normalized. The decay should be similar so when the starting point is set to 1, the decay of the simulation should match the experiment. In the results, it can be seen that the experimental data is the lowest line and therefore decaying faster than the simulated data. When observing the simulated fluence over depth, it can be observed that the decay of signal increases with a higher opening angle, until an opening angle of 120 degrees is obtained, when the opening angle is increased further this does not have much influence on the decay in fluence. That the change of decay is limited from 120 degrees on, indicates that the light is influenced by another factor at a higher opening angle, which can for example be by reflection. The signal obtained from the experiment has a steeper decay than is obtained during the simulations.

In the simulation where the beam profile is determined, the absorber is placed at 20 mm from the LED array and a profile is obtained. In figure 4.5a, the simulations

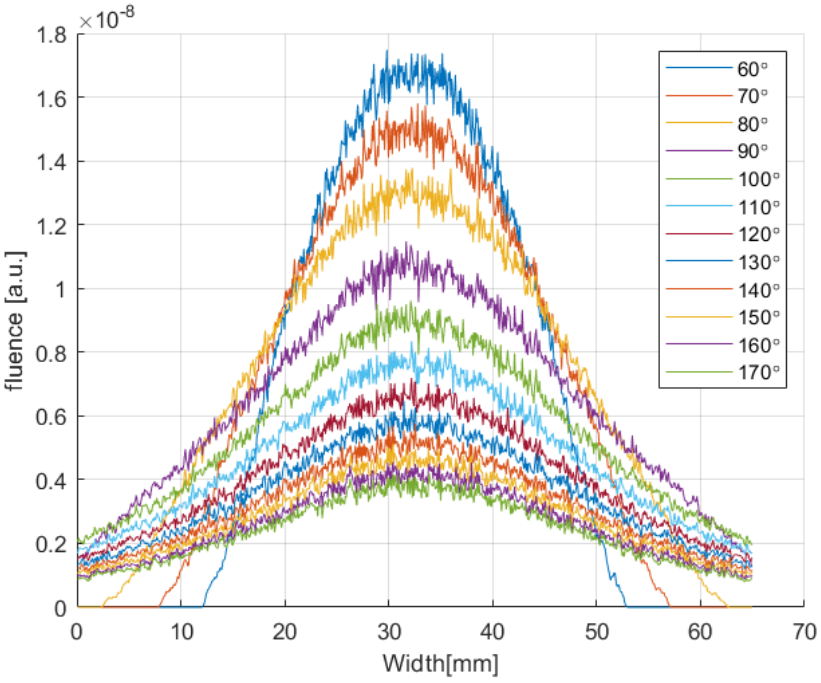

(a)

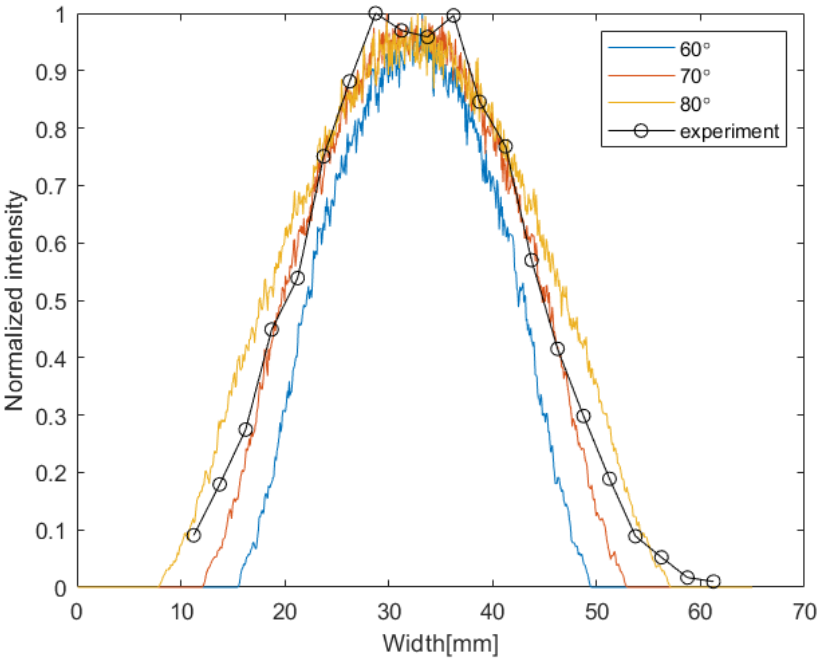

(b)

Figure 4.5: The beam profile of a LED array with an absorber placed at 20 mm from the array. (a) The profile at the absorber with different opening angles. (b) Experimental data compared with the simulations.

are shown, where the opening angle is altered from 60 to 180 degrees. The fluence over the entire absorber is obtained and used for comparison to the experimental data. The result shows that the maximum fluence decreases and the beam is wider with an increasing opening angle.

In figure 4.5b the experimental data of the beam profile is compared to the results obtained from the simulations. The values are scaled between 0 and 1 so a comparison can be done. For this comparison, only the simulated data with an opening angle of 60, 70, and 80 degrees are displayed because they come closest to the experimental data. When looking at this result, the experimental data does match best with an opening angle of 70 degrees.

Table 4.3: FWHM of the beam profile for angles from 50 to 120 degrees

Opening angle	FWHM
50°	15.3°
60°	18.9°
70°	22.1°
80°	25.8°
90°	30.0°
100°	33.5°
110°	38.2°
120°	41.4°
experiment	19.5°

For every beam profile, the results are compared, using the Full-Width Half Maximum (FWHM) as shown in table 4.3. The FWHM of the experimental data is 22.5 mm, comparing this with the simulations, an opening angle of 70 degrees will correspond with the experimental result. which was expected when looking at the results.

In the simulation where the opening angle in the air was determined by turning the LED and placing a sensor at a large distance. The LED array is turned from -120 to 120 degrees in the air. Where the beam profile over the wire is obtained for every simulation from -120 till 120 degrees with steps of 10 degrees. From every angle a profile over the absorbing line is obtained, the middle region of 8 pixels on this absorbing line is taken to determine the value of the beam profile and is used to determine the profile over the angles. This is displayed in figure 4.6. This beam profile originates from a simulation of 1 single array which is rotated. the beam profile of the simulations with a mask and an opening angle of 120 degrees are closely matching with the results obtained during the experiment. In the data of the simulation with an opening angle of 120 degrees, two drops in fluence can be

observed. These drops in fluence originate from the casing surrounding the LED elements.

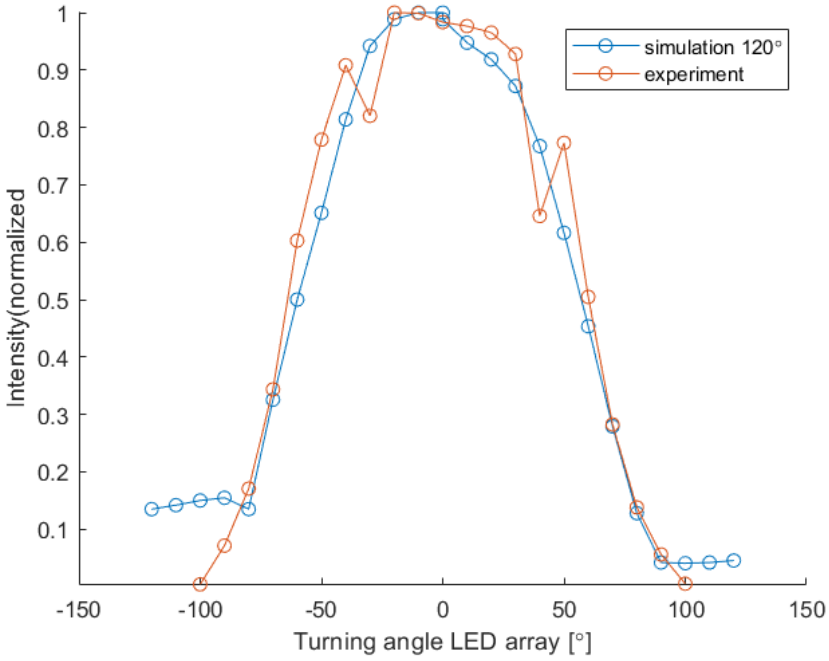

Figure 4.6: Beam profile of the LED in air during experiment and during the simulation, where the LED array is turned with respect to an absorber. An opening angle of 120 degrees per LED element is used in simulations.

Conclusion opening angle

The different simulations compared with the experimental data provide a variety of different opening angles, but the optimal opening angle needs to be determined. In the decay of fluence, a big angle comes closer to the decay in the experiment but from an angle of 120 degrees, there is almost no change any more. The simulations showing the beam profile in water an angle matches the beam profile of the experimental data best with an angle of 70 degrees. The simulation to match the opening angle of the LED elements by turning the array, an angle of 120 degrees closely resembles the experimental data.

From this, the optimal opening angle is determined. The most important value that is taken into account is the fluence profile with respect to depth, to improve the imaging depth, therefore the simulations, especially at a deeper depth are important to be accurate. The beam profile to the sides of the array is less important than the decay over depth, therefore the optimal angle determined for the simulations is an opening angle of 120 degrees.

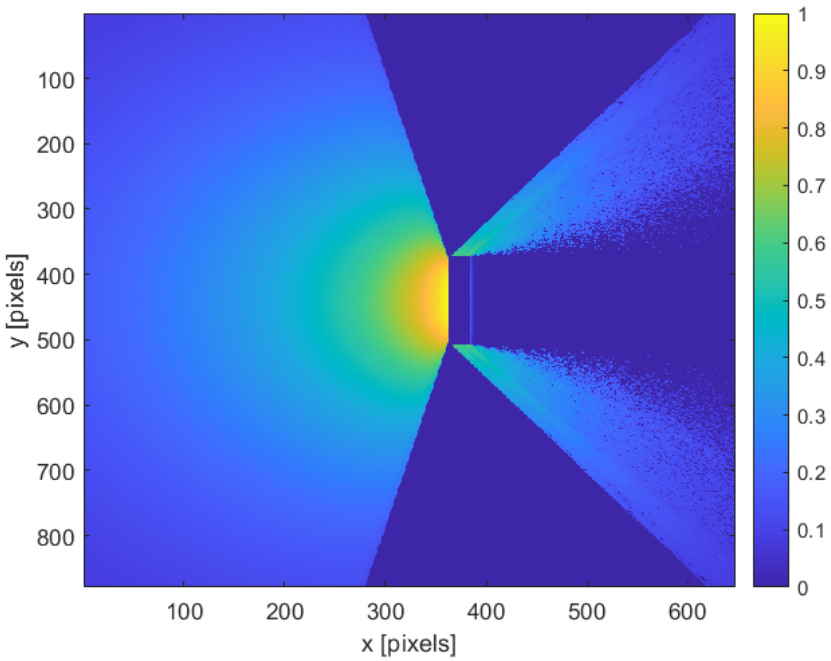

Figure 4.7: Beam profile of the LED in water with an opening angle of 120 degrees with gamma-correction of 0.1 for clear visualisation.

The beam profile of the final configuration is shown in figure 4.7, gamma correction is applied, for better visualization. The Light elements are placed inside a mask, with an absorbing mask behind the light elements, the LED array is illuminating from right to left. In this figure, it can be observed that light is reflected backward, originating from the casing, to prevent internal reflection influencing the light beam, a highly absorbing mask is placed behind the LED elements

4.2.2 Conventional PAI setup

Simulations with the 2-array setup were done for different angles to find the optimal angle of the LED arrays with respect to the transducer. The simulations are done for angles of 10 to 60 degrees. Figure 4.8 shows a fluence map obtained for a simulation of a PAI setup. This fluence map originates from the middle of the geometry, in between the two LED arrays, this plane is also the imaging plane of the ultrasound transducer in a photoacoustics setup.

In figure 4.9 the fluence profile of the simulations with the PAI set up are shown in which the angles of the LED arrays in respect to the transducer are altered from 10 to 60 degrees. The signal displayed is the signal from the middle of the imaging plane shown in figure 4.8. Figure 4.9a shows the fluence over the entire geometry,

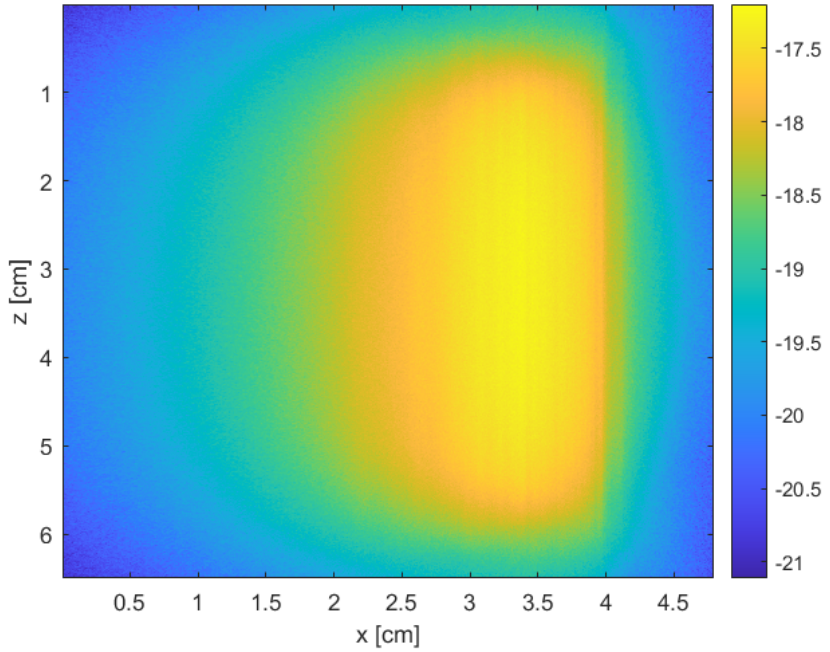

Figure 4.8: The fluence distribution of the 2 LED array set up with an angle of 60 degrees, in the imaging plane of the photoacoustics system.

where the LED arrays are placed at 1.2 cm. The profile from the transducer is shown in figure 4.9b, figure 4.9c is zoomed in at a depth of 0.8-2.6 cm. In the signal of the entire geometry, a small peak at the beginning of the signal, at 0.5 cm can be observed, this originates from reflections of the casing.

When examining the fluence, it can be seen that close to the transducer the fluence increases, with a larger angle, however looking at the fluence deeper into the medium, there is no clear distinction between the different intensities.

4.2.3 Simulate PAI system with additional LED arrays

By increasing the amount of light entering the tissue, it is estimated that the imaging depth would increase, because more light will go into the tissue, and more light will be absorbed, even at deeper depths, causing the imaging depth to increase, so two extra LED arrays are added to the simulations. In the first simulations, the LED arrays are placed parallel to the first set of LED arrays and the angle is altered to find the optimal angle.

Similar to the 2 LED array simulations, the result is shown in figure4.11, where the fluence profile is shown over the middle of the geometry, this is the middle of the plane of which the ultrasound probe forms the image. The result in figure4.11 shows that close to the LED array, the fluence is higher with a bigger angle, this

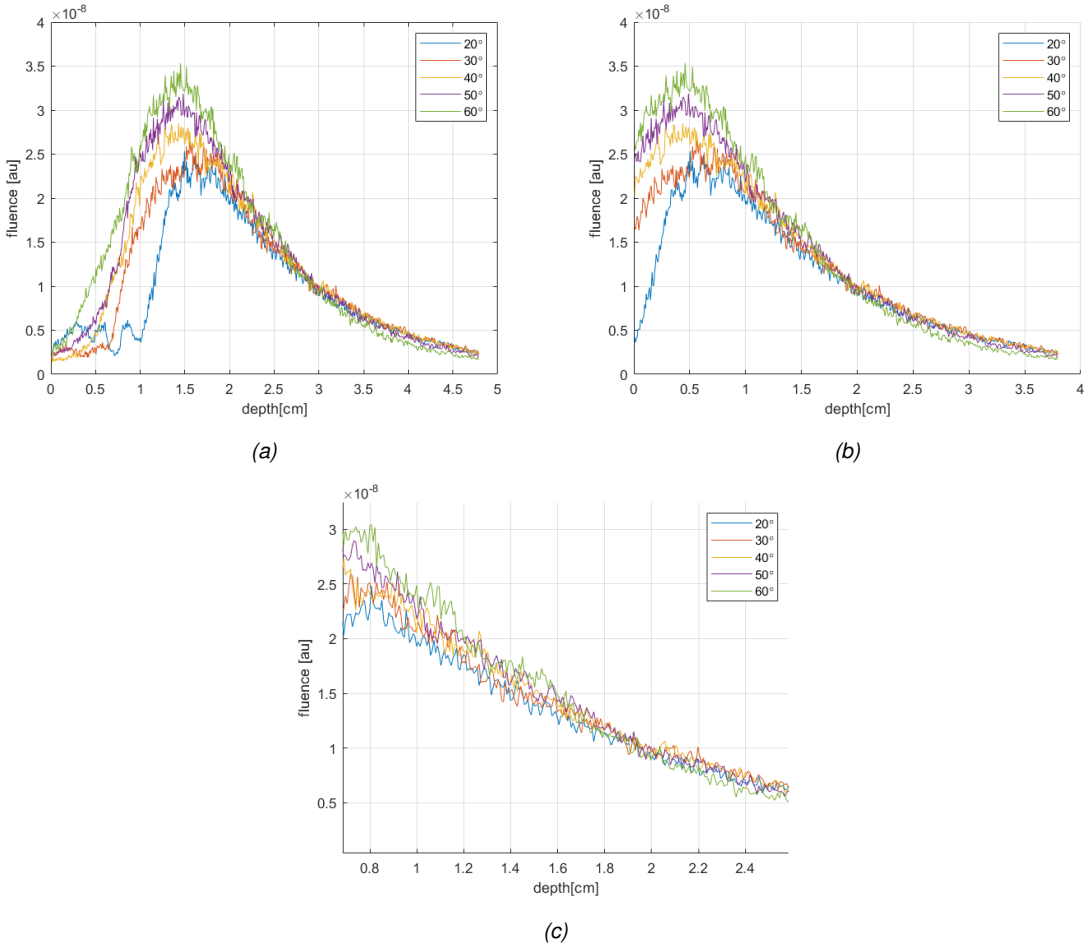

Figure 4.9: Decay in the fluence of the PAI signal over distance, (a) entire geometry, (b) fluence from the front of the transducer, (c) zoomed in to 0.7-2.5 cm.

makes sense because the LED arrays are pointed inwards, towards each other. At a greater distance, this however is not the case. At a distance it can be observed that the 10 and 90 degrees the intensities are lower at a greater distance, the geometry with an angle of 40-70 degrees has the highest fluence at a deeper depth. For this the set up of 60 degrees was determined to be the best, because signal close to the transducer is high,but at a distance from 2.5 cm from the transducer the signal remains relatively high in comparison to the other angles.

Simulations were also performed with the 4 LED arrays, where the first and the second LED array have a different angle. for example, an angle of 40 50 degrees, so the first LED has an angle of 40 degrees and the second one has an angle of 50 degrees. Results from these simulations can be observed in figure 4.12, here it can be observed that a set up with an angle of 50 degrees for LED one and 20 degrees for LED two, and the set up with an angle of 40 degrees for LED one and 50 degrees for LED two result in the highest fluence. With the 50 20 degrees set up, there is

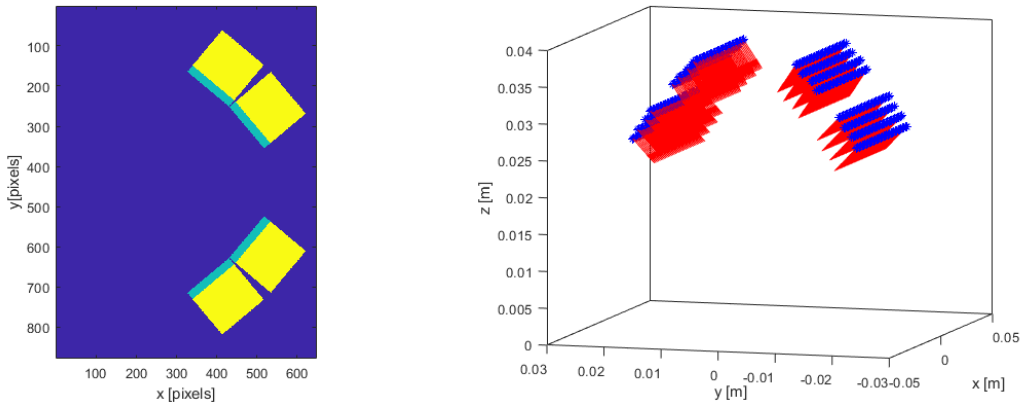

(a) *(b)*

Figure 4.10: The set up used during the simulations of the 4 LED array set up. (a)The configuration used in the two LED array set up with the different masks used, with blue: surrounding tissue, green: base mask of the LED array, yellow: absorbing mask of LED array. (b) The LED elements, which are located in the green part of the configuration in a.

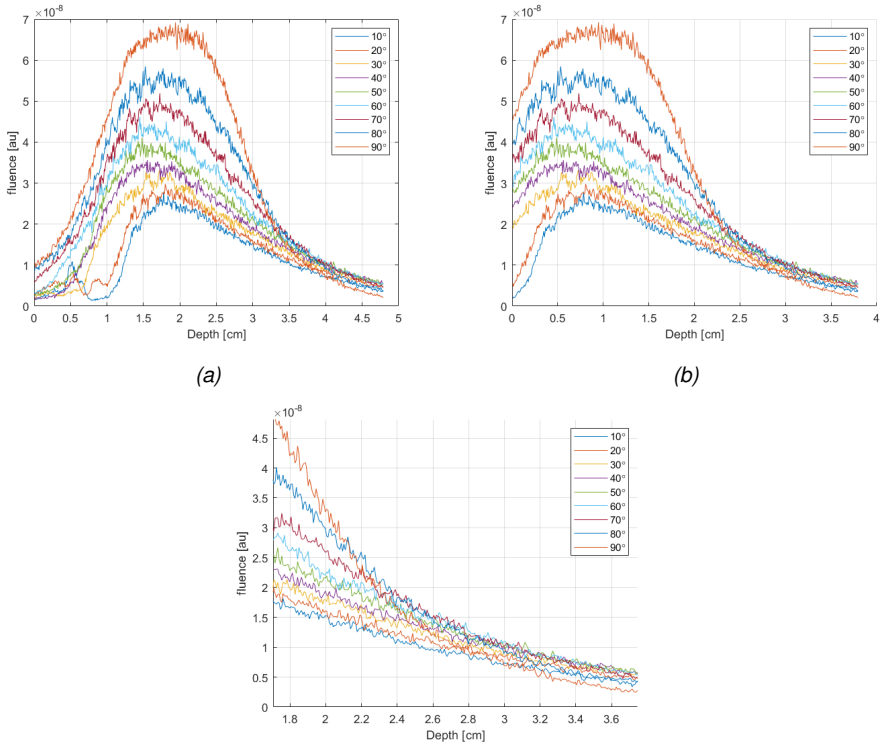

(a) *(b)*

(c)

Figure 4.11: Fluence of the simulations with 4 LED arrays at different angles, (a) fluence at the turning angles displayed over the depth of the entire geometry, (b) signal from the front of the transducer, (c)zoomed in to deeper depths.

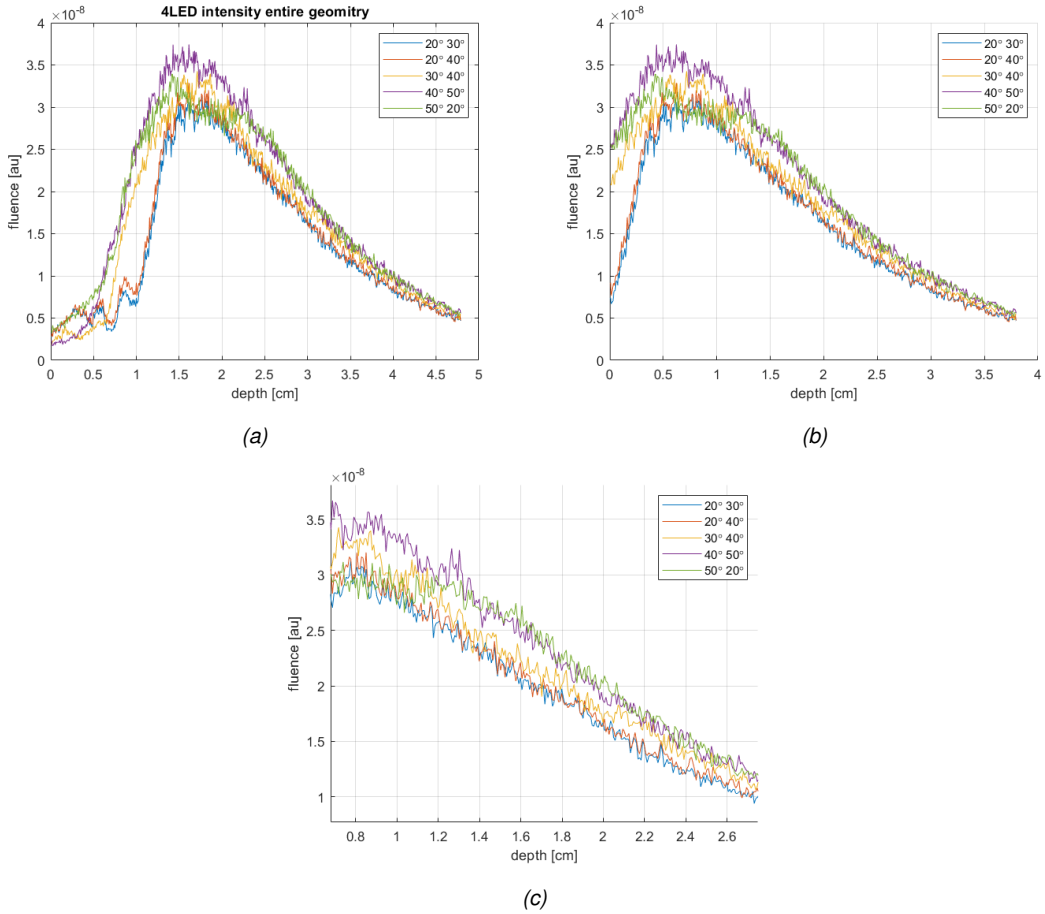

Figure 4.12: Decay in the fluence of the PAI signal over distance for simulations with 2 different angles on each side, (a) Entire depth, (b) from the front of the transducer, (c) zoomed in to deeper depths, from 0.7 till 2.7 cm.

a dip in the fluence, caused by the 20 degrees array, which is faced more forwards than inwards, therefore overall the 40 50 degree set up preforms best.

The final simulations are done of the 4 LED arrays, with two different angles, where a layer of water is placed between the transducer and the edge of the LED elements. The results of the fluence profile are shown in figure 4.13, in figure 5.9a the fluence is shown over the entire geometry, however, only from the start of the tissue signal is originating and there can be measured, from where the depth measurement starts. Therefore the results have been corrected for this in figure 5.9b.

From this it can be observed that there is no clear difference in signal over distance, only the 40 50 degrees angle set up is giving a slightly lower signal than the other measurements. Furthermore, it can be observed that there is a difference in how far the signal reaches in the different configurations. The ultrasound transducer has an imaging depth of 37.8 mm. the LED arrays are placed in front of the transducer, so with a large angle, they take up more space and by that decrease the effective imaging depth.

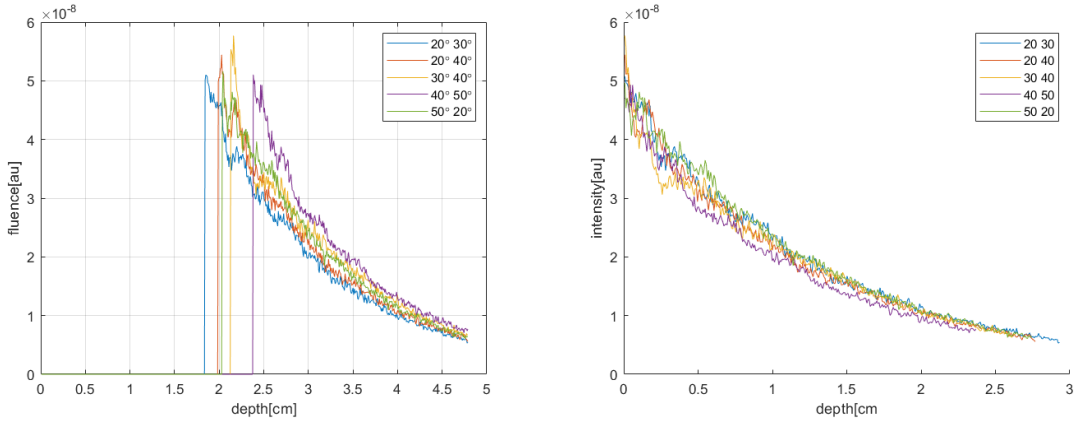

(a) *(b)*

Figure 4.13: Fluence over the simulation, with a water layer until the end of the LED arrays. (a) the entire geometry, (b) shows the fluence corrected for the start of the water layer.

4.2.4 Best configuration

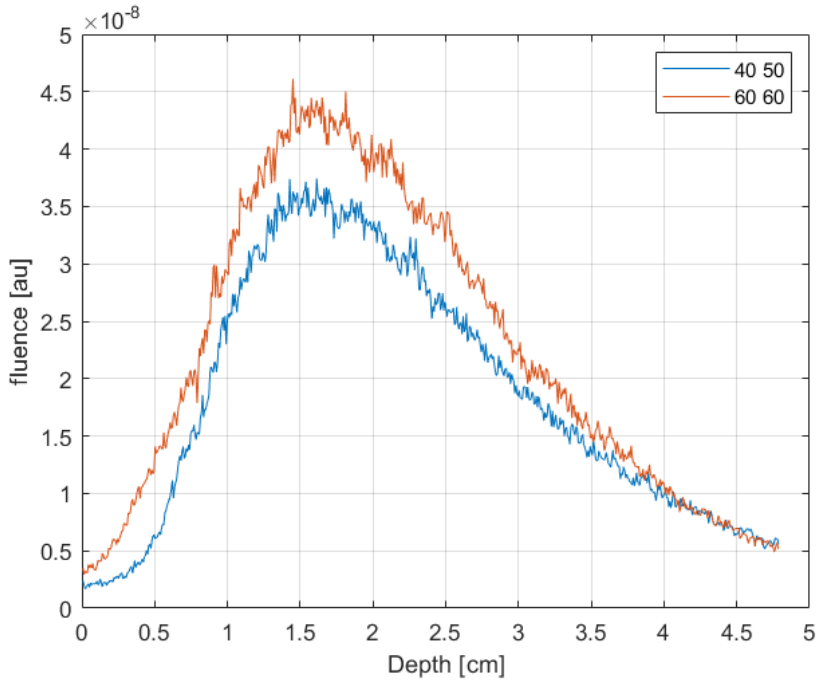

Figure 4.14: Fluence over distance of the parallel, 60 degrees set up compared to the set up with two different angles, with the used angles of 40 and 50 degrees.

From the previous comparisons, for the set up with four parallel LED arrays, the optimal angle found was 60 degrees. In the setup with two different angles for the two arrays, the best setup is the configuration where the first set of LED arrays

has an angle of 40 degrees and the second set of LED arrays has an angle of 50 degrees. To find which setup would result in a better imaging depth, the fluence over the middle of the imaging plane is compared. The results are shown in figure 4.14. Comparing the results, it can be observed that the parallel setup has a higher fluence than the set up with different angles, until at a deeper depth of 4 cm, the fluence of both configurations is similar. Therefore the parallel configuration with 60 degrees is optimal.

4.3 Conclusion

With the simulations done in this chapter, a model is created of the photoacoustics setup. The opening angle of the LED elements in the LED array is determined to be optimal at 120 degrees. This is used in the setup where two and four LED arrays are used. The optimal angle for the 2, 4, and 4 with different angle LED array set up are examined. The optimal angle for the 2 LED array set up could not be determined. The optimal angle for the 4 LED array set up was found to be 60 degrees. For the four LED arrays set up with different angles, the best angles found was 40 50 degrees. Comparing the best results, the optimal setup to be found was the set up with parallel angles with an angle of 60 degrees. These results need to be verified during experiments, which is done in the following chapter.

Chapter 5

Experimental validation of the simulations

In chapter 4 the optimal configuration for enhancement of the imaging depth in a photoacoustics system was investigated by doing simulations. In this chapter, experiments are executed using a developed probe holder, to validate the results from the simulations.

This work was done in collaboration with bachelor student Elise Schilt.

5.1 Method

5.1.1 Experimental setup

In this chapter, experiments are done to validate the simulations executed in chapter 4. For the experiments, a setup, shown in figure 5.1, was created where LED arrays can be placed next to the transducer, AcousticX (Cyberdyne Inc., Tsukuba, Japan), and the angle and location of the LED arrays can be altered. In this holder, the number of LED arrays can be changed, in this work altering from one LED array on each side of the transducer to two LED arrays on each side. The drawings and SolidWorks design of the probe is added in Appendix B.

The location and the angle of the LED arrays can be altered to position them in a preferred location. When experiments with the setup are performed, the chosen amount of LED arrays are placed in the holder. The LED arrays are placed at the preferred angle and located so that the edge of the array touches the ultrasound transducer, or the LED array placed next to this.

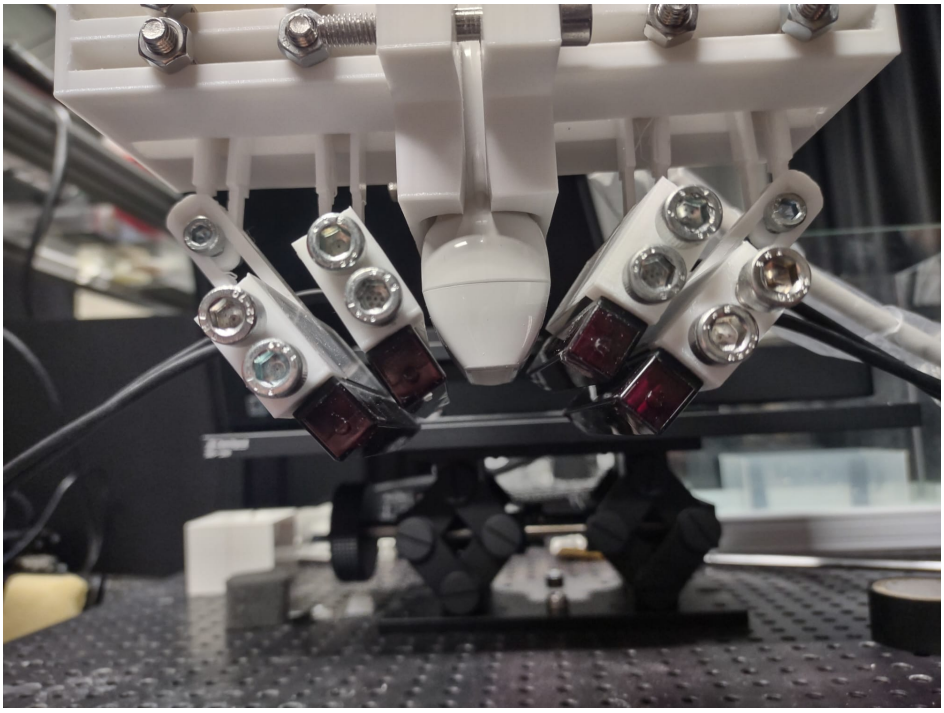

Figure 5.1: The set up with the developed LED array holder, attached the the ultrasound transducer.

5.1.2 Experiments in tissue-mimicking phantom

Figure 5.2: Phantom with the 8 absorbers placed the container, located 10 mm apart laterally and 5 mm apart axially.

To investigate the imaging depth and signal-to-noise ratio for validating the results of the simulations, multiple surgical threads are used as absorbing targets, similar to the surgical thread used in the 1 LED array experiment (vetsuture, black nylon, USP 4/0 metric 1.5). The threads are placed in a transparent plastic container (Raaco). Holes are drilled and the thread is placed in the desired positions, 10 mm

apart laterally and 5 mm apart axially. A total of 8 threads are placed, so the lowest thread is placed 35 mm below the first thread. The phantom is shown in figure 5.2

For the experiments, a tank in is filled with a medium mimicking tissue, described in appendix C, with absorbing and scattering coefficients:
absorption coefficient: $\mu_a = 0.033mm^{-1}$
reduced scattering coefficient: $\mu_s' = 6.67cm^{-1}$

The setup is prepared, with previously determined angles and alignment, above the phantom material. When the LED arrays are aligned correctly, the setup is lowered into the phantom material, above the phantom with the absorbing surgical treads. With the set up with 2 LED arrays, the transducer is placed 8-9 mm from the first wire, with the set up with the four LED arrays, this was 19-20 mm. The setup was aligned with the container for each measurement, to keep the orientation constant between the measurements.

5.1.3 Ex vivo imaging experiment

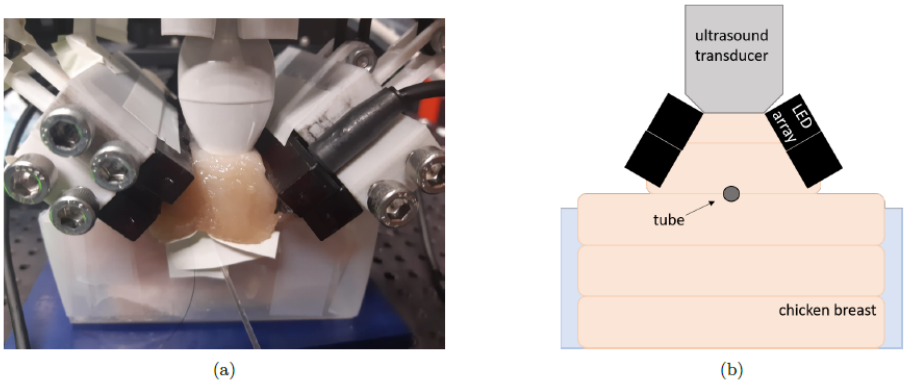

Figure 5.3: Setup used for the chicken experiment, where a tube filled with Indian ink is placed in between slabs of chicken tissue to mimic a blood vessel.

With the configurations that are found to be optimal, an experiment with tissue will be performed. For this experiment, chicken tissue is used. The chicken tissue is sliced in slabs of 5-10 mm thickness. Chicken tissue is placed in a plastic container with a minimum of 20 mm of chicken tissue placed in the container. Above this layer, a tube with 1 mm diameter is placed which is filled with a solution of Indian ink with milliQ water, with an absorption coefficient of 1.0 mm^{-1}. Over the tube, layers

of chicken breast tissue are placed, to place the tube at the preferred depth. In between each layer and in between the chicken tissue and the transducer ultrasound gel (SONOGEL, Germany) is used. The setup is shown in figure 5.3.

During the experiment, three measurements at different depths were performed. Between every measurement, a layer of chicken tissue was added to increase the distance between the transducer and the tube with the absorbing medium. This is done for the optimal configurations found earlier.

5.2 Results

5.2.1 Tissue mimicking phantom with 2 LED array setup

In the experiments, with two LED arrays, one on each side of the transducer, the angles used during the simulations were tested using angles from 0 to 60 degrees in the measurements in the phantom solution. The log plots of the reconstructed photoacoustic images are shown in figure 5.4. The absorbing thread is visible in these log plots. It can be clearly seen that there is a difference in the number of visible threads, between the different angles. Most noise can be observed at the 10 degrees angle. There is also a reflection artifact visible underneath the thread. The PA signal intensity of each thread is measured for each angle, and plotted over depth, as shown in figure 5.5a. The CNR is calculated and plotted over distance in figure 5.5b.

The 50 degrees setup results in the highest signal intensity, but a setup with a 60-degree angle shows a better signal intensity at larger depths. In the log plot of the reconstructed image in figure 5.4e, 3 threads are clearly visible. The best depth of 24 mm is obtained when using a 60° angle. The CNR is the best for 50° angle up to 18 mm of depth. At lower depths, the CNR of the 60° angle is slightly higher for a depth of 1 mm, after this both CNRs decay almost parallel to each other.

5.2.2 Tissue mimicking phantom with 4 LED array setup

After the experiments with two LED arrays, one on each side of the transducer, two more LED arrays are added, so that there are two LED arrays on both sides of the transducer. During the experiments, 6 different angles were used for the LED arrays, from 0 to 60 degrees with steps of 10 degrees with a parallel setup.

The set-up was the same as in the 2 LED arrays experiments, except that because of the design of the adjustable holder, the set-up was positioned so that the first thread was 19-20 mm from the surface of the transducer. The distance was kept constant over the measurements so that comparison was possible. An angle of 60

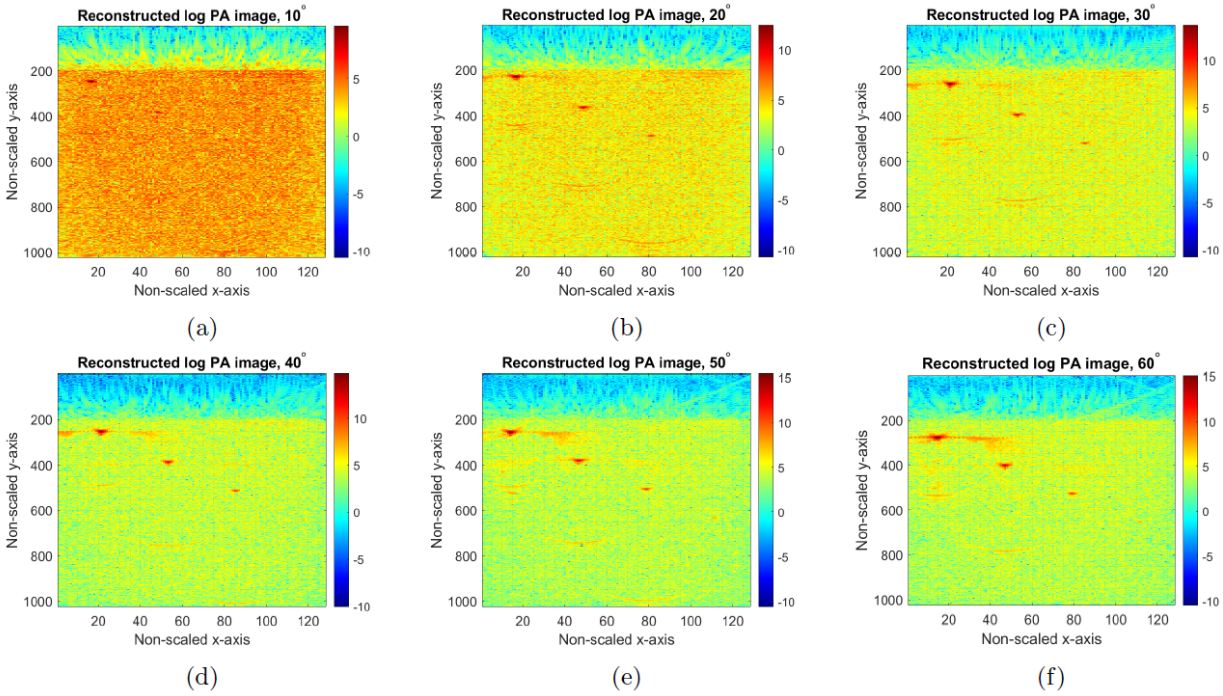

Figure 5.4: Log plots of the images obtained during the experiments with two LED arrays in the probe holder for different angles.

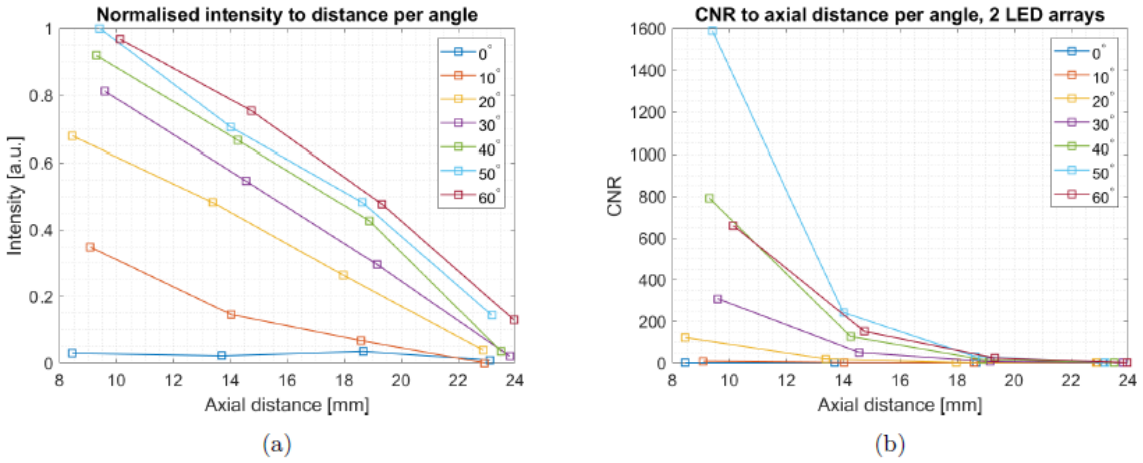

Figure 5.5: The results of the experiment with the two LED arrays in the probe with: (a) The signal intensity of the absorbers at varous depth, (b) the CNR of the signal.

degrees has the highest signal intensity over a distance up to approximately 29 mm. The last thread at a depth of 32-33 mm 50 degrees has the highest signal intensity. Looking at the CNR, the 60-degree setup shows a better result over the complete distance. The other angles show a low signal intensity at a great depth.

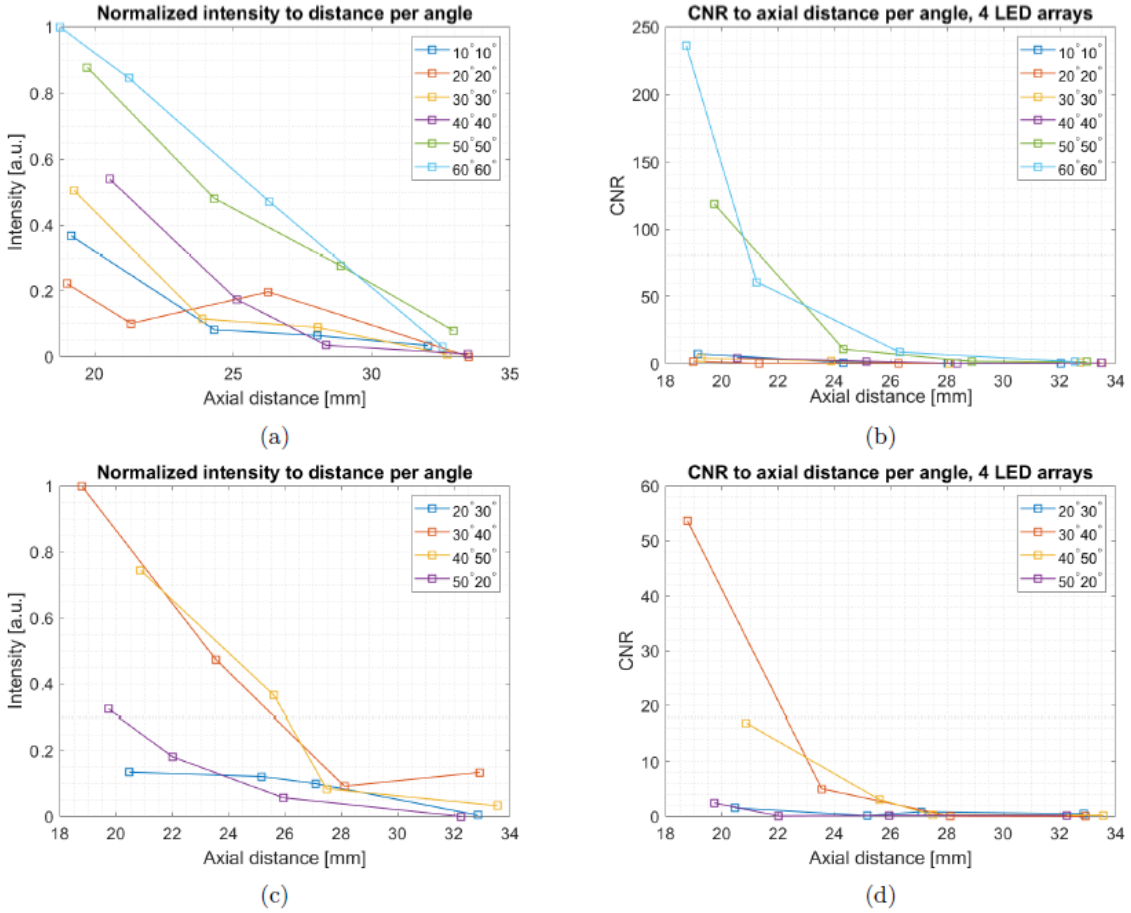

Figure 5.6: The results of the experiment with four LED arrays in the probe with: (a)The signal intensity of the absorbers at various depth for the set ups with parallel angles, (c)and different angles. (b)The CNR of the signal (d)for parallel angles and different angles.

Afterward, measurements were executed where the angle with respect to the transducer of the first array is different than the angle of the second array. For these four combinations were tested, namely: 20° 30°, 30° 40°, 40° 50°, and 50° 20°, where the first angle is the angle of the first LED array with respect to the transducer, and the second angle is the angle of the second LED array with respect to the transducer. In a lowered position, 20° 40° was measured.

Figure 5.6 shows the results of the experiments with the set up with 2 different angles. Here can be observed that the 30° 40° and 40° 50° set up have the highest signal intensity at the start, but at the third thread is close to the other configurations. The set up with 30° 40° angles showed the highest signal intensity at the deepest depth. The intensities at the last thread at a depth of approximately 33 mm increase slightly in comparison with the third thread at a depth of 28mm.

The experiments with the 2 LED array set up and with the 4 LED array set up

with parallel and nonparallel angles are compared to determine the best set up. The best 7 results, based on signal intensity over the depth are shown in figure 5.7. A threshold is set to the signal intensity where the thread is visible by the observer. In this way, a threshold of 14 % of the maximum signal intensity is chosen.

Figure 5.7b is zoomed in to the biggest depth. These figures show that the 4 LED arrays set up delivers more light to a deeper depth in comparison to the 2 LED array set up. It can also be observed that in the 4 LED arrays system the parallel angle set up results in a greater imaging depth.

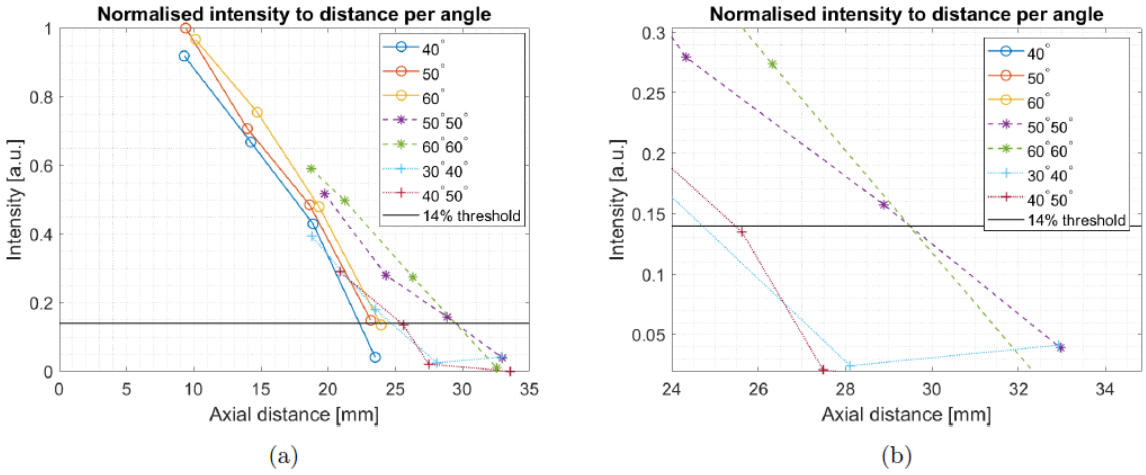

Figure 5.7: The three best angles of the 2 LED arrays system and the four best angles of the 4 LED arrays system plotted against axial distance in a). The black line is the threshold under which threads were not visible in the log plotted reconstructed photoacoustics image. In b), it is zoomed in on the highest axial distance between approximately 24 and 30 mm of depth.

It can be hardly distinguished whether 50°50° is better or worse than 60°60°, so the CNRs should also be taken into account. At the highest axial depth, in figure5.7 approximately 29 mm, the CNR of the 50°50° angle is 1.5, while at 60°60° the CNR is 5.5. Therefore, it can be concluded that 60°60° is the optimal illumination angle in the current set-up, reaching 29 mm of depth.

5.2.3 Ex vivo imaging experiment

In this experiment, two setups are investigated. The first set of angles is the parallel set up with an angle of 60 degrees, equal for all 4 LED arrays. The second set up with the two LED arrays with an angle of 60 degrees. These angles are chosen because they showed the best imaging depth.

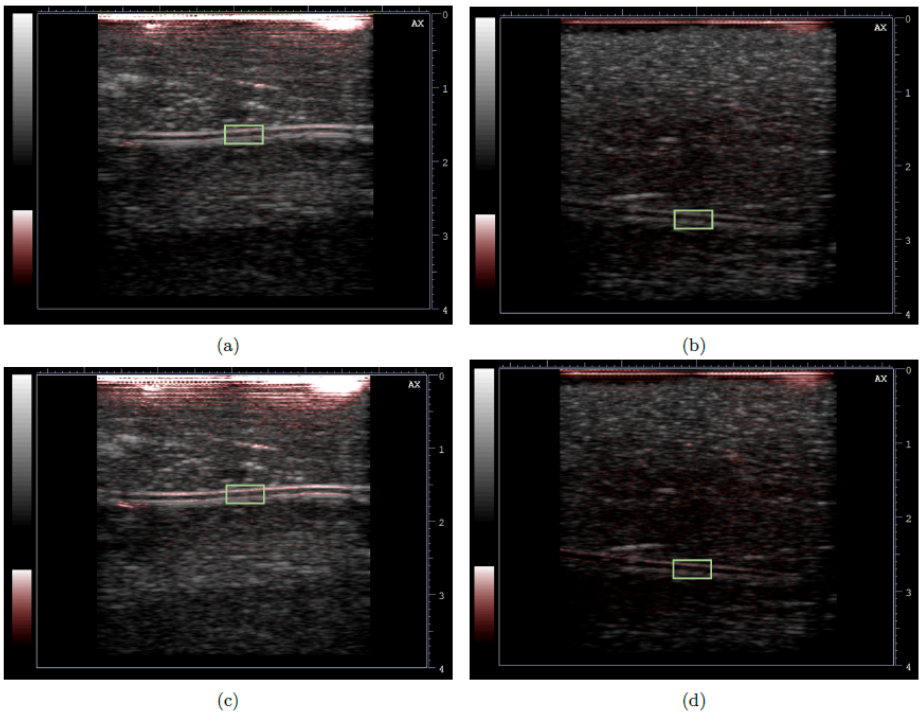

Figure 5.8: PAI images of the tube in chicken breast tissue. The green square marks the region of interest.

Figure 5.8 shows the reconstructed images of the tube in the chicken tissue. The area in the green square in each image is used to determine the signal intensity of the tube. These values are displayed in figure 5.9

Comparing the 2 LED array set up to the 4 arrays set up as done in figure 5.9 shows that the signal intensity of the 4 LED array set up is higher. At a depth of approximately 27 mm, the intensities are closer to each other. The decay of CNR looks similar in shape to the signal intensity of the two LED arrays.

5.3 Conclusion

In this chapter, experiments are done to validate the simulations. During the experiments, the optimal setup is investigated for a 2 LED array set up, a 4 LED array set up with parallel angles, and a 4 array set up with different angles. For the 2 LED array set up the optimal angle that was found is an angle of 60 degrees, in the set up with 4 LED arrays the optimal angle was also 60 degrees, and in the set up with different angles, the optimal configuration had angles of 30 degrees for the first set of LED arrays and 40 degrees for the second set of LED arrays. Comparing the optimal setups with the parallel and different angles, the parallel setup has proven to be better. In chicken tissue experiments were with the 2 LED arrays setup and with

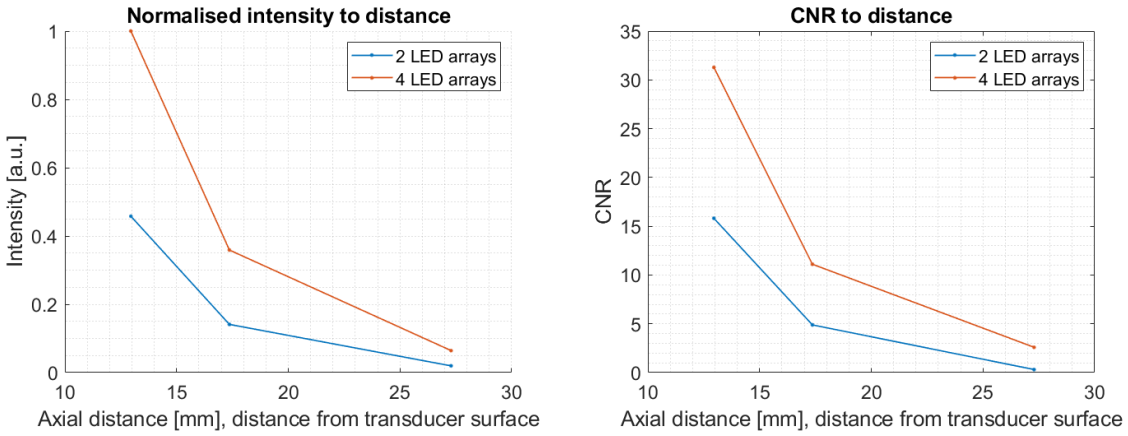

(a) *(b)*

Figure 5.9: The signal in the tube, obtained from the chicken breast experiments for the two set ups, one with two LED arrays used, the second with four LED arrays used in the set up (a) signal intensity plot (b) CNR of the results

the 4 LED arrays setup with parallel angles. The best results were obtained with the 4 LED arrays setup. This corresponds with the results in the simulations of the previous chapter

Chapter 6

Investigating a new configuration

In this chapter, a new configuration for enhancing the light delivery at a deeper depth and with that improving the imaging depth is investigated using Monte Carlo simulations. The optimal configuration found in chapter 4 is compared with the results in this chapter to find the best configuration.

6.1 Method

In this chapter, the simulations are used to investigate the optimal setup for a better light delivery at a deeper depth. The results in the previous chapters show that increasing the amount of LED arrays increases the imaging depth. Therefore, the question is raised: how does the amount of LED elements influence the light fluence in a tissue, and what is the best shape of the LED arrays for a better imaging depth?

Improving the imaging depth using simulations, the setup is not limited to using existing LED arrays as used in the previous chapters. A custom LED array can be created and in the future be manufactured. In this chapter, the best configuration is investigated outside the limitations of using an existing array.

6.1.1 Number of LED rows

To examine how the amount of LED rows influences the light delivery, simulations are done whith the setup created, where the number of rows is altered. The configuration is similar to the configuration in previous chapters, with 2 LED arrays, one on each side of the transducer at an angle, but the number of rows in the simulations is increased from 2 to 10, adding 2 rows at every simulation. This was examined with an angle of 60 degrees with respect to the transducer, which is the best angle found in the previous chapters. The optical properties used are the same as described in table 4.2. The medium in which the probe is simulated has the optical properties of tissue.

6.1.2 Curved LED array

Another configuration that is possible is a configuration where the LED arrays have a curvature. A curved array could potentially create a focus of light inside the medium, which can be used to focus deeper in the tissue. A curved array, shown in figure 6.1 was created using the same rows of LED elements as found before. To investigate the best configuration of a curved array, a single curved array is created, so the best angle can be found for creating a focus deep in the tissue.

These tests are also executed by placing a layer of water between the LED arrays and the tissue. The array should image a human body, which can be a (semi)flat surface. The configuration can cause the transducer to not be able to touch the tissue, therefore a coupling medium should be used in this case. The influence of the curvature on the light distribution in the tissue will be investigated.

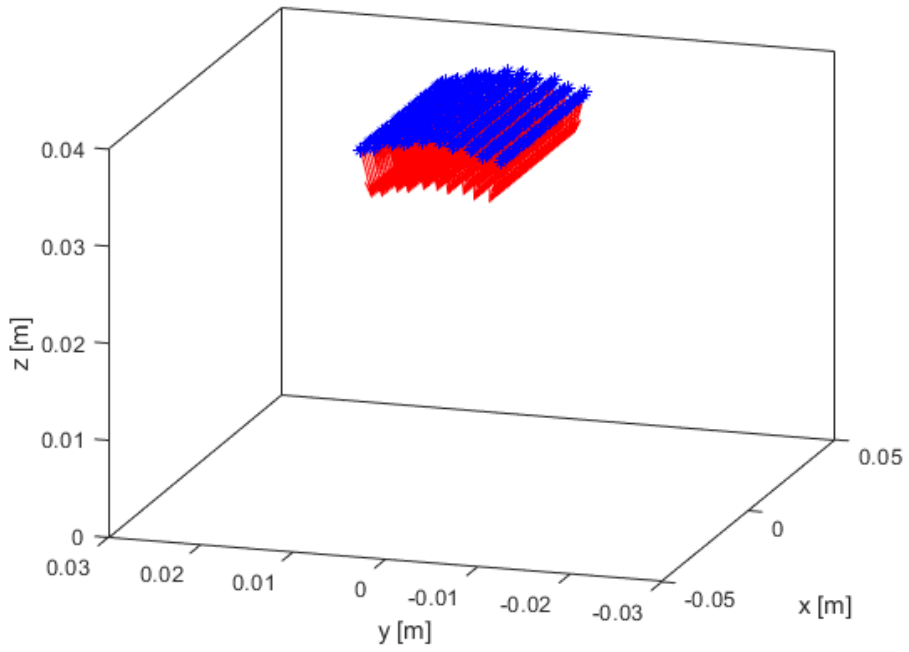

Figure 6.1: Location of LED elements of the curved array, with a curvature of 6 degrees between each row of LED elements.

6.2 Two curved arrays

When the optimal curvature is found, a setup was created using the curved LED array as found to be optimal in the previous experiments. The LED arrays are placed 14 mm apart, like before, as if the US transducer would be in between the LED arrays. The angle of the LED array with respect to the transducer changed, this angle

is defined as the angle between the transducer and the first row of LED elements. The angle was increased from 0-80 degrees with steps of 10 degrees. The position of the LED elements rows can be seen in the figure 6.2. The distance between the LED elements is 14 mm the same in all simulations. With this setup, the angle is varied to obtain the optimal configuration for good light deposition at a deeper depth and with that a deeper imaging depth.

When the best configuration is obtained for the curved array, the curved array will be compared with the set up with parallel angles to obtain the best configuration.

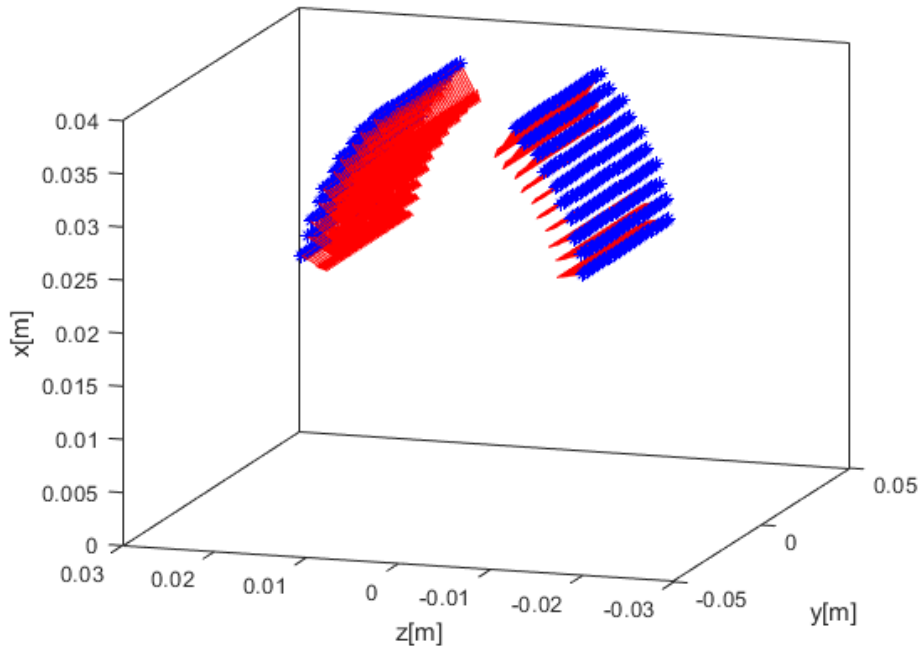

Figure 6.2: Two curved arrays with a space of 14 mm in between so an ultrasound transducer can be placed there. The curvature of the arrays is a 4-degree difference between every row of LED elements and a starting angle between the first array and the transducer of 40 degrees.

6.3 Results

6.3.1 Big array

Simulations are done where an angle of 60 degrees is used, and the number of LED rows is increased. From the results in figure 6.3 it can be observed that the fluence increases with increasing the number of LED rows. This can also be expected because, with LED rows, more energy is generated by the LEDs resulting in higher

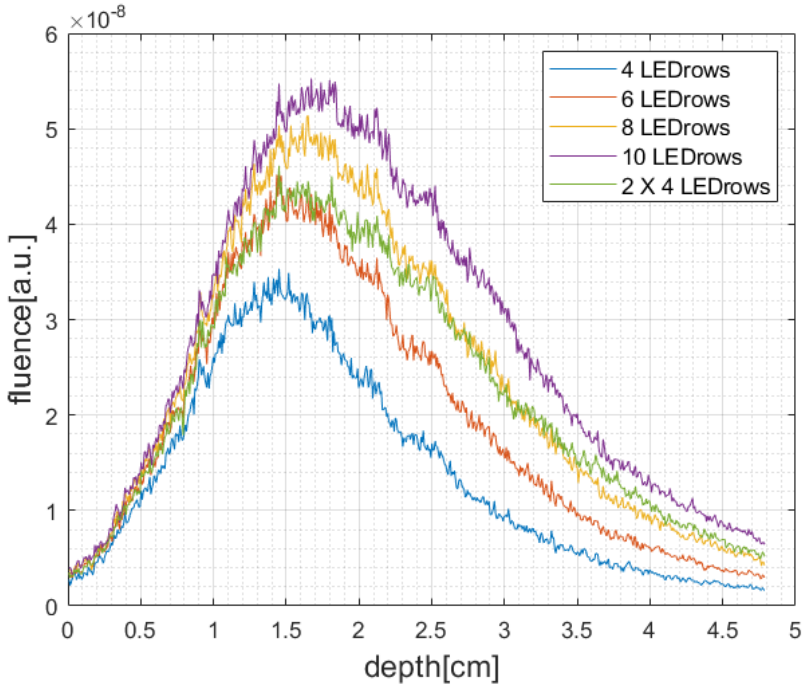

Figure 6.3: Fluence profile for arrays increasing in size, by increasing the number of rows used in an array.

fluence. However, it must be considered that with increasing the number of rows, also the size of the LED arrays increase. This can be a limiting factor because the tissue which is measured might not fit in between the LED arrays, causing a big gap between the transducer and the tissue, hindering the imaging depth.

Figure 6.4 shows how much the fluence of the setups differs from the fluence of the setup with 4 rows of LED elements, which is used as the standard. The set up with 6 LED rows increases to a factor of 1.7, the 8 LED row set up to 2.5, the 10 LED row set up to 3.8 with respect to the 4 LED row set up. Therefore in these simulations, the 10 LED row set up was determined to be the best, and not more than 10 rows were tested due to the increasing size of a LED array.

6.3.2 Curved array

A configuration that is possible is a configuration where the LED arrays have a curvature. To investigate the best configuration a single curved array is created. This was done with a mask as before. However, when looking at the results in figure 6.5, it is not as would be expected. The decay of fluence at every curvature angle of the array is the same, while you would expect to see some influence of the curve in the fluence profile. When looking into the simulations better, it can be observed that

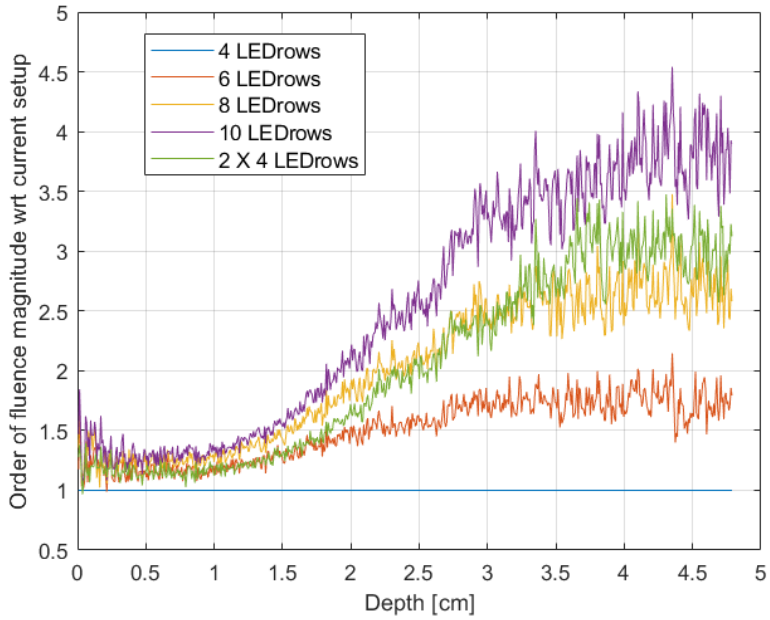

Figure 6.4: Order of fluence magnitude from amount of LED rows with respect to the 4LED row set up.

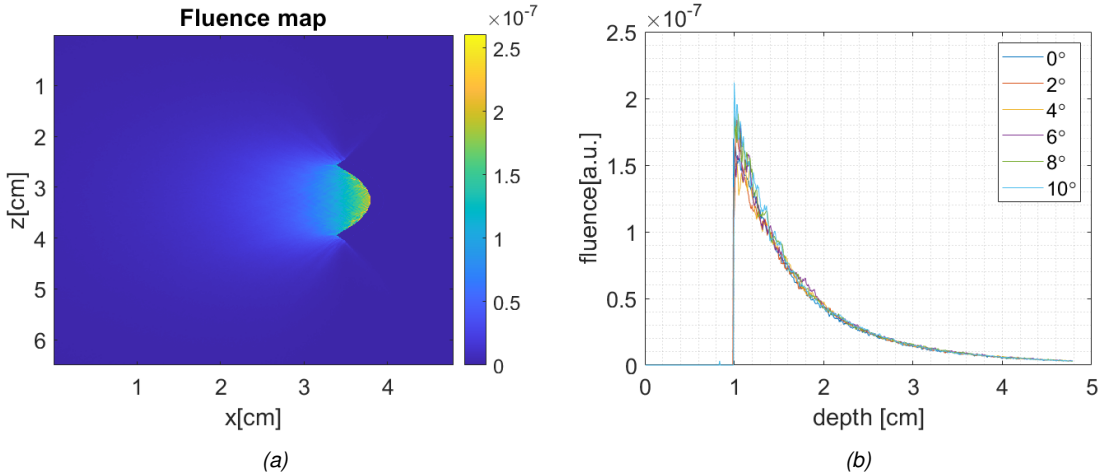

Figure 6.5: (a) The fluence map of a curved array of 6 degrees, with a mask, resulting in reflections in the curved array. (b) Fluence signal over the middle of the imaging plane for altering curvatures.

there is some error occurring originating from the mask. Therefore, it is chosen to do these simulations without a mask.

When looking at the simulations without a mask in figure 6.6a, there is a difference in the fluence profile over the middle of the configuration. Close to the light elements, there is a peak observed, which decays rapidly, indicating a focus of light. However, at a greater depth, not much difference can be observed. In figure 6.6b it

can be observed that there is a signal behind the LED arrays, which are placed at approximately 0.9 cm. This signal occurs because no mask is used anymore and the LED elements are surrounded by tissue-mimicking properties, causing light to scatter to the back of the LED array.

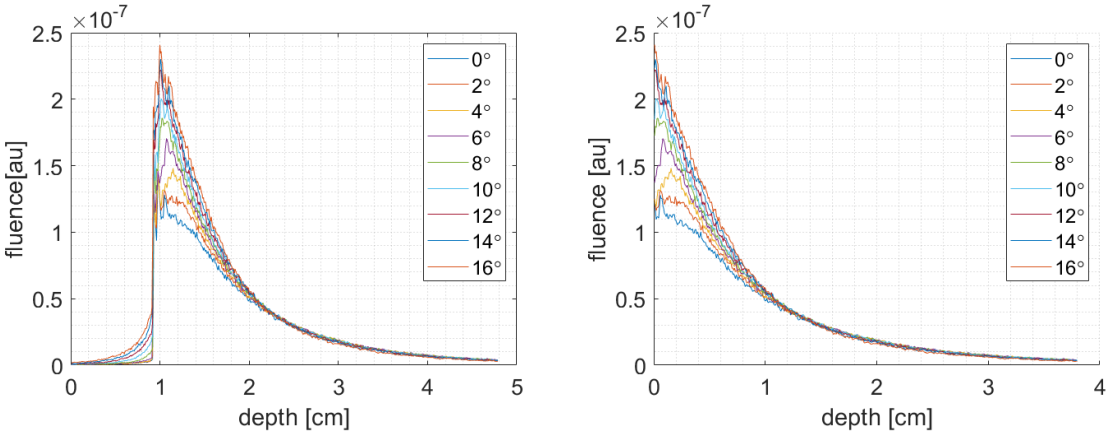

Figure 6.6: The fluence profile of the curved LED array placed without a mask, with altering curvature angles. (a) Fluence profile of the entire geometry. (b) The fluence profile, corrected for location of the curved LED array.

When investigating the influence of the curvature on the fluence distribution, it can be observed that a curved array causes a peak in the fluence distribution close to the ultrasound transducer, placed at 0 in figure 6.6b. It can be observed that around 3 mm away from the transducer a peak in the graphs of the fluence distribution, so a focus is formed. From these graphs, it can be observed that the focus from the configuration with a curvature of 4 degrees between each row of LED elements is furthest away from the transducer, at 2 mm from the transducer. From 1 cm in the tissue, there is no difference between the fluence of all the configurations.

In figure 6.7, a layer of water is added to the simulations, so the LED elements are surrounded by water and the light enters a tissue-mimicking layer below the water. The first figure shows the fluence plot of curvature with a difference between the LED rows of 0 to 12 degrees with steps of 2 degrees. From figure 6.7a, it can be observed that the signal starts later with a changing angle because the water layer starts at the end of the LED array. In figure 6.7b a correction for the water layer has been used, at 0 the tissue layer starts. Here can be observed that the lowest curvature angle causes the highest fluence in the tissue, decreasing with increasing the curvature. Furthermore, it has to be marked that with an increasing curvature, a bigger layer of the imaging plane is not used, causing the useful imaging plane to be decreased with a bigger curvature.

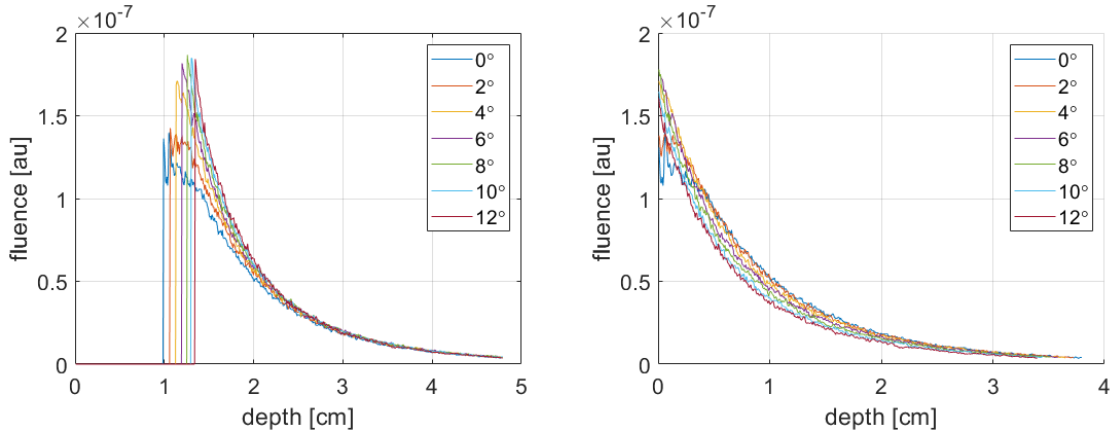

Figure 6.7: The fluence profile of the curved LED array placed in a waterlayer. (a) Fluence profile of the entire geometry. (b) The fluence profile, corrected for the layer of water, where 0 is the start of the tissue layer.

Two curved arrays

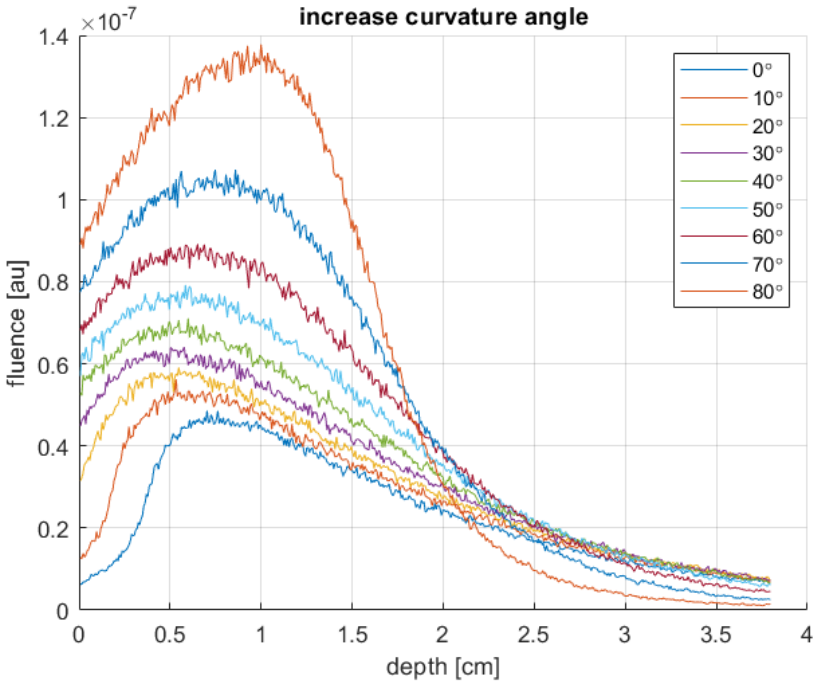

Figure 6.8: Fluence over distance, with an array with a curvature of 4 degrees, increasing the angle of the first element with respect to the transducers.

After simulations with 1 LED array, one LED array is divided into a 2 LED array setup. In this setup, the best curvature of the two arrays with respect to the transducer is investigated. The fluence profile is shown in figure 6.8, where it can be observed clearly that a bigger angle gives a higher fluence at the start, however at a

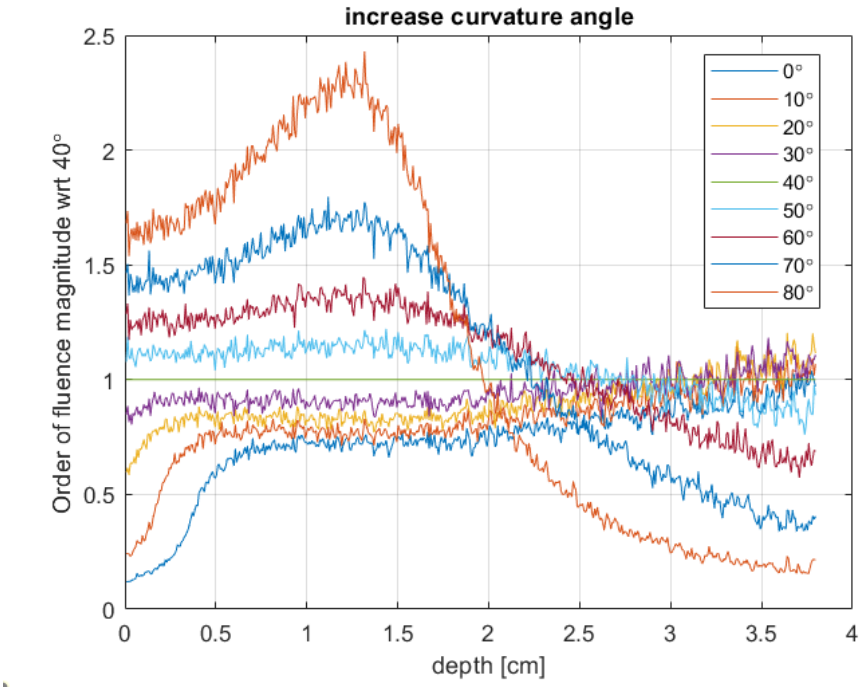

Figure 6.9: Order of fluence magnitude from the array with a curvature of 4 degrees, increasing the angle of the first element with respect to the transducer, with respect to the curved array with an angle of 40 degrees.

depth of 2 cm this changes. When looking deeper into the imaging plane, it can be observed that an angle of 20-50 degrees gives the best results with the highest fluence. For better comparison, the relation between the different setups is examined in figure 6.9 with respect to the 40 degrees setup. In this figure, it can be observed that the 80-50 degree setup has a higher fluence at the start, but deeper in the tissue, the fluence is lower than the 40 degrees set up, at 1. The angles from 0-30 start with a lower fluence than the 40 degrees set up, and at a deeper depth there is no significant difference, therefore the 40 degrees set up is determined to be optimal.

In figure 6.10, the beam profile of the set up with an angle of 40 degrees, perpendicular to the imaging plane of the transducer is shown, 5 mm further from the transducer for every figure. The ideal would be that as much light as possible would stay in the imaging plane (in the middle of the curve). close to the transducer peaks are clearly visible, originating from the LED elements, which are further away deeper in the tissue, resulting in a smooth fluence curve.

6.3.3 Optimal configuration

Figure 6.11 shows the results of the two optimal configurations found in this chapter: The curved array and a parallel array at an angle of 60 degrees. Both configurations

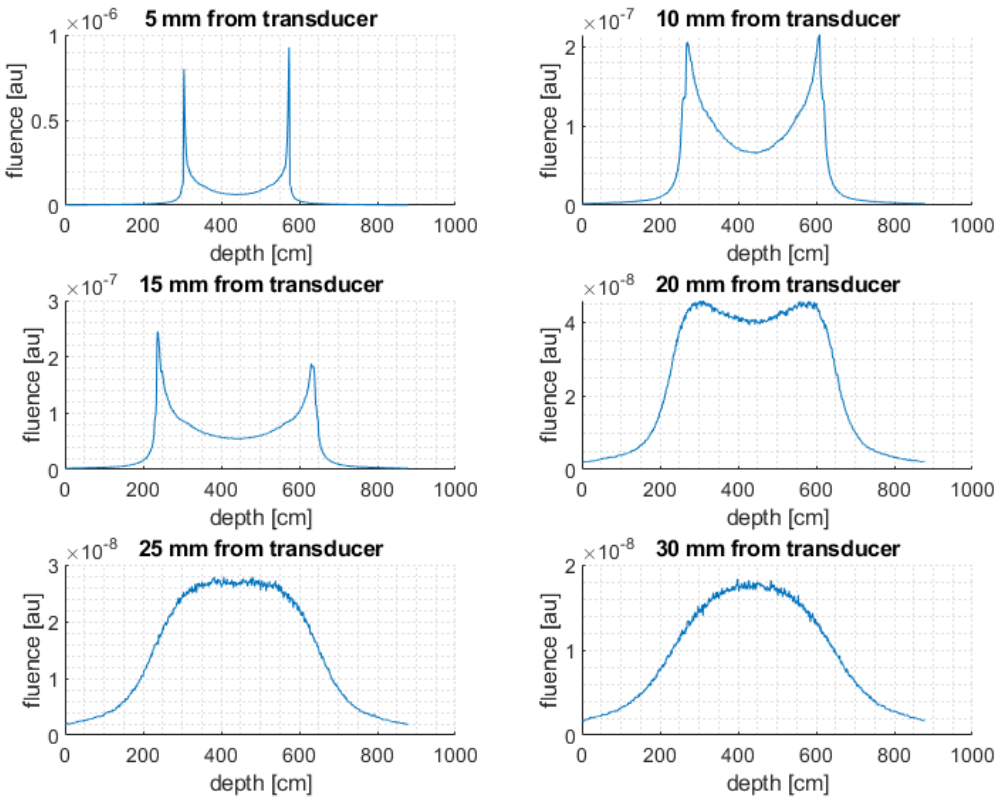

Figure 6.10: Fluence profile perpendicular to the imaging plane, at depths from 5 to 30 mm from the transducer of the 40 degree curved setup.

contain the same amount of LED elements in the same amount of rows, but with another configuration. Figure 6.11 shows that the set up with the straight configuration obtained a higher fluence over the entire depth after the transducer, which is placed at 12mm from the base.

6.4 Conclusion

In this chapter, a new configuration for enhancing the light delivery at a deeper depth and with that improving the imaging depth is investigated. The optimal setup for a bigger imaging depth is a straight configuration with a big amount of LED rows and elements at an angle of 60 degrees. A downside to a bigger LED array is that the configuration uses more space, causing the transducer not to be able to touch the tissue, therefore the size should be taken into consideration during the final design with keeping the aimed target of imaging in mind.

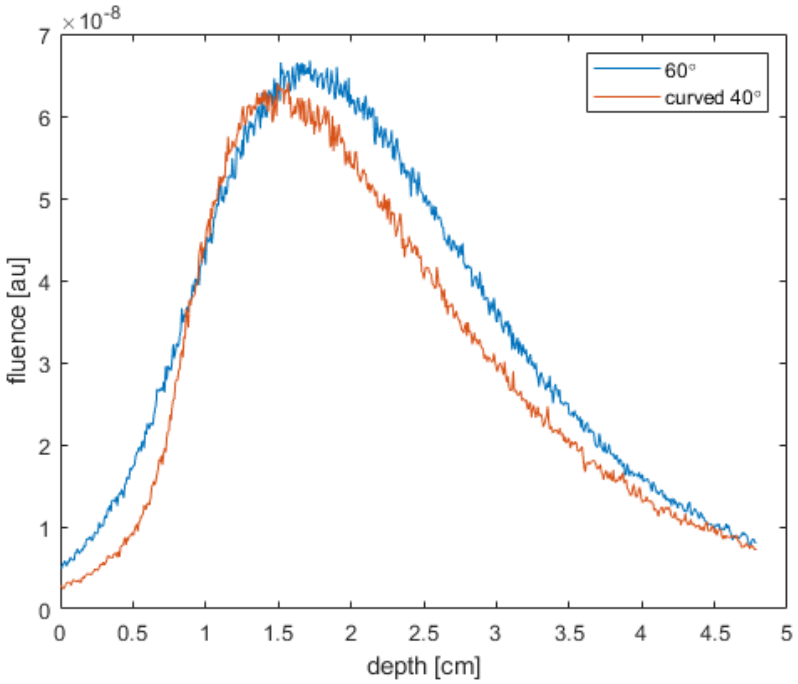

Figure 6.11: The fluence profile of the parallel 60 degree and of the curved array with a curvature of 4 degrees difference between each LED, at an angle of 40 degrees from the first LED row with respect to the transducer.

Chapter 7

Deep learning for enhancement of imaging depth

In this chapter, another approach is used to investigate a possible enhancement of imaging depth. For the use of a handheld photoacoustic system, improvement of the imaging depth increases the usability of the system. This chapter will focus on an approach to improve the imaging depth. Deep learning is relatively new and it is more often used in applications nowadays. The GPUs used for deep learning improve rapidly, causing deep learning to be applied in more fields and applications. In LED-based photoacoustic imaging, the use of deep learning has big potential

Using a deep learning-based general adversarial network (GAN), based on the Pix2Pix [38] algorithm, a program will be trained to recognize signals from a photoacoustic image. When the algorithm proves to work on photoacoustic training images, the photoacoustic test images can be enhanced from higher noise levels to train the algorithm obtained from low light fluence resulting from LED-based illumination.

7.1 Method

The LED-based PA image obtained from an acquisition in combination with the corresponding ultrasound image can be used to increase the imaging depth. In this chapter the open-source GAN pix2pix [39] based framework is used to train a program for the recognition of photoacoustic signals. This algorithm will be explained in detail below. In the algorithm, 2 datasets are used as input to train the algorithm. Noisy photoacoustic images with decay in signal over distance, due to the fluence, are used as input, photoacoustic images without the noise and the influence of fluence decay in the signal are used as a ground truth. The algorithm is trained to predict denoised and fluence independent output images, so the output comes as close as possible to the ground truth images.

7.1.1 Dataset

For the approach of improving the imaging depth, two datasets will be used: Drive database [40], and NNE database [41]. Drive database is a database of 48 images containing segmented vessels images of the retina. The drive vessel images are processed by first making 5 images out of one image, by cropping and rotating the blood vessel image. To this processed image a skin layer is added to the top of every obtained vessel image to mimic extracorporeal handheld imaging. Figure 7.4 shows the pre-processing of the images in this dataset. In this way, a data set of 240 images is obtained.

NNE database [41] is a database, containing 9531 images from 2-Photon Single-Vessel Diameter Measurements from Mouse SI Cortex. An example of the input images from this dataset is shown in figure 7.1a. In the images, it can be observed that the structures are relatively small and do not match with the aimed dimensions (between 7.5 and 0.03 mm [42] [43]) of blood vessels under the skin, like the carotid artery or vessels in the breast. therefore the images of the NNE dataset are zoomed in to 2/3th of the image to obtain proper dimensions of the structures.

A threshold of 18% of the maximum signal intensity is used to obtain a binary image which is used as an input into the k-wave algorithm to obtain photoacoustic images. This threshold was found to be optimal to filter out noise while retaining the structures. Before thresholding, a Gaussian filter is applied to obtain a smooth image without high peaks and so the noise is smoothed and will have less of an influence on the created photoacoustic images. After the preprocessing the images are resized using bilinear resizing, to obtain the original size of 256 x 256 x 3 pixels, which is used as input to obtain the photoacoustic images. Figure 7.4b,c shows a preprocessed image, and in figure 7.4e the obtained photoacoustic image using the K-wave algorithm is shown.

7.1.2 Photoacoustic simulation and reconstruction

For the simulation of the acoustic signal, the MATLAB k-wave toolbox is used [44]. For this simulation, a grid of 512 x 512 is used, to which the images with the initial pressure are scaled. The acoustic detector is a linear array with 128 elements and with a pitch of 0.315 mm. A 7 MHz center frequency gaussian bandpass filter is used with a bandwidth of 80%. The directivity of the transducer is introduced by the finite element size, and a homogeneous medium with a density of 1000 kg/m^3 and a speed of sound of 1500 m/s is used. With this, acoustic k-wave propagation is performed. White noise is added to the simulations, which is varied from 50 to 10 dB with steps of 10 dB, to mimic the noise in measurements. The PA image is

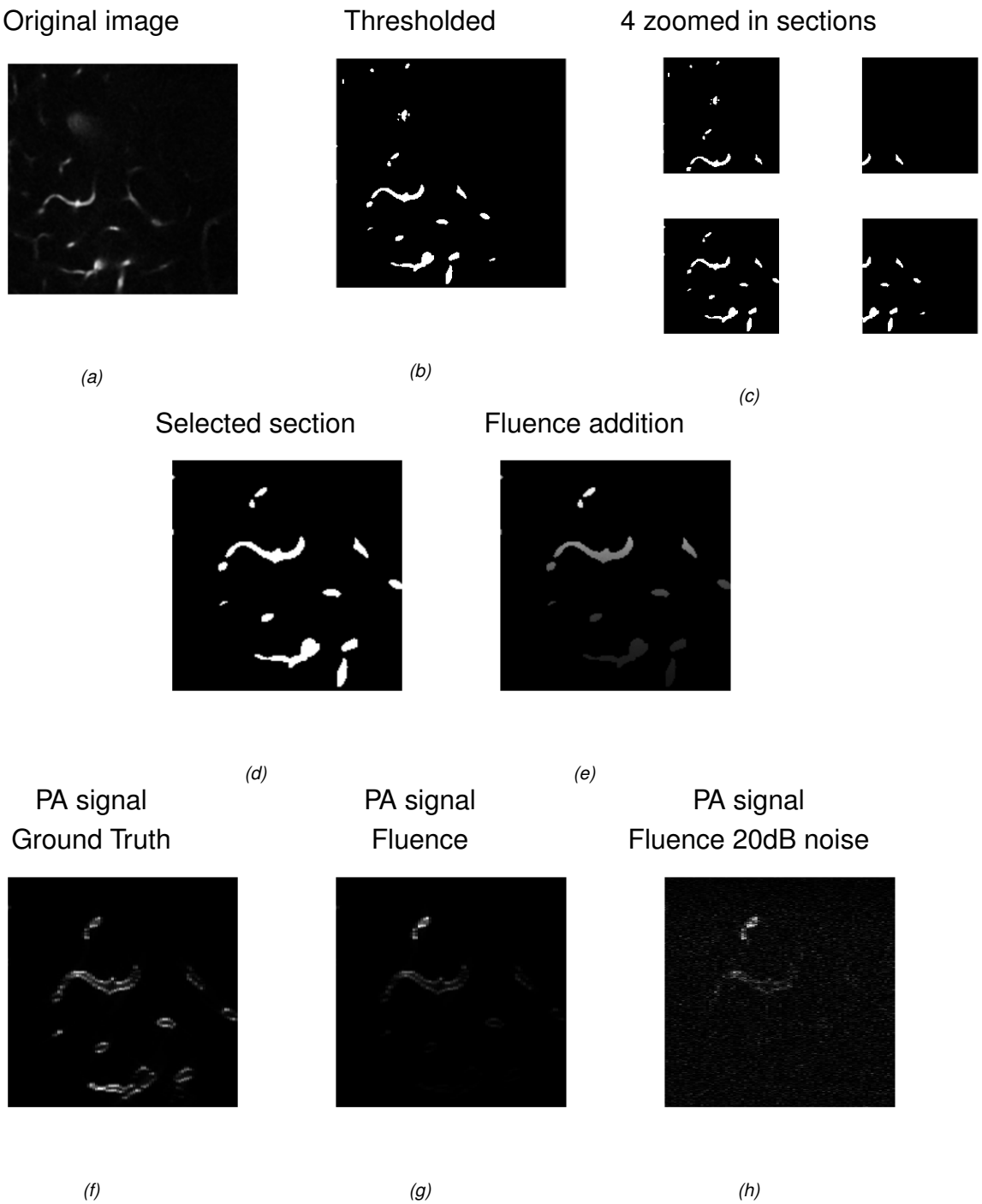

Figure 7.1: Workflow of images generated from NNE dataset, (a) original image, (b) thresholded image, (c) zoomed in sections at 60% of the size of the orriginal image, (d) selected section, (e) fluence addition image, (f) image converted to photoacoustic signal (g) fluence corrected image converted into photoacoustic signal, (h) Photoacoustic image with 20 dB of noise and fluence correction.

reconstructed with a time-reversal algorithm and resized to 256 x 256 pixels. [45]

7.1.3 Monte Carlo simulation to generate fluence map.

During this research, a fluence map is used to correct the images for the decay of fluence due to absorbance and scattering inside a tissue. For the creation of the fluence map, Monte Carlo simulations are used [35] [36].

A model of the LED-based PAI setup is created similar to the model created in chapter 4. The LED arrays are placed 14 mm apart, at an angle of 42 degrees with respect to the transducer, similar to the setup available in the lab. The optical properties used in the simulations are described in table 4.2. The setup is placed in a surrounding of 6.5 x 6.5 x 4.8 cm, which in pixels is: 878 x 878 x 647 pixels. From this, a fluence map is obtained, in which the signal is rescaled between 0 and 1. This fluence map is resized to correlate with the size of the images used (256 x 256 pixels) and multiplied with the images to obtain the input images.

7.1.4 GANs algorithm

The algorithm that is used to train a program to recognize the signal from a potential noisy photoacoustic image, is the open-source Pix2Pix framework [38]. The Pix2Pix software is specialized in the automatic image to image translation, translation of an input image into another image when trained sufficiently. This framework is not application-specific and can be used for many different applications. In earlier work [46], we used a Pix2Pix based framework on photoacoustic blood vessel images. The Pix2Pix framework is a Generative Adversarial Networks (GANs) framework, where a generator and a discriminator work together to “make the output indistinguishable from reality” [46].

GANs work as follows: Images are used as an input in the algorithm, the generator alters these images to look like the ’real’ ground truth images, resulting in a generated dataset. The discriminator has 2 inputs, the ground truth images, and the generated images. The discriminator tries to distinguish the ’real image’, ground truth image from those two images, while the generator tries to fool the discriminator. In this way, the generator is trained to alter the images so it matches the real input closely. The architecture of GANs is shown in figure 7.3

The generator is based on a U-Net architecture with skip connections, in which the input structure is aligned with the output structure. For the discriminator, a convolutional ’PatchGan’ classifier is used, which tries to classify whether patches of

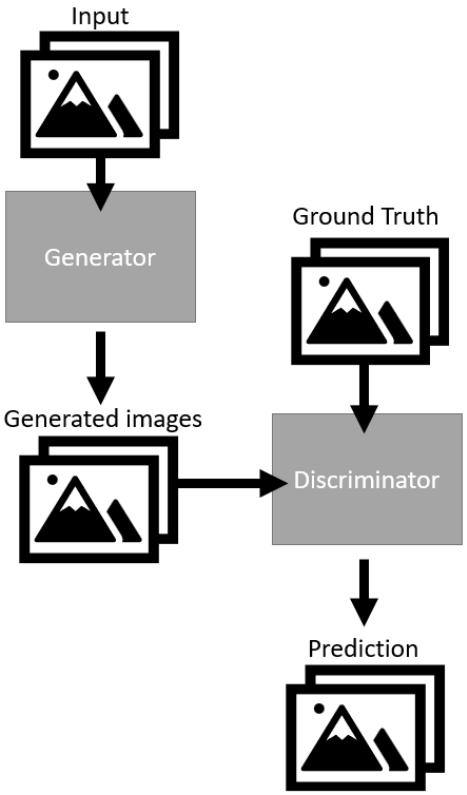

Figure 7.2: Generative adversarial network (GANs) block diagram.

N x N are real or fake, until the entire image is scanned, and penalizes structure at the scale of these image patches. The loss function has the real image and the generated image as input. From the real images, the sigmoid cross-entropy loss is used, which are ones. For the generated images this sigmoid cross-entropy loss is zero. The sum of the real and generated loss results in the total loss. [38]

7.1.5 Workflow

Two datasets are available for the examination of this algorithm, which could improve the imaging depth in photoacoustic imaging signals. Both datasets should mimic photoacoustic signals from blood vessels in the tissue. The images from the datasets are converted to photoacoustic images using a K-wave propagation program in Matlab. These images were used as input into the deep learning algorithm. The input images have a size of 256 x 256 x 3 pixels.

Converting the datasets is done using the k-wave toolbox in Matlab [44], the input and ground truth datasets are obtained, which are used to train the algorithm for the detection of photoacoustic signals. The ground truth dataset is obtained by converting the preprocessed dataset images as shown in figure 7.4b. This results in

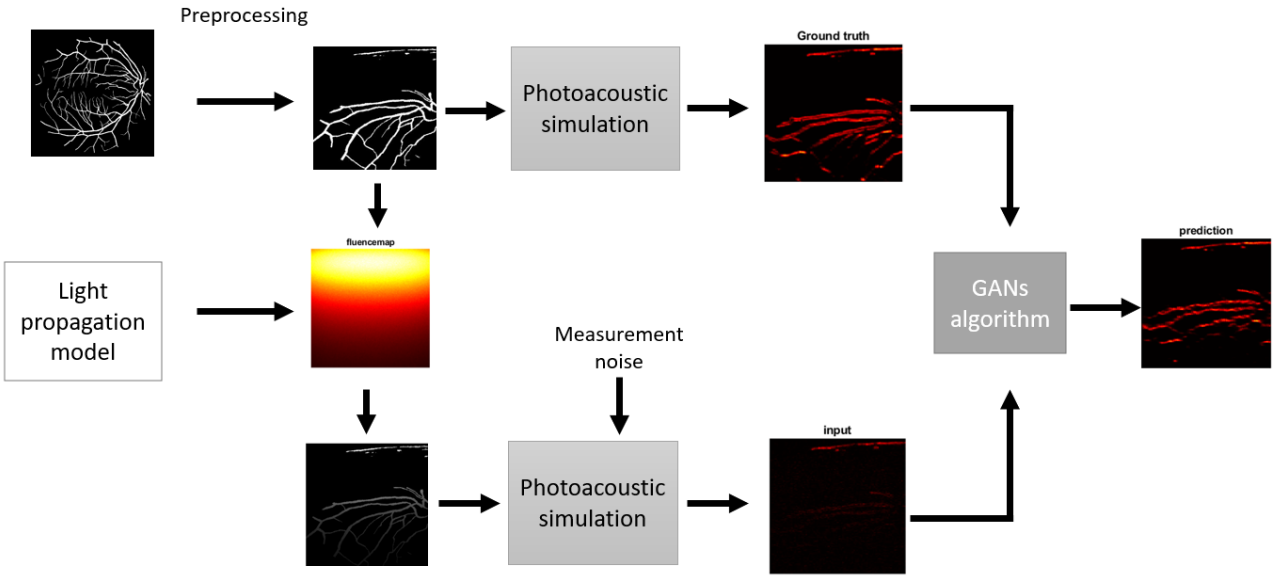

Figure 7.3: Workflow of the preprocessing and training of the GANs algorithm.

a photoacoustic image as shown in figure 7.4e. The entire dataset is converted to photoacoustic images and used as a ground truth input into the algorithm.

Obtaining Photoacoustic images using a LED-based photoacoustic system, the distribution of the light in the tissue, and the intensity of the photoacoustic signal are highly related. The photoacoustic signal from deeper in the tissue is therefore much lower than closer to the surface. To compensate for the signal decay, a fluence map is used to correct this and obtain a more realistic photoacoustic signal which can be used as an input in the algorithm. A fluence map to compensate for the decay in light intensity is obtained using the simulations with 2 LED arrays described in chapter 4, with the tissue properties in table 4.2 with an angle of the LED arrays of 42 degrees, similar to the setup available in the lab. The fluence map obtained is shown in figure 7.4d, this map is multiplied with the images of the reprocessed dataset, as shown in figure 7.4b to obtain a dataset with the influence of a light source, with images with a decaying signal, as can be seen in figure 7.4c. This input image, influenced by a light source, is similar to the ground truth dataset converted with the K-wave propagation program to a photoacoustic image.

In the GANs algorithm, different training sessions will be executed with different noise levels, because in photoacoustic images noise is involved. Therefore, the photoacoustic images with different levels of noise are used as input into the deep learning algorithm to evaluate the performance of different qualities of images. The noise is added to the rf data (raw time data obtained from the transducer output) of the datasets using the k-wave propagation, to mimic measurement noise, this noise

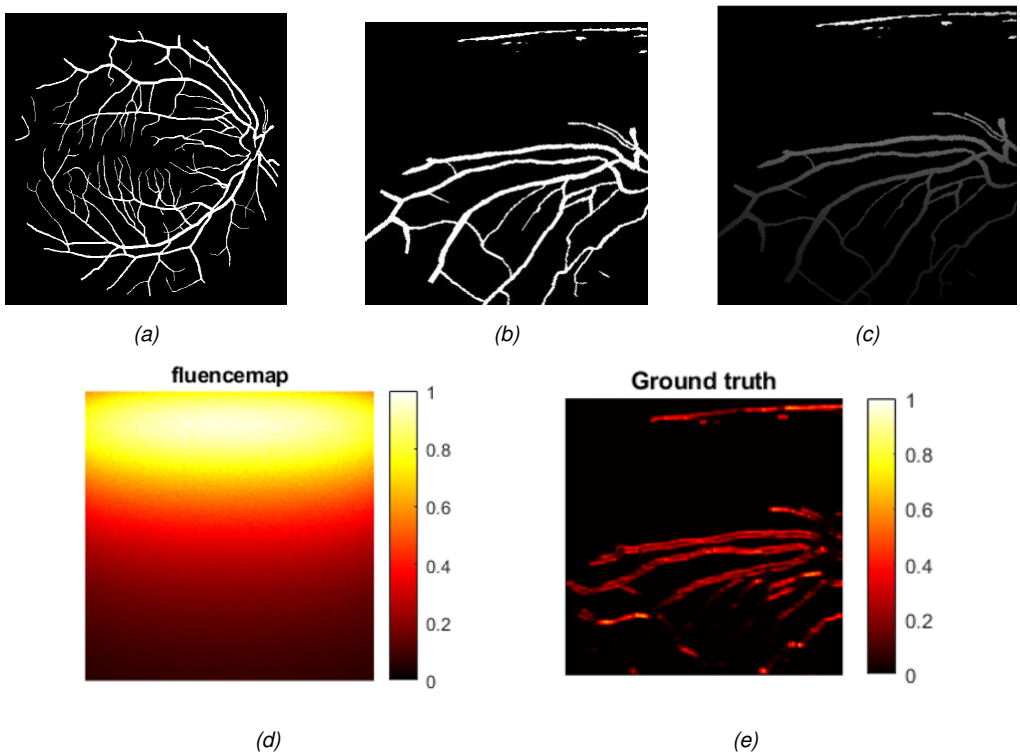

Figure 7.4: (a) vessel image of the retina (b) the original optical nerve image is rotated, cropped and a skin layer is added, (c) the fluence map used for implementation and compensation of fluence, (d) the image in b is multiplied with the fluence map to mimic an image with the influence of the illumination, (e) input image converted to a photoacoustic image using K-wave propagation.

is varied from 50 to 10 dB of noise in steps of 10 dB, obtaining a total of 5 input datasets with different noise levels.

When the datasets are prepared, they can be used to train and test the deep learning GANs algorithm. To do this, the dataset needs to be divided into a training set and a test set. The Drive dataset is divided into a train set of 80% of the images and the test set has a size of 20% of the images, 192 and 48 images respectively. The NNE database consists of 9531 images, which are divided into a training set of 6355 images and a test set of 3176 images, 67%, and 33 % respectively. The division is done by randomly selecting the predetermined amount of images to be the test set. The not selected images are assigned to function as the training set. This selection is used throughout this research, so the results can be compared without an influence of a change in the test and training set.

7.1.6 Quality metrics

For the determination of the quality of the images, three different metrics are used. The result of the images obtained is compared using: Structural similarity index measure (SSIM), peak signal to noise ratio (pSNR), and sharpness.

The pSNR is described as:

$$pSNR = 10log_{10}\left(\frac{MAX_I^2}{MSE}\right) \tag{7.1}$$

with

$$MSE = \frac{1}{M * N}\sum_{i=1}^{M}\sum_{j=1}^{M}||f_{ij} - g_{ij}||^2 \tag{7.2}$$

where MAX_i is the maximum signal value in the image. With a reference image f and a test image g, with size M×N.

Another quality metric is the structural similarity index measure (SSIM). The SSIM evaluates the difference between two images, described as follows:

$$SSIM(f,g) = [l(f,g)]^{\alpha}[c(f,g)]^{\beta}[s(f,g)]^{\gamma} \tag{7.3}$$

where:

$$l(x,y) = \frac{2\mu_f\mu_g + C_1}{\mu_f^2 + \mu_g^2 + C_1}$$

$$c(x,y) = \frac{2\sigma_f\sigma_g + C_2}{\sigma_f^2 + \sigma_g^2 + C_2}$$

$$s(x,y) = \frac{\sigma_{fg} + C3}{\sigma_f\sigma_g + C3}$$

where: μ is the average, σ is the variance, and $\sigma_{fg}$is the covariance, where f is the reference image and g is the test image. α, β and γ are weight factors, which are set to 1.

For another comparison of the results, sharpness is used. The sharpness gives a measure of the quality of the images. The computation of the sharpness is done using the Brenner gradient. The Brenner gradient computes the difference between

a pixel value and its neighbors two points away. In two dimensions, this can be written as

$$F_{brenner} = \sum_{x,y} (f_{x+2,y} - f_{x,y})^2 + (f_{x,y+2} - f_{x,y})^2 \tag{7.4}$$

where $f_{x,y} \equiv f(x, y)$ is the gray-level intensity of the pixel at (x, y). [47]

The similarity changes over depth, therefore, the SSIM values are calculated for different layers in the images. The image is divided into 32 segments, from the top of the image to the bottom, as shown in figure 7.5 The SSIM is calculated for each layer, this was done for all images in the testing set and is used for comparison.

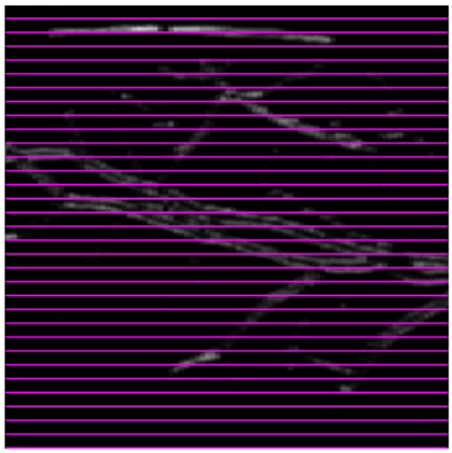

Figure 7.5: The PA images are divided in 32 sections, shown with the magenta lines. For every section the SSIM is determined.

7.1.7 Validation with experimental data

The model created is tested using experimental data. A selection of 3 images from the test set of the Drive dataset and 3 images from the test set from the NNE dataset has been used to create a phantom. This phantom is used for testing the algorithm with images obtained using the PAI system, AcousticX (Cyberdyne Inc., Tsukuba, Japan).

The obtained images from the PAI system are resized to the size of the images used in the GANs algorithm, at a size of 256x256 pixels, and tested with the trained algorithms for the Drive and NNE databases.

Experiments were conducted to test and validate the trained GANs network. We used the AcousticX system with two LED arrays next to the probe, 850 nm and a 7 MHz, 128 element transducer for the image. Six test images, three from DRIVE and three from NNE datasets were selected to make experimental phantoms. Impressions of the test images were made on plastic cling film of 12 µm thickness. A black permanent marker (Pendel LTD. Japan) was used to draw the vessel structures on the film to form the test objects. The film with the test image was then mounted on a holder in the imaging plane of the transducer.

Two measurements were conducted for each test object, one with water as a medium and another in tissue-mimicking phantom solution. The phantom solution was prepared with an absorption coefficient of 0.3 cm^{-1} and a reduced scattering coefficient of 6.5 cm^{-1} at 850 nm, by adding 285 µl of Indian ink (Royal Talens, Netherlands) and 20 % intralipid (Fresenius Kabi, Germany) to 6 L of water.

Photoacoustic images were obtained with a LED pulse repetition rate of 4 kHz and with a frame averaging of 6400. Images obtained with water as a medium are used as ground truth given that light from the LED can illuminate the entire sample in a non-scattering medium. Photoacoustic images obtained in phantom solution were resized to the right dimensions and used to test the already trained GANs. The predicted images are then compared with the images obtained in water to see how well the GANs predicted the structures at larger depths. SSIM and PSNR of the predicted images were also computed against images obtained in water to analyze the predicted image quality.

7.2 Results

The GANs algorithm has been trained using the ground truth data set and the input datasets with different noise levels in different training sessions. In figure 7.6 a testing image is displayed for every noise level. For every noise level, four images are displayed, the first image shows the input image from which the algorithm predicts what the output should be. The second image is the ground truth image, and the third image is the prediction, which is the output image from the algorithm. Ideally, the prediction would exactly match the ground truth. The fourth image is the fluence compensated image, which is compared to the results predicted by the GANs algorithm to see if the algorithm gives better results than a relatively easy fluence compensation method. This image is obtained by using the input image on the left and dividing this with the fluence map of figure 7.4d.

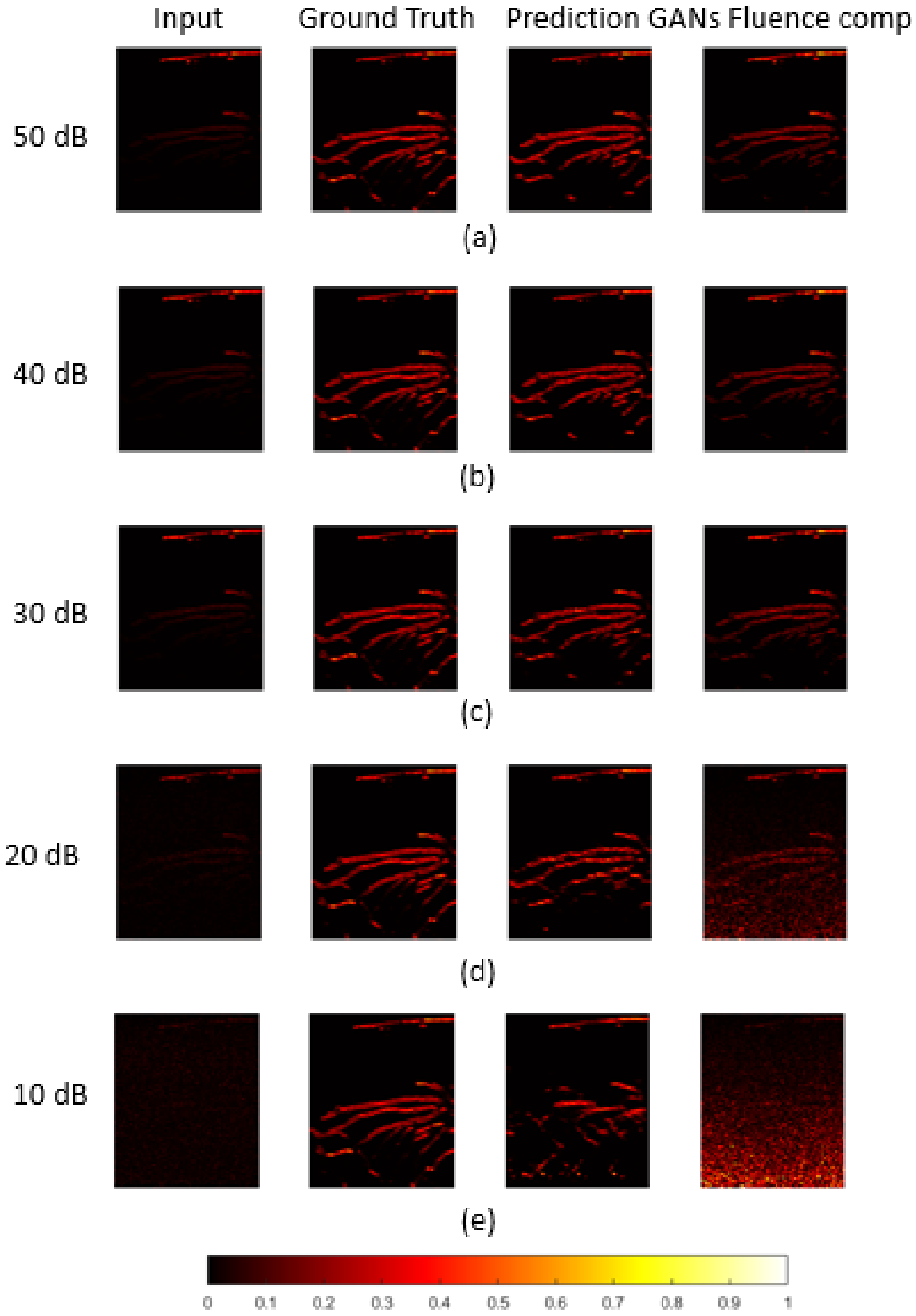

Figure 7.6: PA signal of the input, ground truth, output from GANs algorithm and fluence compensaton images from the Drive dataset for noise levels of (a) 50 dB (b) 40 dB (c) 30 dB (d) 20 dB (e) 10 dB.

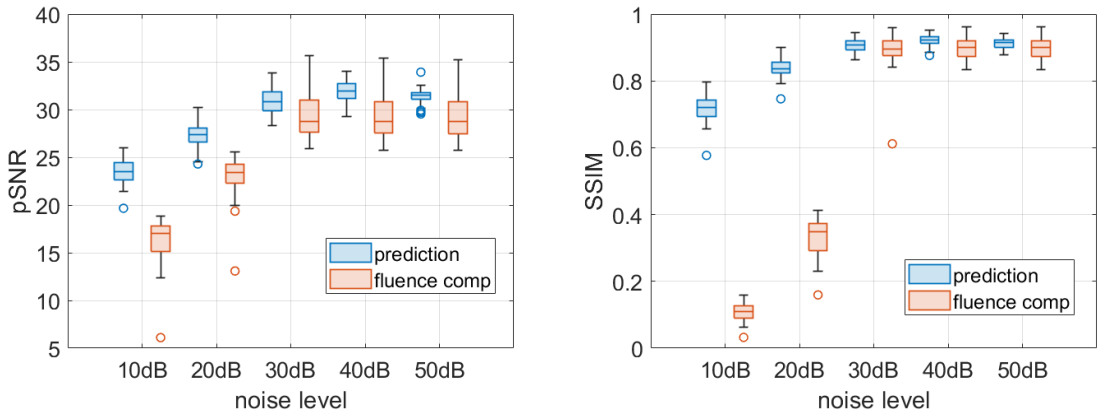

Figure 7.7: Drivedataset: (a) pSNR (b) SSIM of the GANs algorithm, blue. The fluence compensated image, red, for noise levels from 10 to 50 dB.

7.2.1 Drive dataset

For evaluation of the results from the Drive dataset, the pSNR and the SSIM are used. The results of these metrics, for every noise level, are displayed in figure 7.7 and table 7.1 for the predicted and the fluence compensated images. Figure 7.7a shows that with a higher noise level the pSNR decreases for both the fluence compensated images and the predicted images. The median of the pSNR of the fluence compensated images is slightly lower than the predicted images at 50, 40, and 30 dB noise, but from 20 dB the pSNR decreases more rapidly and the predicted median pSNR at 10 dB noise is the same as the fluence compensated median pSNR at 20 dB.

Table 7.1: Median of the pSNR and SSIM from the drive dataset for noise levels from 10 to 50 dB.

	10 dB	20 dB	30 dB	40 dB	50 dB
pSNR predicted	23.5	27.4	30.8	31.9	31.5
pSNR fluence comp	17.0	23.4	28.8	28.8	28.7
SSIM predicted	0.719	0.836	0.909	0.921	0.915
SSIM fluence comp	0.110	0.348	0.896	0.900	0.900

Figure 7.7b shows the SSIM of the fluence compensated and predicted images. Similar to pSNR, for 50, 40, and 30 dB the median SSIM is stable for both fluence compensated and predicted images. The prediction decreases to 0.72 at 10 dB

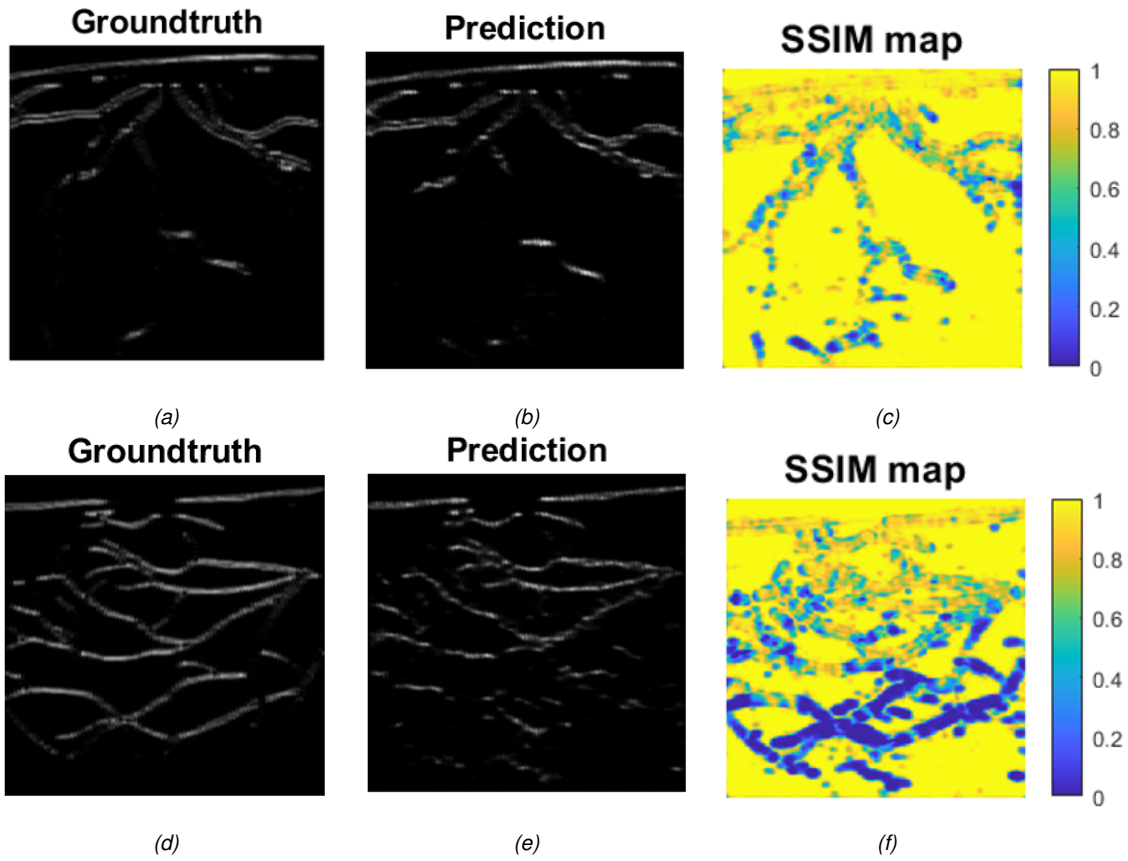

Figure 7.8: Drive dataset: SSIM comparison prediction to Ground truth at 20dB, (a,b,c) SSIM score of 0.90, (c,d,e) SSIM score of 0.75.

noise, while the fluence compensation decreases significantly to 0.11. Images with low and high SSIM are displayed in figure 7.8, where the SSIM between the ground truth and the prediction of the 20 dB fluence images result in a high score of 0.90 for the upper images and a lower score of 0.75 for the bottom images.

Figure 7.9 shows the boxplot of the sharpness from the input, ground truth, prediction, and fluence compensated images in the Drive test set. In these input images, the fluence is included and a noise level is added. The region in green shows the sharpness of the ground truth and is used to compare the other results too. The medians of the sharpness for every case and noise level are displayed in table 7.2.

Figure 7.10 shows two predicted images, the highest sharpness of 527 in 7.10a, and the lowest sharpness of 159 in figure 7.10b for the 50 dB predicted images. When looking at the input, the results show that the sharpness of the images is 2.5 times smaller than the sharpness of the ground truth, and at noise levels of 50 dB, 40 dB, and 30 dB the sharpness is constant, but noise levels of 20 and 10 dB result in a sharpness halved compared to the lower noise levels. When looking at the sharpness of the predicted images, it can be observed that the sharpness of the

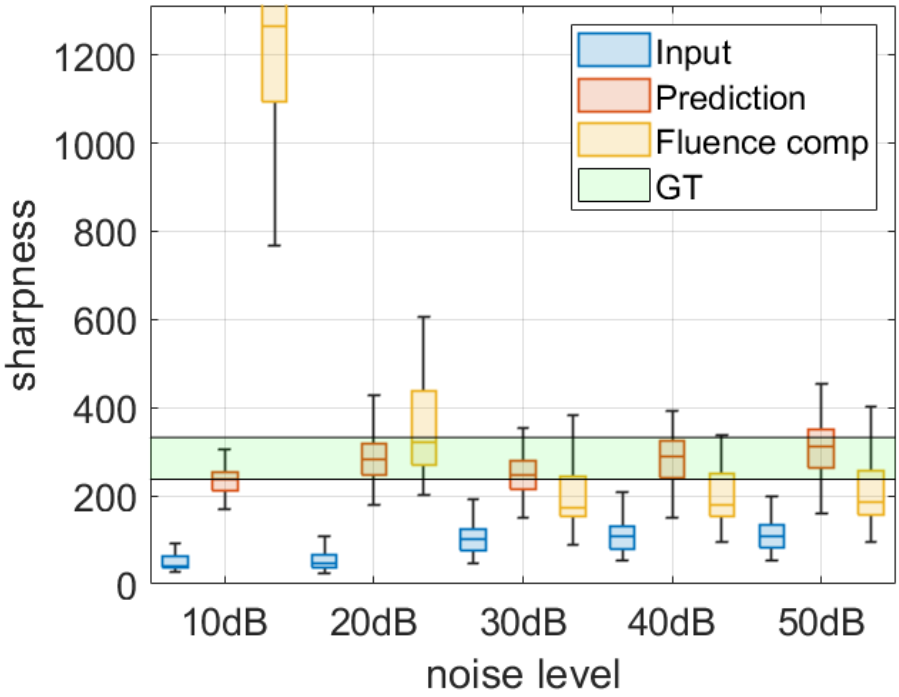

Figure 7.9: Boxplot of the sharpness from the Drive dataset, for the input, fluence compensated and predicted images. The ground truth displayed as the green bar.

predicted image is close to the sharpness of the ground truth, with a slight fluctuation. Observing the fluence compensation in figure 7.9 the sharpness is lower than the ground truth image by a factor of 1.5, for noise levels of 50, 40, and 30 dB. When the noise is increased to 20 and 10 dB, the sharpness increases rapidly, this is due to relatively sharp noisy pixels, occurring frequently, as shown in figure 7.11, but this does not show an improved image.

The SSIM evaluates the difference between two images, this can be evaluated in a single value, but also an image. The SSIM map of the difference between the input

Table 7.2: Median of the sharpness from the drive dataset for noise levels form 10 to 50 dB, for the ground truth, input, prediction and fluence compensation.

Noise	10 dB	20 dB	30 dB	40 dB	50 dB
Input	41.9	46.7	101.5	107.2	109.6
Ground truth	280.8	280.8	280.8	280.8	280.8
Prediction	236.5	283.7	248.8	288.4	310.5
Fluence compensation	1265.9	320.6	173.5	180.7	184.5

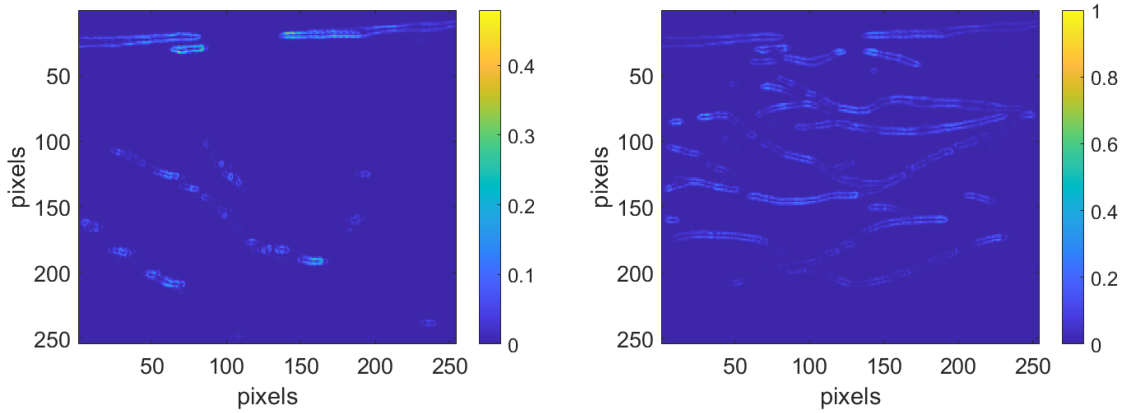

Figure 7.10: Drive dataset: 50 dB prediction, (a) sharpest with a score of 528, (b) least sharp with a score of 159.

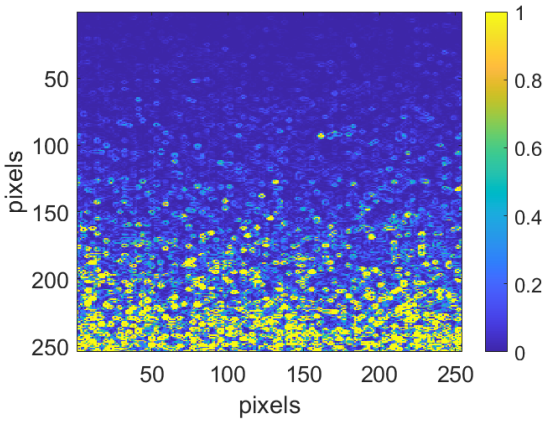

Figure 7.11: The sharpness map of the fluence compensated image with the highest sharpness, with a score of 17675. The sharpness originates from the noise in the image.

and the output image is shown in figure 7.12a, the difference between the ground truth and the fluence compensated image is shown in figure 7.12b. In these results values that are close to 0 show a big difference between the two images that are compared. In these images, it stands out the darker values are visible at the bottom of the image. Values are closer to 0, so displayed darker, showing that there is more difference between the ground truth image and the results, indicating that this is a depth-dependent variable.

The Results of the depth-dependent SSIM values are displayed in figure 7.13 for all 5 noise levels. On the left, the results of the GANs algorithm are displayed and on the right, the results of the fluence compensation method are shown.

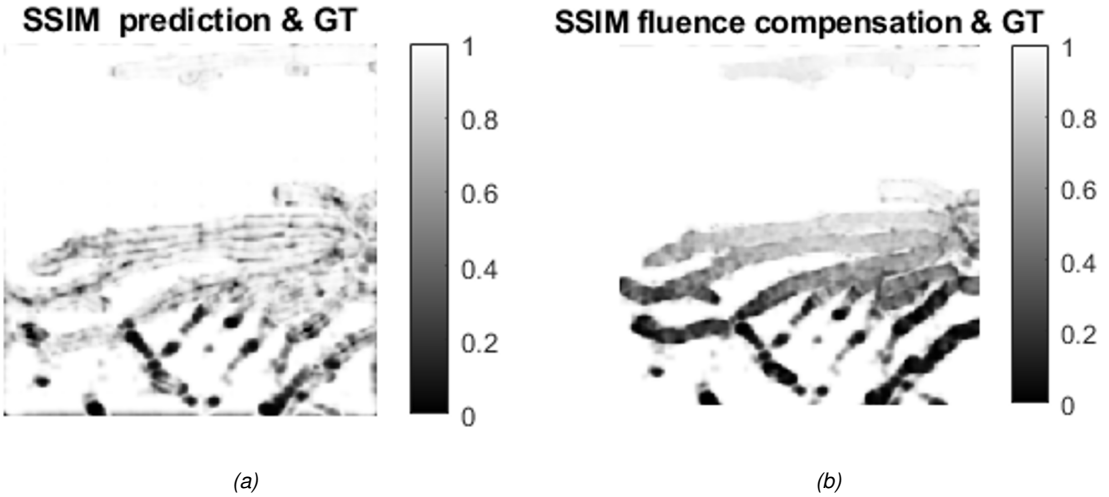

(a) *(b)*

Figure 7.12: Drive dataset: 50 dB prediction, (a)sharpest with a score of 528, (b)least sharp with a score of 159.

Figure 7.13 shows the SSIM results over the depth of the 5 different noise levels, from top to bottom, from 50 to 10 dB of noise. Looking at the results of the lowest noise level of 50 dB, it can be observed that the SSIM value is high, close to 1, so the predictions match the ground truth closely. The prediction from the algorithm is slowly decaying over depth, getting slightly less accurate with an increasing depth.

The prediction of the fluence compensation method in 7.13b shows a dip at 2/3th of the image. The prediction of the fluence compensation method in the upper half of the image is good (almost perfect), however, halfway it becomes less accurate, at the deepest depth, from section 28, it looks from the graph that the prediction becomes better, however, this is not necessarily the case. The input images have a photoacoustic signal, this signal is distributed over the image, but this distribution is not evenly over the entire image. On average there is more signal in the middle of the images and at the bottom of the images, there is on average less photoacoustic signal. Using the SSIM prediction is determined to be a perfect score when the image would be black and it is indeed black. The irregularity in the signal distribution causes the SSIM score at the deepest depth to be relatively high.

The SSIM results show that with an increasing noise level, between 50, 40 and 30 dB there is not much difference in the graphs in figure 7.13a,c,e. The 20 dB results of the algorithm start to show a profile, which is similar to the profile observed in the fluence compensation images, this is also due to the irregular distribution of the signal over the images. The SSIM score starts to decay from the predicted images at a noise level of 20 dB. When looking at the images in figure7.6 differences can be observed between the prediction and ground truth images. The 10 dB results are even worse, especially in the middle of the image. Looking at the images the

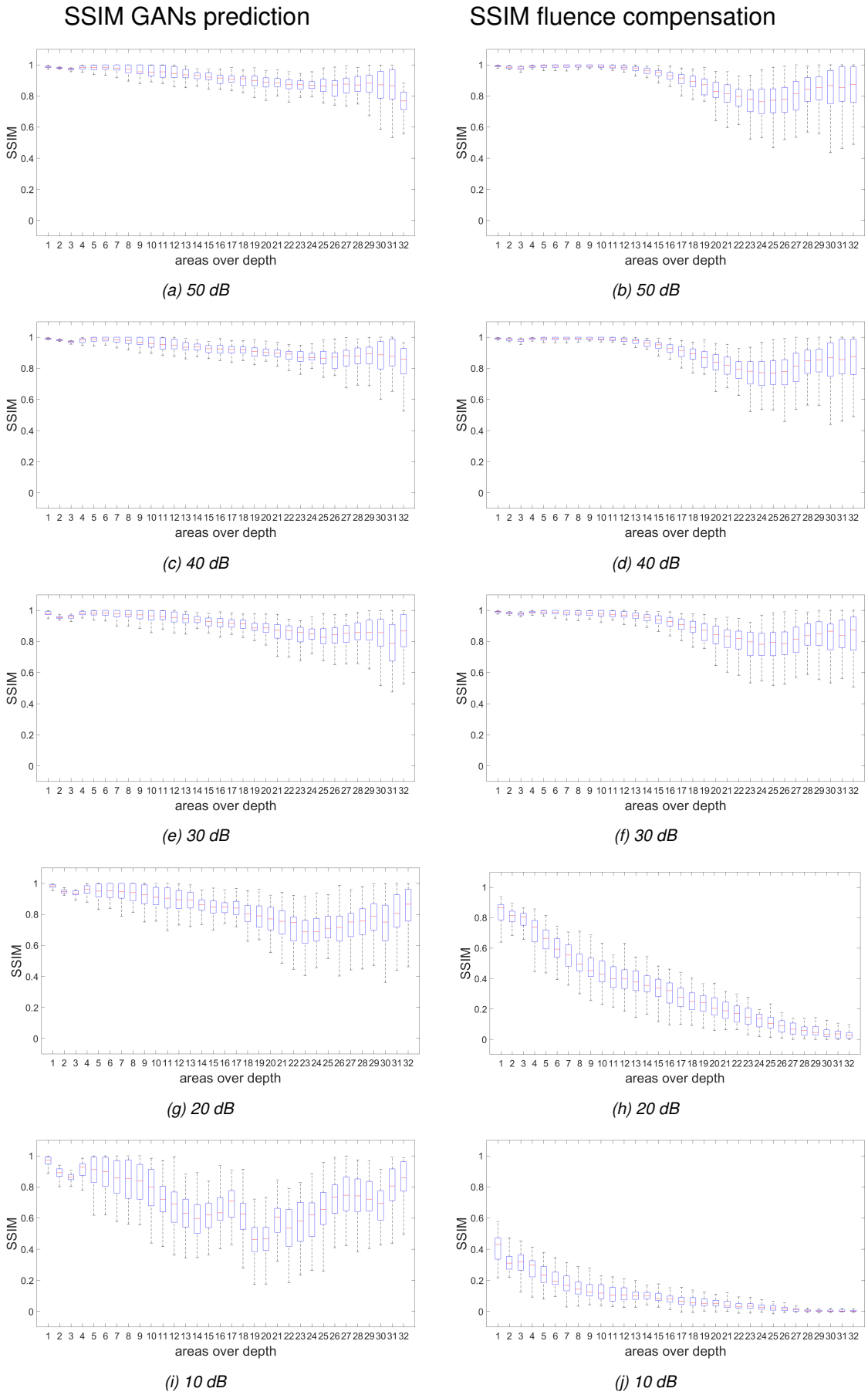

Figure 7.13: The depth dependant SSIM values are displayed for all 5 noise levels. On the left the results of the GANs algorithm are displayed and on the right the results of the fluence compensation method.

prediction of the algorithm corresponds with the SSIM value, and the image does not correspond to the ground truth, except for the top. In this image, a rercuring structure can be observed just below the middle.

The SSIM scores of the fluence compensated image show a constant prediction until a noise level of 30 dB. With higher noise levels, the noise is becoming prominent and a fluence compensation method does not improve the signal anymore. In the images can be observed that only noise is shown, instead of the signal originating from the structures in the images.

7.2.2 NNE dataset

After using the drive database, consisting of 240 images, a larger database, the NNE database has been used. The NNE database consists of 9531 images which are divided into a training set of 6355 images and a test set of 3176 images, separated randomly. The GANs based deep learning algorithm has been trained using the ground truth data set and the input datasets with different noise levels in different training sessions, similar to before. In figure 7.14 a testing image is displayed for every noise level. For every noise level, four images are displayed, the first image shows the input image from which the algorithm predicts what the output should be. The second image is the ground truth image, and the third image is the prediction, which is the output image from the algorithm. Ideally, the prediction would exactly match the ground truth. The fourth image is the fluence compensated image, which is compared to the results created by the GANs algorithm to see if the algorithm gives better results than a relatively easy fluence compensation. This image is obtained by using the input image on the left and dividing this with the fluence map.

SSIM and pSNR are used for the evaluation of the accuracy of the prediction. The results of this are shown in figure 7.3 and table 7.3.

Figure 7.7a shows the SSIM of the fluence compensated and predicted NNE images. For 50, 40, and 30 dB the median SSIM is mostly constant around x for both fluence compensated and predicted images. The prediction decreases slightly, to 0.90 at 10 dB noise, while the fluence compensation decreases significantly to 0.27.

Figure 7.15b shows that with a higher noise level the pSNR decreases for both the fluence compensated images and the predicted images. The median of the pSNR of the fluence compensated images is slightly lower than the predicted images at 50, 40, and 30 dB noise, but from 20 dB the pSNR decreases more rapidly and the predicted median pSNR at 10dB noise is close to the fluence compensated

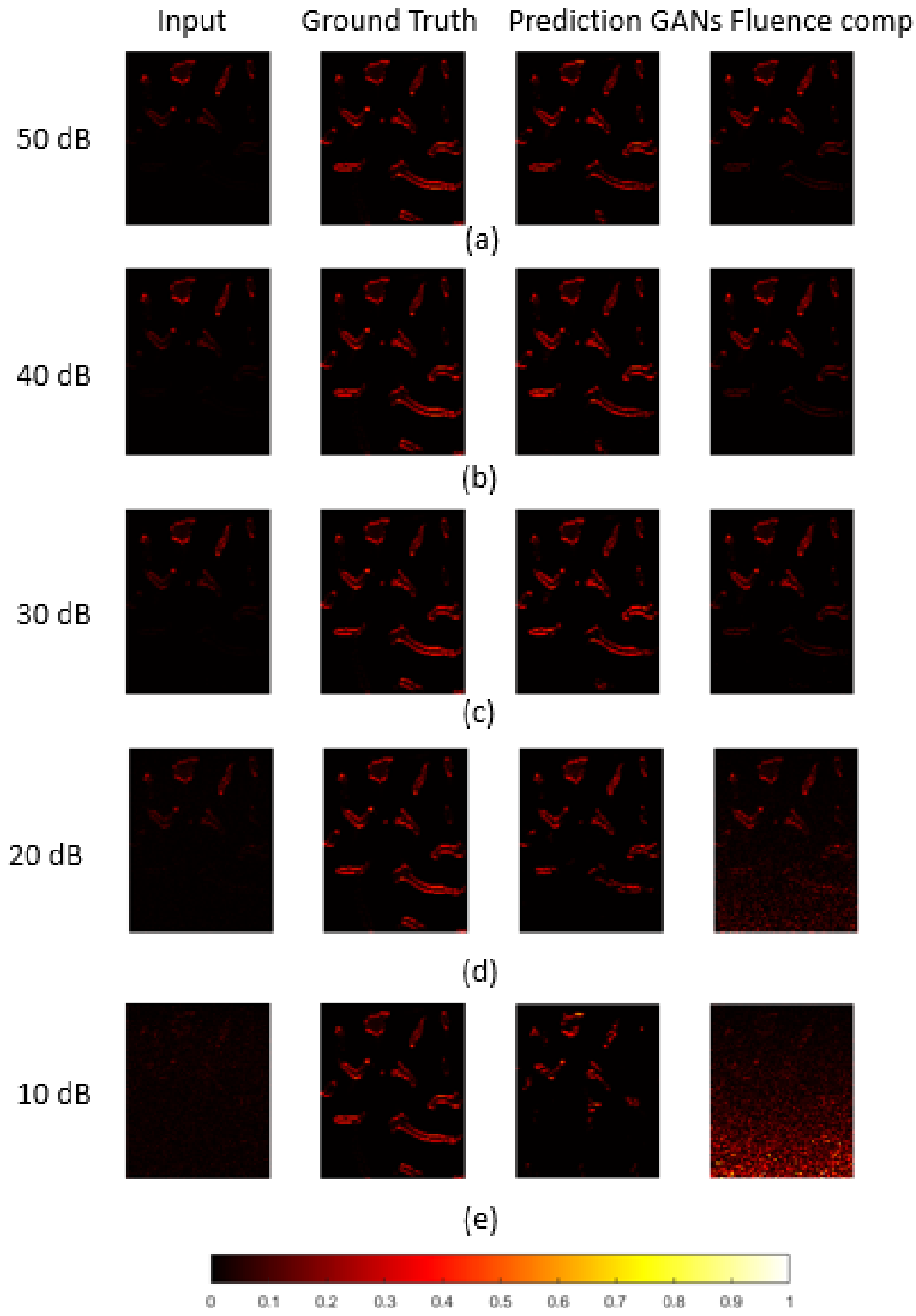

Figure 7.14: PA signal of the input, ground truth, output from GANs algorithm and fluence compensation images from the NNE dataset for noise levels of (a) 50 dB (b) 40 dB (c) 30 dB (d) 20 dB (e) 10 dB.

median pSNR at 20 dB.

Table 7.3: Median of the pSNR and SSIM from the NNE dataset for noise levels from 10 to 50 dB.

	10 dB	20 dB	30 dB	40 dB	50 dB
pSNR predicted	30.4	36.1	39.2	40.1	37.8
pSNR fluence comp	24.0	31.9	35.8	35.7	35.7
SSIM predicted	0.900	0.952	0.974	0.974	0.950
SSIM fluence comp	0.270	0.704	0.961	0.961	0.961

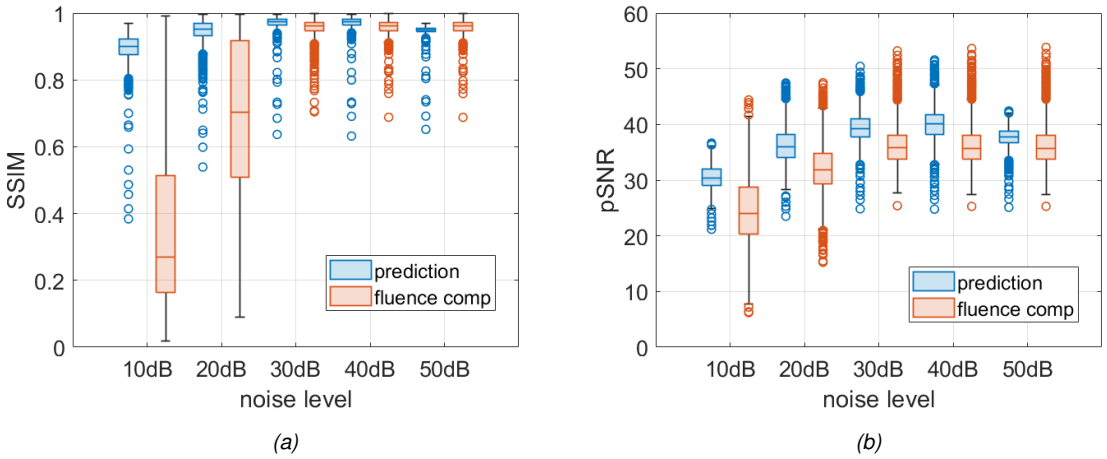

Figure 7.15: NNE database: (a) SSIM (b) pSNR of the GANs algorithm for varying noise levels.

Figure 7.16 shows the boxplot of the sharpness from the input, ground truth, prediction, and fluence compensated images in the Drive test set. In these input images, the fluence is included and a noise level is added. The region in green shows the sharpness of the ground truth and is used to compare the other results too. The medians of the sharpness for every case and noise level are displayed in table 7.4.

When looking at the input, the results show that the sharpness of the images is 3.2 times smaller than the sharpness of the ground truth, and noise levels of 50 dB, 40 dB, and 30 dB do are constant, but noise levels of 20 and 10 dB result in a sharpness decreases at the lower noise levels. When looking at the sharpness of the predicted images, it can be observed that the sharpness of the predicted image is close to the sharpness of the ground truth, with a slight fluctuation, there is no clear trend distinguished from this.

Observing the fluence compensation in figure 7.9, the sharpness is lower than the ground truth image by a factor of 1.6, for noise levels of 50, 40, and 30 dB, when

Table 7.4: Median of the sharpness from the NNE dataset for noise levels form 10 to 50 dB for the ground truth, input, prediction and fluence compensation.

	10 dB	20 dB	30 dB	40 dB	50 dB
Input	12.0	14.2	20.0	20.5	20.8
Prediction	62.1	55.1	71.3	59.8	80.2
Fluence compensation	334.4	70.6	41.0	41.4	42.0
Ground truth	67.4	67.4	67.4	67.4	67.4

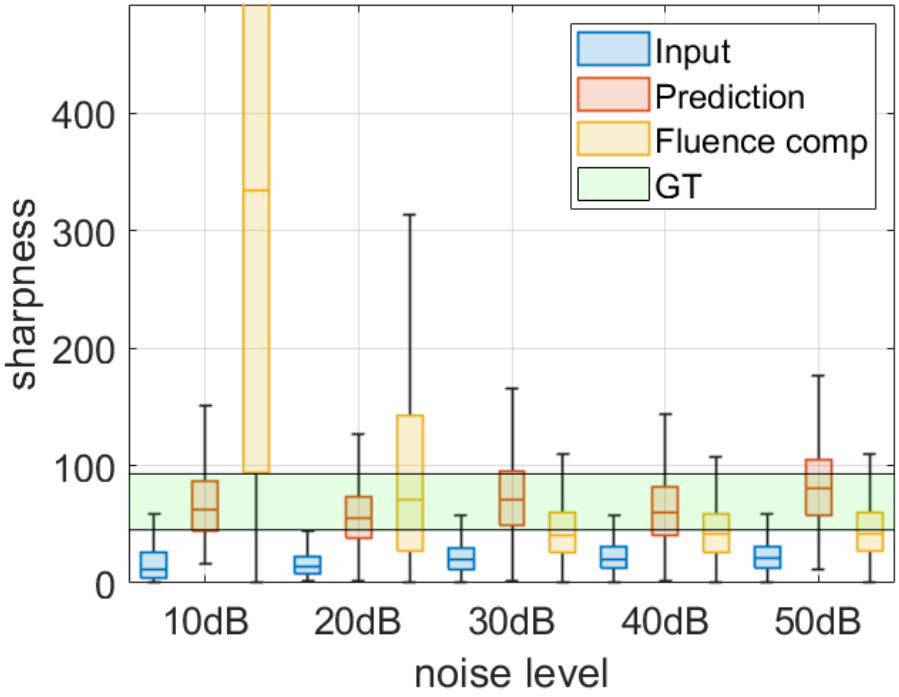

Figure 7.16: Boxplot of the sharpness from the NNE dataset, for the input, fluence compensated and predicted images. The ground truth displayed as the green bar.

the noise is increased further, the sharpness increases rapidly, this is due to relatively noisy pixels but does not show an improved image.

Because of the depth-dependent quality of the images, the SSIM over 32 sections is taken, as was done before in the drive dataset. The boxplots for the NNE dataset are displayed in figure E.12 from 50 to 10 dB of noise.

At a noise level of 50 dB, it can be observed that there is a high SSIM throughout the image for both the fluence compensated and predicted image. In the fluence compensated dataset, from halfway through the image, there is a slightly lower SSIM observed, while the SSIM of the predicted images is higher, compared to the fluence

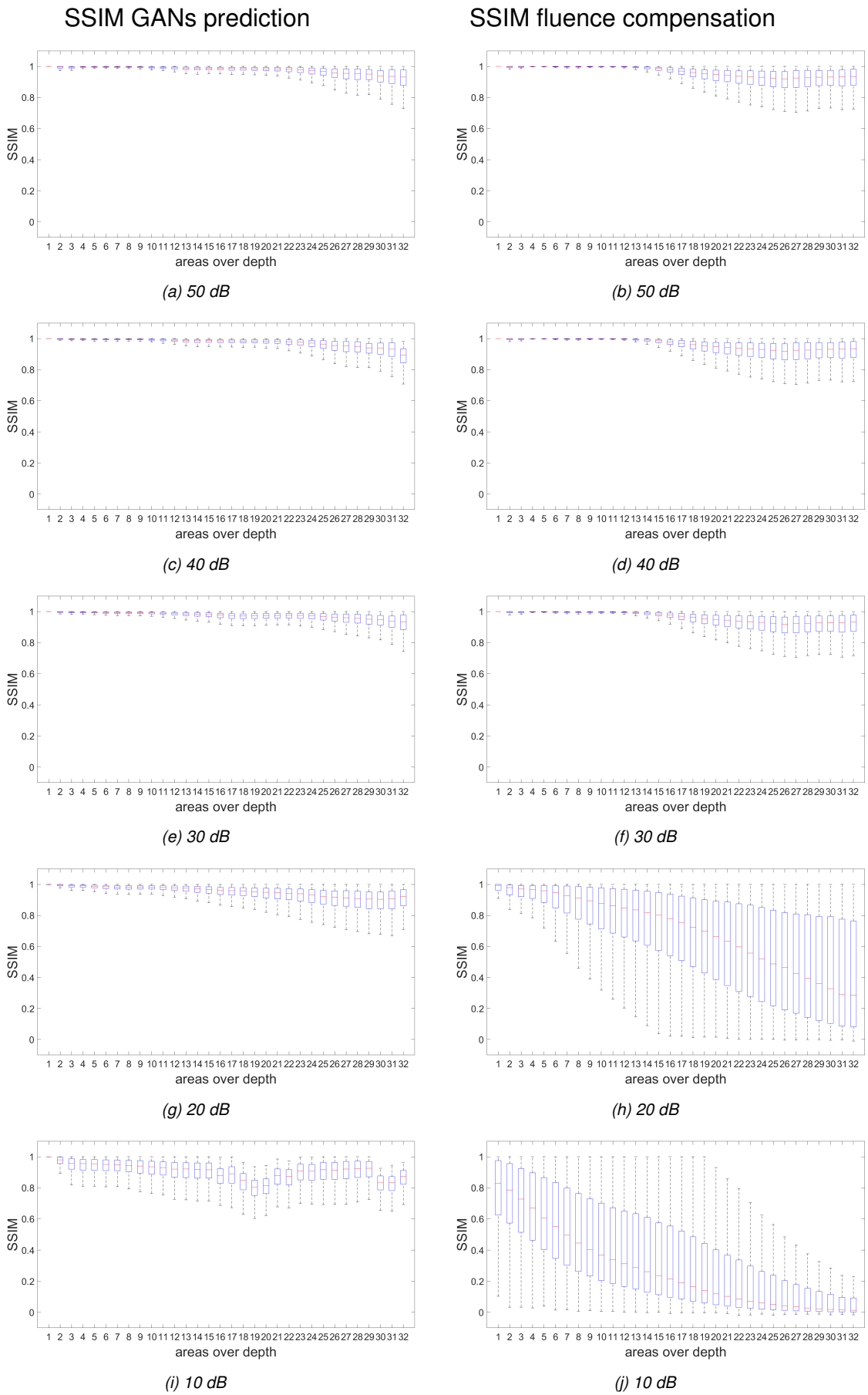

Figure 7.17: The depth dependant SSIM values are displayed for all 5 noise levels. On the left the results of the GANs algorithm are displayed and on the right the results of the fluence compensation method.

compensated images and only at the end decreases slightly. The SSIM results show that with an increasing noise level, between 50, 40, and 30 dB the scores remain constant. The 20 dB results of the predicted images are still similar to the results of the predicted images in the previous noise levels, the SSIM values start to decrease slightly, but are still high, above 0.9. The fluence compensation at 20 dB, shown in figure 7.14h shows an entirely different plot. Where until 30 dB the results were similar, now it is clear that the SSIM values start to decay rapidly lower in the image. The noise multiplied with the fluence map is showing, resulting in a big influence on the SSIM. The 10 dB results of the fluence compensated images are even worse, and the decay in SSIM is even happening throughout the image. For the predicted dataset at 10 dB, shown in figure 7.14i, the SSIM is still relatively high, above 0.8, but there shows some irregularity and a dip in the middle of the image around section 10, and at the end from section 29 becomes apparent.

7.2.3 Validation with experimental data

Experiments are executed to validate the model. For these experiments, 3 images from the Drive test set and 3 images from the NNE test set were selected and transformed from the input image into a phantom, shown in figure 7.18. The phantom was placed in a tank filled with water and a tissue-mimicking phantom. The PA image obtained in the tissue-mimicking phantom is used to test the trained algorithm and is displayed in figure 7.18 on the left. All the results of every phantom at the different averaging levels are shown in appendix E

The trained GANs algorithm from both the Drive dataset for P1-P3 and the NNE dataset for P8, P9, and P11, trained for a noise level of 20dB, is used to investigate whether it could obtain more information from the image than is visible to the observer. The PA image obtained in a tissue-mimicking phantom is used as an input in the model, and compared to the results obtained in water. For evaluation of the results, the pSNR and SSIM are investigated.

From the results in table 7.5 it can be observed that the results of both the SSIM and pSNR of the Drive images P1-P3 are on average lower than the results of the NNE images P8, P9, and P11. This can be explained by the amount of signal originating from the vessels in the images, where the amount of signal from the NNE dataset is sparse with respect to the Drive dataset.

Comparing the results of the phantom metric and the prediction metrics in table 7.5, it can be observed that the SSIM values of the prediction images are lower

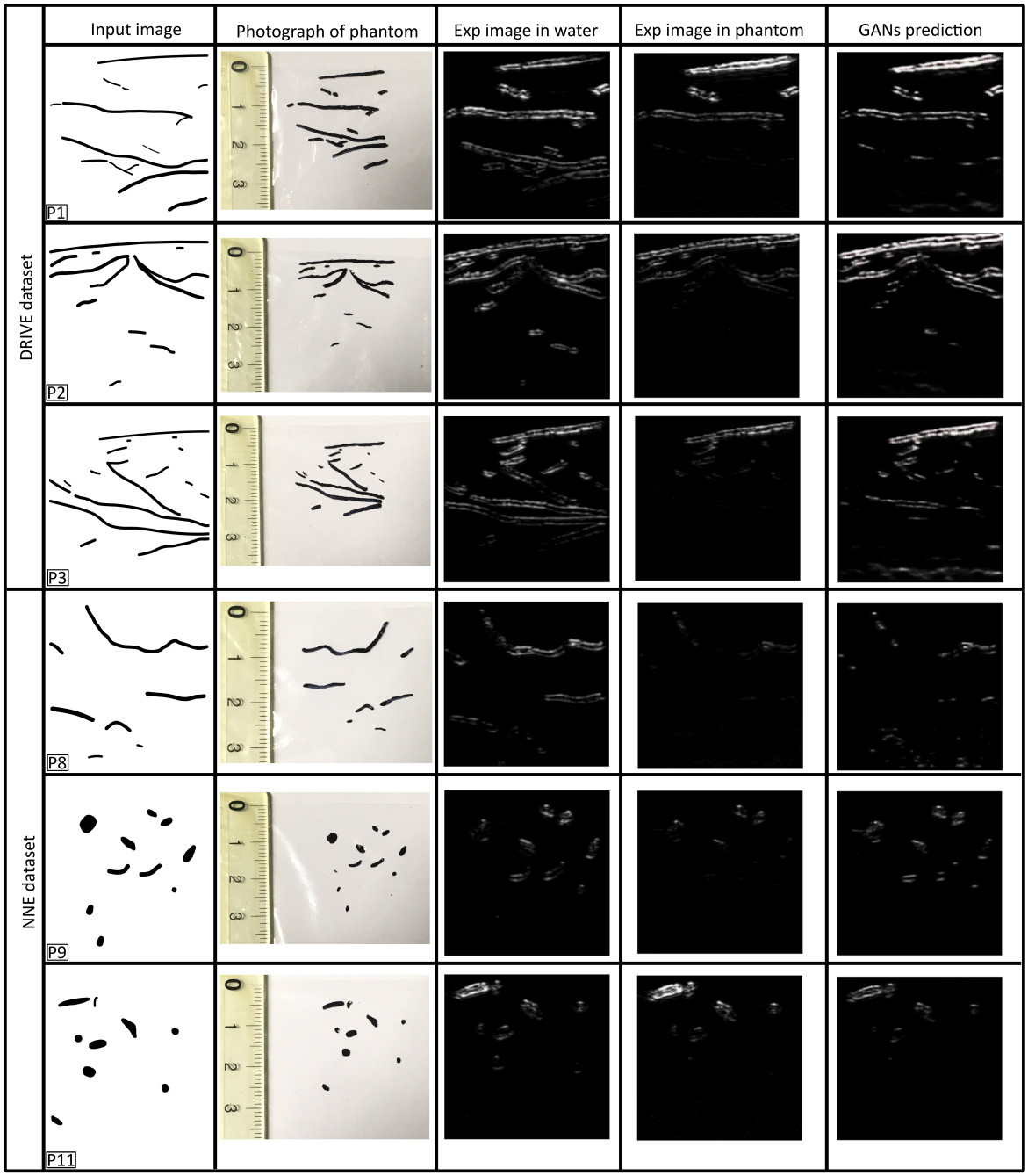

Figure 7.18: Phantom experiment, from right to left: Input images for the experiment, phantom of input images, experiment executed in water, experiment executed in tissue mimicking solution, prediction from phantom image.

than the SSIM values of the phantom images. Comparing the pSNR, the predicted images result in a lower pSNR than the phantom image, similar to the SSIM.

In the predicted images, in figure 7.18, there is more signal distinguishable from the predicted image than from the image in the phantom solution. Comparing the im-

Table 7.5: pSNR and SSIM for the Drive dataset, P1 P2 and P3 and for the NNE dataset: P8, P9 and P11. The results in water with a gain of 65 compared to the results in the phantom solution at a gain of 75, compared to the prediction results in the phantom solution.

	P1	P2	P3	P8	P9	P11
$SSIM(f_{water}, f_{phantom})$	0.78	0.88	0.82	0.90	0.95	0.95
$SSIM(f_{water}, f_{prediction})$	0.78	0.86	0.81	0.82	0.90	0.92
$pSNR(f_{water}, f_{phantom})$	19.8	23.3	24.7	28.0	35.2	32.4
$pSNR(f_{water}, f_{prediction})$	19.0	21.1	23.4	25.2	31.2	32.3

ages to the image in the water, the predicted image is closer to the water image than the image in the phantom is. This is not what you would expect from the pSNR and SSIM values. The difference between the metrics scores and the visual improvement can be explained by closely examining the images. In the predicted images, structures or noise can be observed at the bottom of the image, furthermore, the intensity of the signal from the predicted image does not correspond with the signal intensity in the image in the water. Nevertheless, structures are not distinguishable in the phantom image and are more apparent in the predicted image.

7.3 Conclusion

In this chapter, a GANs algorithm is used to investigate whether images from a LED-based PAI system could be enhanced to obtain more signals from the images. The algorithm is trained and tested with synthetically generated PA images, for different noise levels, and compared to a standard method of fluence compensation. The algorithm was able to distinguish more signals from the images, especially at higher noise levels of 20 and 10 dB, with respect to the fluence compensation.

The algorithm was tested on images obtained with the LED-based photoacoustic system for experimental validation. Here the metric scores are lower for the generated images than from the original images, however, when observing the images, the predicted image is matching closer to the image in water than the image in the phantom solution does. This indicates the potential and therefore it would be a good next step to train and test the images with real photoacoustics images instead of synthetic images, because the synthetic signal may differ significantly from the signal originating from the PAI system.

Chapter 8

Blood oxygen saturation imaging

The work in this chapter was published: Bulsink et al. [34]. In this chapter blood, oxygen saturation is estimated using the LED-based photoacoustic system as used in the previous chapters. Blood oxygen saturation measurements using a LED-based photoacoustic system can give spatial blood oxygen saturation values and might be an alternative for a golden standard oximeter. For an accurate estimation of the blood oxygen saturation levels inside the tissue, fluence compensation is used so the oxygen saturation levels at different depths can be determined accurately.

8.1 Introduction

Blood oxygen saturation(sO2) is the ratio between the amount of oxygen saturated hemoglobin to the total amount of hemoglobin in the blood. Reduced oxygen saturation can be an indicator of breathing problems, but also inflammation or tumor in tissue. The average oxygen saturation is often measured using a pulsoxymeter, but this gives only an average value and no spatial blood oxygen saturation values. Spatially resolved oxygen saturation can also be measured with functional MRI and PET, but these modalities are not always accessible and are expensive. A pulsoxymeter uses optical properties of oxygenated and deoxygenated hemoglobin in the near-infrared wavelengths to determine the oxygen saturation values. These properties can also be used spatially, using a photoacoustic system. Photoacoustic imaging combines the advantage of ultrasound and optical imaging techniques, reaching deeper in the tissue with using the optical properties at a relatively high resolution and can provide functional and molecular information.

8.2 Material

In this chapter, we used the LED-based PA imaging system: AcousticX (Cyberdyne Inc., Tsukuba, Japan). Two LED arrays with dual wavelengths, of 750 nm and 850 nm were used to distinguish oxygenated from deoxygenated hemoglobin. The LED arrays are placed on either side of the transducer (Figure 8.1e). The 850 nm array has pulse energy of 200 μJ and the 750 nm array has 100 μJ, with a pulse duration of 70 ns. The LED array has two rows of 36 elements 850 nm arrays and two rows of 24 elements 750 nm arrays arranged alternately. A 128 element, 7 MHz linear US transducer with a bandwidth of 80% was used in the probe.

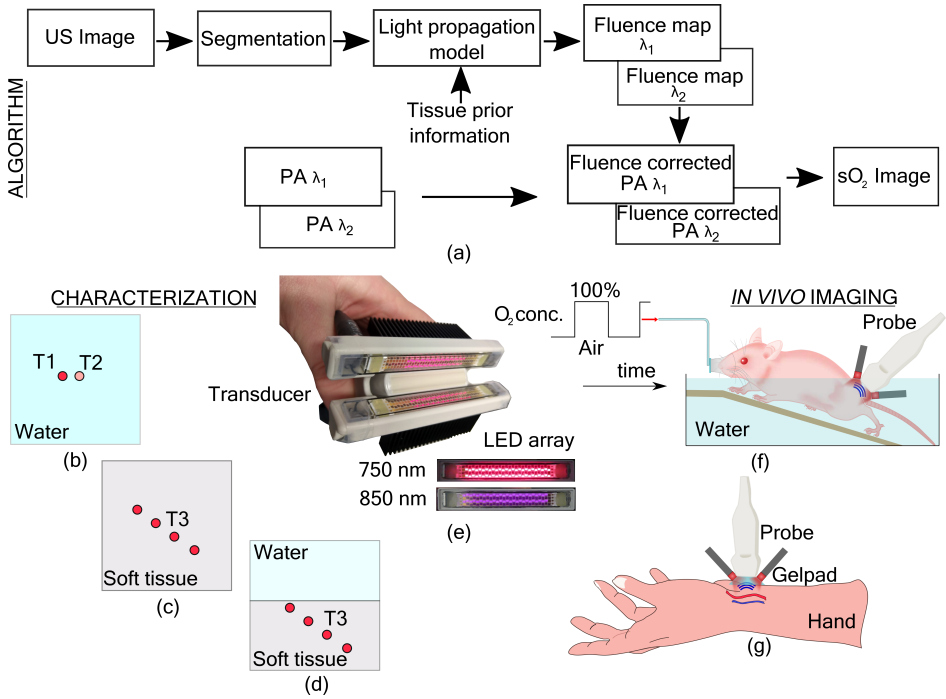

Figure 8.1: The workflow: (a) Algorithm for fluence compensation by using information from ultrasound. (b-d) experimental situation used. (e) The probe used, containing wavelengths of 750 and 850 nm. (f) Experiment of in vivo mouse imaging. (g) Imaging an artery on the wrist of a human volunteer.

Figure 8.1 shows the workflow used. A target is imaged, resulting in photoacoustic and ultrasound images. Information is taken from the Ultrasound image to segment structures. This image is smoothened with a median filter and with a manually selected threshold, to obtain tissue boundaries using the Sobel edge detector. After filling holes, the biggest part is detected as the target area.

The segmented Ultrasound information is used as input in a light propagation model. Using the light propagation model a fluence map of the target is created for

the different wavelengths used. These fluence maps are combined with the photoacoustic information to obtain a fluence compensated photoacoustic image, which is used to determine the oxygen saturation in the target.

8.2.1 Light propagation model

A model of the LED-based PAI setup is created using Monte Carlo-based simulations, similar to the simulations in the previous chapters. The Simulated LED arrays have the same dimensions as the LED arrays used in the experimental setup. The LED arrays have a width of 50 mm, with four rows of LED elements, two rows with 36 LED elements of 850 nm, and two rows with 24 LED elements of 750 nm. One LED array is placed on each side of the transducer, placed 95.6 mm apart, with an angle of 41.4 degrees with respect to the surface of the transducer.

The input for the Monte Carlo-based light propagation model (MCXLAB) [35] was the segmented binary mask, combined with the optical properties of the tissue in the experiments, which are determined beforehand. The positions of the LED elements in the array, the pulse energy, and the opening angle were defined for the light source in the simulations. The optical properties used, are measured in the phantom and obtained from the literature for the in vivo experiments and are shown in table 8.1.

Table 8.1: Optical properties used in the simulations.

Medium	wavelength $[nm]$	$\mu_a[cm^{-1}]$	$\mu_s'[cm^{-1}]$
Soft tissue phantom [48]	750	0.101	10.5
	850	0.089	9
Mice thigh muscle [49]	750	0.76	5.3
	850	0.64	4.8
Human forearm [50]	750	0.41	7.2
	850	0.3	6.5

With the simulations a geometry is created where the probe is placed in, this geometry is 55 mm (x-axis) × 55 mm (y-axis) ×37.9mm (z-axis) (744×744×512 pixels) with a grid size of 74 . The imaging plane is the center slice of this 3D grid, under the probe. The imaging plane during the simulations matches with the dimensions of the acquisition during the experiment, where the imaging plane is 40.32 mm (x) ×37.9 mm (z). The PA and US images were then interpolated to 545×512 pixel images with a uniform spacing of 74 μm in both dimensions, so the dimensions of both the images and the simulations are the same.

Transducer: 128 elements, pitch 0.315, 1024 time samples at 40 MHz sampling rate. LED array: angle of 41.4 degrees, length of 50 mm and a width of 10 mm,

distance of 9.56 mm between arrays, The elements were placed with a spacing of 1.4 mm within the arrays and the spacing between the arrays was 1.72 mm.

In the geometry of the simulations, the segmented ultrasound mask is used to mimic the target. The mask has dimensions of 545(x) x 512(z) pixels, however, the entire geometry has dimensions of 744(x) × 744(y) × 512(z) pixels. The Length of the simulation geometry (744 pixels) is bigger than the input mask(545 pixels) along the x-axis, so the LED array fits in the geometry, therefore the first and last pixels were replicated, so that the US mask is in the center. This 2D mask is replicated in the y-direction by stacking 744 copies of the mask.

8.2.2 Linear unmixing

For determining the blood oxygen saturation levels from the LED-based photoacoustic images, linear unmixing is used [51] [52].

Photoacoustic initial pressure originating from an absorber in which excitation by a pulsed light source is done, when stress confinement is assumed, is expressed as

$$p_0\left(r,\lambda_i\right) = \Gamma\mu_a\left(r,\lambda_i\right)\Phi(r,\lambda_i) \tag{8.1}$$

Where the grüneisen parameter Γ is the conversion efficiency from thermal energy to pressure, and μ_a is the optical absorption coefficient, Φ is the light fluence. The optical absorption coefficient can be written as the product of the concentration (c), and the molar extinction coefficient (ϵ) so the photoacoustic reconstructed photoacoustic image is:

$$p(r,\lambda_i) \;=\; \Phi(r,\lambda_i)[\epsilon_{HbR}\left(\lambda_i\right)c_{HbR}\left(r\right) \;+\epsilon_{HbO2}\left(\lambda_i\right)c_{HbO2}(r)] \tag{8.2}$$

The wavelengths used are $\lambda_1 = 750$ nm and $\lambda_2 = 850$ nm.The fluence compensated image can be discribed by:

$$b(r,\lambda_i) \;=\; p(r,\lambda_i)/\;\Phi(r,\lambda_i) \tag{8.3}$$

Here, for both the wavelengths fluence compensation photoacoustic images are used.

$$b = \begin{bmatrix} b(r,\lambda_1) \\ b(r,\lambda_2) \end{bmatrix} \tag{8.4}$$

Also, the molar extinction coefficient can be written in matrix form, for oxygenated and deoxygenated blood, for both wavelengths.

$$A = \begin{bmatrix} \epsilon_{HbR}(\lambda_1\ ) & \epsilon_{HbO2}\ (\lambda_1\ ) \\ \epsilon_{HbR}\ (\lambda_2\ ) & \epsilon_{HbO2}(\lambda_2\ ) \end{bmatrix} \tag{8.5}$$

With the molar concentration of oxygenated and deoxygenated blood:

$$x = \begin{bmatrix} c_{HbR}(r) \\ c_{HbO2}(r)] \end{bmatrix} \tag{8.6}$$

This concentration x can be found by using the linear equation: Ax=b. Solving this equation is given by the use of the least square solution.

$$x\ =\ (A^T\ A)^{-1}\ A^T\ b \tag{8.7}$$

This all leads to the following formula to obtain the molar concentration of the blood oxygen levels.

$$sO_2(r) =\ \frac{c_{HbO2}(r)}{c_{HbO2}(r) + c_{HbR}(r))} * 100\% \tag{8.8}$$

8.3 Method

Using a Fourier-based algorithm, the ultrasound and photoacoustic images are reconstructed [40]. The tissue boundaries are obtained from the information in the ultrasound image, by segmenting it. Using the segmented mask, and the optical properties of the tissue, a fluence map of the imaging plane of the two used wavelengths are obtained with the light propagation model. The photoacoustic images are normalized for the fluence, using the fluence maps. To obtain oxygen saturation images, linear unmixing is used on the fluence normalized photoacoustic images. This approach was done on three different sets of experiments:
- Validation of oxygen saturation imaging with the two-wavelength LED array, using the linear unmixing algorithm.
- Imaging tubes carrying blood at different depths, the effect of fluence compensation was investigated.
- The fluence compensation was tested on in vivo and phantom imaging.

8.3.1 In Vitro validation

The photoacoustic two-wavelength oxygen saturation imaging is compared against the ground truth method using an oximeter. In this experiment, two Polythene tubes (Smiths Medical, USA) with an inner diameter of 0.5 mm and an outer diameter of

0.84 mm, are placed in a tank filled with water, at 15 mm from the surface of the transducer. The tubes are placed beside each other, at the same depth with a small distance between them.

The two tubes were filled with blood, obtained by TechMed Centre donor services, University of Twente, from a human volunteer after completing an ethical approval, adhering to the Dutch Medical Research involving human subjects Act (WMO) [34]. The first tube contained blood with a constant oxygen saturation level of around 65%, while in the second tube different blood oxygen saturation levels are used. Deoxygenated blood is obtained by adding 17 mg of sodium hydrosulfite (Sigma Aldrich, Darmstadt, Germany) to 5 mL blood. And exposing it to atmospheric oxygen, so different levels of oxygen concentration are obtained. Before and after the measurements the blood oxygen saturation levels were measured using an oximeter (AVOXimeter 4000, ITC, Munich, Germany).

The tubes were imaged with the dual-wavelength LED-based photoacoustic imaging system at 750 and 850 nm by toggling between the wavelengths. Linear unmixing was applied to the photoacoustic images at a different wavelength to obtain the blood oxygen saturation levels. An area of 0.6 x 0.6 mm is used to estimate the mean blood oxygen saturation during analysis so these can be compared to the blood oxygen saturation levels measured by the oximeter.

8.3.2 Homogeneous phantom

Examining the effect of fluence on the blood oxygen saturation at different depths is done in the second experiment. Tubes containing blood were placed at four different depths in a tank filled with a medium with tissue-mimicking optical properties [48]. The optical properties are displayed in table 8.1. Fluence maps for both wavelengths are obtained using the light propagation model with a uniform mask, without any variations, with the optical properties of the medium. These fluence maps are used to compensate photoacoustic images for the illumination inequalities and the decay of intensity in LED-based photoacoustic imaging. From the fluence compensated photoacoustic images, the blood oxygen saturation levels are determined at different depths using linear unmixing and compared to the values of the oximeter.

8.3.3 Two slab phantom

In the third experiment, a tissue-mimicking situation is used, where there are two layers imaged. This is because, in the LED-based photoacoustic probe, the configuration of the probe with the LED arrays on the side of the transducer prevents the transducer from touching the tissue, so a coupling medium will be used. The

two slabs used are water for the top layer and a tissue-mimicking phantom as used in the previous experiment as the second layer. The layers are separated using polyurethane US film (Protection Cover Ultrasound B. V., The Netherlands) with a thickness of 140 μm [34]. Four tubes at different depths, which filled with blood are used, the same as in the previous experiment. The blood oxygen levels in the tubes were determined using the oximeter and kept constant and are expected to be the same in all tubes.

Using the light propagation model with a mask of the two-layer phantom, the fluence maps of the phantom are determined for both wavelengths. These fluence maps were used to compensate the images for the fluence and the blood oxygen saturation levels were determined using linear unmixing.

8.3.4 In Vivo imaging

After the experiments in the phantom solution, two in vivo experiments are performed. In the first in vivo experiment, a mouse is imaged to estimate the blood oxygen saturation. An animal (BALB/c nude mice) was anesthetized. The lower body of the mice is placed in a bath of warm water, so the water is serving as a coupling medium for the transducer. The flank region close to the thigh is used to image and is aligned with the probe. At first, the animal breathed normal air, and the blood oxygen saturation imaging was done. After these measurements, the air that the animal breathes is changed to 100% oxygen after the oxygen levels are stabilized, and new measurements are performed. From this information, the tissue boundaries are determined to create a mask, with which a fluence map is created of the tissue using the light propagation model. With these results, fluence compensated images are obtained and used to determine the blood oxygen saturation levels.

8.3.5 Human imaging

After the animal imaging, an experiment on a human wrist of a healthy volunteer with brown skin was done. The wrist was imaged in a tank of water, which functions as a coupling medium. An artery and a vein are identified and imaged in real-time. Similar to the previous experiments a mask was obtained and used to determine the fluence map with the light propagation model. The fluence normalized images of both wavelengths are used to determine the blood oxygen saturation levels by linear unmixing. The blood oxygen saturation levels are estimated for the artery and the vein.

8.4 Results

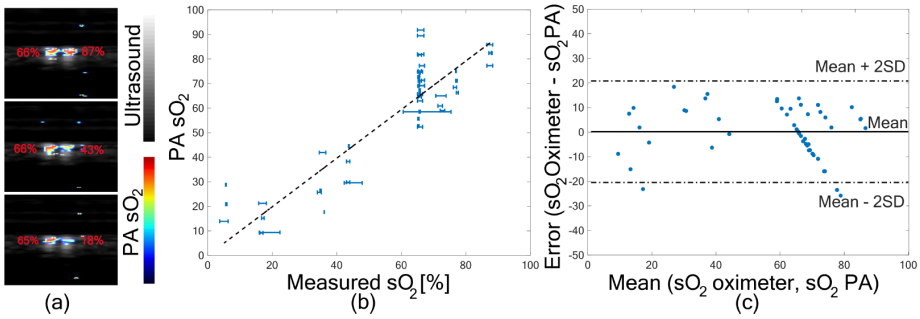

Figure 8.2: Validation of photoacoustic Oxygen saturation. (a) oxygen saturation images of 3 blood oxygen levels, with measurement of the oximeter shown in the image. (b) Oxygen saturation against the oximeter readings. (c) Error plot of the average of photoacoustic oxygen saturation and the oximeter values against the difference between the methods. [34]

8.4.1 In Vitro validation

In the first experiment, the photoacoustic blood oxygen saturation method was tested against the golden standard oximeter measurements of the blood oxygen saturation levels. Two tubes, filled with blood are shown in figure 8.2a the tube on the left has a constant blood oxygen saturation level and the level of blood oxygen saturation in the right tube is altered. The values of the blood oxygen saturation levels, measured using an oximeter, are shown next to the tubes.

For the estimation of the blood oxygen saturation levels in the tubes, a region of interest of 0.6 x 0.6 mm is taken and the mean values are calculated for these regions. In figure 8.2b the mean blood oxygen saturation levels are shown, which are measured in the tubes, against the blood oxygen saturation levels measured with the oximeter. There is a linear correlation between the measurements with the oximeter and the measurements with the photoacoustic setup, with a correlation coefficient of 0.893. In figure 8.2c, the error of the determined blood oxygen saturation levels with the photoacoustic system is shown, against the difference between the measurements using the oximeter and the photoacoustic system. This shows a mean error of 0.18% and a standard deviation of 10.33%. The noise is probably the cause of the variations.

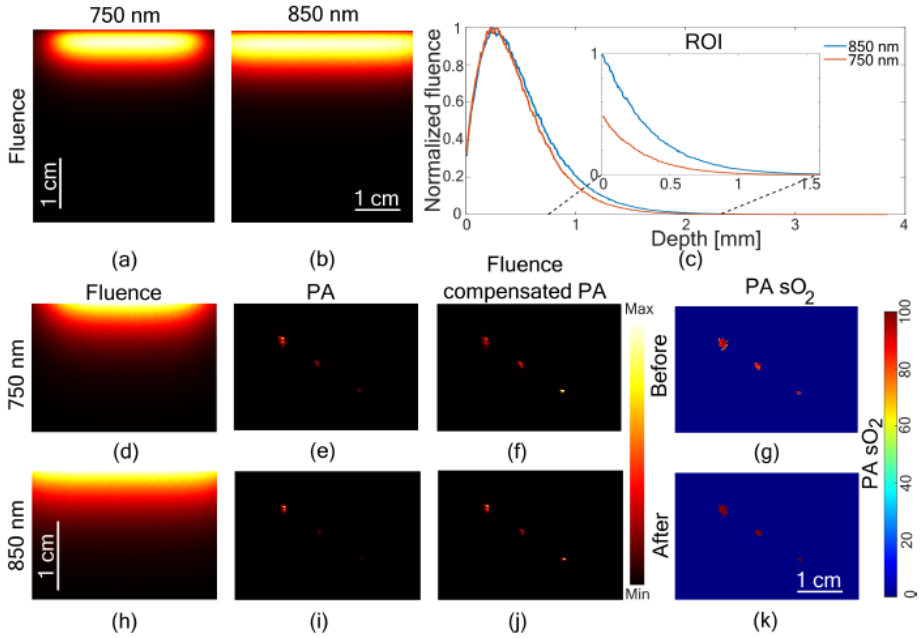

Figure 8.3: Oxygen saturation measurement for a homogeneous phantom: (a-b) The fluence maps for 750 and 850 nm. (c) the fluence profile of the normalized fluence (d,h) Region of interest of the fluence map. (e,i) Photoacoustic signal. (f,j) Fluence compensated photoacoustic signal. (g,k) Oxygen saturation image (g) before fluence compensation and (k) after fluence compensation.

8.4.2 Homogeneous phantom

In the second experiment, the blood oxygen saturation is investigated at different depths. Here tubes at different depths are placed in a tank filled with a tissue-mimicking medium. Photoacoustic images are obtained and the ultrasound images are used to create a fluence map for 750 and 850 nm as shown in figure 8.3a and b. A normalized line profile of the fluence maps is obtained and shown in figure 8.3c. The region of interest is smaller than the entire profile, due to the placement of the LED arrays in the geometry. In figure 8.3e,i the photoacoustic images without fluence compensation are displayed. Figure 8.3f,j shows the photoacoustic images, which compensated for the fluence using the fluence maps, so the fluence compensated oxygen saturation levels can be determined. Using the photoacoustic images, a blood oxygen saturation was determined as shown in figure 8.3g,k, this was done for the normal and fluence compensated photoacoustic images.

In the normal, not fluence compensated image, the oxygen saturation levels are determined for the tubes. The first tube shows an oxygen saturation level of 85.8%, the second tube of 83.9%, and the third tube of 81.7%. When fluence compensation

is applied on the images the blood oxygen saturation levels are 99.1% in the first tube, 99.3% in the second tube, and 99.6% in the third tube. The values measured using the oximeter were 95.9% before the experiment and 96.6% after the experiment. The fourth tube was not visible in the reconstructed images, while it was visible on the system.

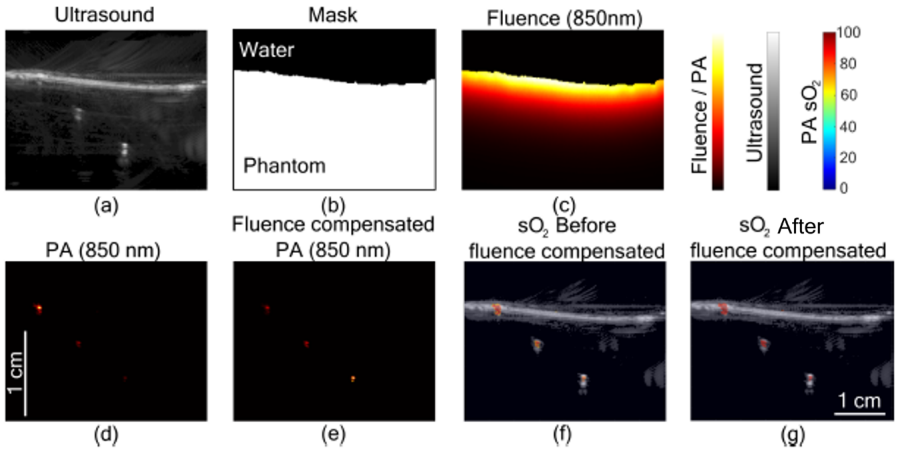

Figure 8.4: Oxygen saturation measurement for a two slab phantom. (a) Ultrasound image (b) binary mask (c) fluence map (850 nm) (d) photoacoustic image (e) fluence compensated photoacoustic image (f) photoacoustic oxygen saturation before fluence compensation (g) photoacoustic oxygen saturation after fluence compensation.

8.4.3 Two slab phantom

In the third experiment, a setup with two layers is used, where the first layer is a layer of water and the second layer a tissue-mimicking layer. The same phantom with the tubes as in the previous experiment was used. In figure 8.4 the phantom can be seen. The ultrasound image is segmented, and the two-layer mask is used as input in the light propagation model to obtain a fluence mask for 750 and 850 nm. With this, the blood oxygen saturation was determined, with and without the fluence compensation. The mean blood oxygen saturation without fluence compensation for the first tube was 82.4%, for the second tube, this was 76.9%, and in the third tube 77.7%. With fluence compensation, the blood oxygen saturation determined in the tubes was 91.8% in the first tube, 89.5% in the second tube, and 92.1% in the third tube. The values measured using the oximeter were 96.8% before the experiment and 97.4% after the experiment.

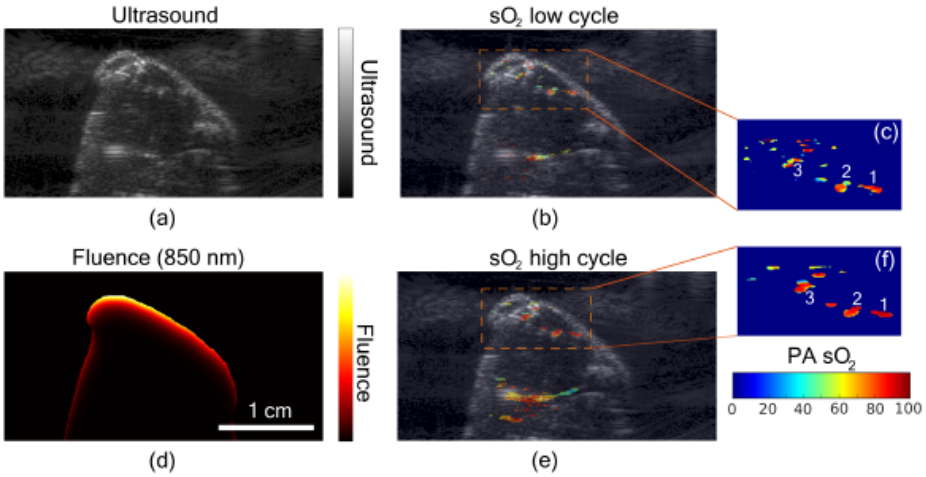

Figure 8.5: Oxygen saturation measurement on mice thigh muscle. (a) ultrasound image (b) fluence compensated oxygen saturation image durng a low oxygen cycle (c) zoomed in section of b (d) fluence mat at 850 nm (e) fluence compensated oxygen saturation image durng a high oxygen cycle (f) zoomed in section of e.

8.4.4 In Vivo imaging

In the fourth experiment, a mouse is used to examine the oxygen saturation imaging using the photoacoustic system. The thigh of the mouse is imaged, where the oxygen the mouse breathes is altered. In figure 8.5a the ultrasound image of the thigh muscle of the mouse is displayed. This ultrasound image is segmented, and the mask is used to obtain a fluence mask for both wavelengths, figure 8.5d shows the fluence map of 850 nm. This is used to do the fluence compensation of the photoacoustic mouse thigh muscle image as can be seen in figure 8.5b and e where the air that is breathed by the mouse is altered from normal air to 100% oxygen, and on the right the zoomed-in sections of the thigh in figure 8.5f and g can be observed. The blood oxygen saturation levels were determined from these zoomed-in images for three regions. In the low cycle, these regions had a mean blood oxygen saturation value of 72.9% in region 1, 67.8% in region 2, and 67.3% in region 3. When the mouse is breathing high oxygen, the blood oxygen saturation level of the first region is 93.4%, of the second region this is 89.2% and the third region has an oxygen saturation of 85.4%

8.4.5 Human imaging

In the last experiment, the wrist of a healthy human volunteer was used to measure with the photoacoustic system. In figure 8.6, an artery and a vein are used for the

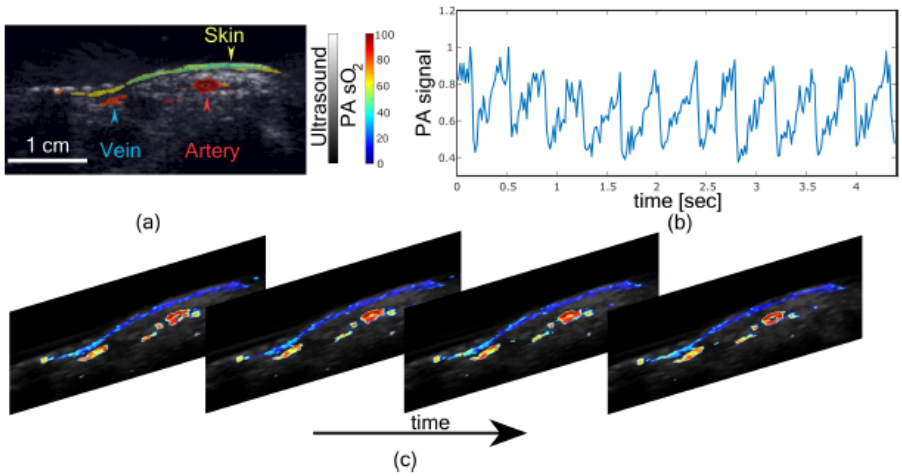

Figure 8.6: Fluence compensated oxygen saturation measurement in the human wrist. (a) Fluence compensated oxygen saturation image overlayed on an ultrasound image (b) normalized photoacoustic signal from the artery (c) frames of the pulsating artery.

measurement of the blood oxygen saturation. From this, a blood oxygen level of 92.6% was found for the artery, and an oxygen saturation level of 78.7% for the vein, this is clearly visible in figure 8.6a. the real-time signal is obtained at a wavelength of 850nm, as can be seen in figure 8.6b, the heartbeat is obtained from the signal origination from the artery as shown in figure 8.6c, a heartbeat of 84 bpm is estimated from this.

8.5 Conclusion

The results in this chapter show that blood oxygen saturation imaging using a dual-wavelength LED-based photoacoustic system has potential for use in clinical and preclinical applications. The method has a limited imaging depth in soft tissue, which would be beneficial to improve. Using fluence compensation in this method improves the accuracy of the blood oxygen saturation levels by 12-15%.

Chapter 9

Conclusions and recommendations

The main objective of this thesis was to enhance the imaging depth for a handheld LED-based photoacoustic imaging system. To achieve this, different routes have been taken. In changing the illumination of the LED-based photoacoustic system, the imaging depth could be increased. The experimental results of chapter 5 show that by increasing the number of LED arrays from 2 to 4, the imaging depth was increased from 24 mm to 29 mm respectively. The optimal configuration has been investigated and was found to be a configuration with a straight LED row configuration with 10 rows of LED elements, at an angle of 60 degrees with respect to the transducer.

For further research, a new probe for enhancing the imaging depth can be developed. In developing the new probe, the physiology of the patient has to be taken into account. Factors that might be limiting in the design of the probe might be the shape of the body. Ideally, the transducer has contact with the skin, without a coupling medium. The final probe has to be designed with this in mind. In this research, the shape of the illumination is limited to LED arrays, with multiple rows of LED chips. However, other configurations than an array are also possible. An example is an ultrasound transducer, surrounded by LED elements on all sides. It would be interesting to investigate what the effect of this would be on the light delivery in the tissue.

In the other route that is taken, a GANs algorithm is trained to obtain signals from deeper depths from noisy images which are highly influenced by the decay of fluence. This synthetic data is generated from two different datasets, the Drive dataset, containing 240 retina vessel images, and the NNE dataset containing 9531 images from vessels in a mouse brain. The images are converted to photoacoustic images, with and without the influence of fluence and at 5 different noise levels, and used to train an algorithm for different noise levels. The algorithm was able to distinguish more signals from the images, especially at higher noise levels of 20

and 10 dB, with respect to the fluence compensation. The algorithm was tested on images obtained with the LED-based photoacoustic system for validation. Here the metric scores are lower for the generated images than from the original images, however, when observing the images, an enhancement of signal from the upper half of the image can be observed, while in the lower half mainly noise is being enhanced.

The enhancement of signal in the experimental PA images shows potential and therefore it would be a good next step to train and test the images with real photoacoustic images of vessels, instead of synthetic images. The signal and noise that are generated from the images may differ significantly and therefore not result in improved imaging when the algorithm is used on images obtained with the photoacoustic system. A way to generate a ground truth and test dataset can be by using phantoms, where in-water images of phantoms are obtained which can be used as ground truth, and images in a tissue-mimicking phantom at different averaging levels can be used as a train set.

Furthermore, an algorithm should be robust for every noise level, and not a specific noise level as it is now, therefore it would be wise to train an algorithm on a variety of noise levels or multiple training sessions for the different levels of averaging in the system.

In this research, the possibility to enhance the signal from a noisy, image with a high influence on the fluence decay is investigated. The usability and reliability need to be investigated further. The system is prone to miss data or add data to the predictions, which reduces the reliability. For the use of photoacoustic images with enhancement in medical healthcare, the signal observed has to be trustworthy and an incorrect result can have a big impact on the treatment of a patient.

Additionally, we concluded that blood oxygen saturation imaging using a dual-wavelength LED-based photoacoustic system has potential for use in clinical and preclinical applications. The method has a limited imaging depth in soft tissue, which would be beneficial to improve. This shows the importance of the work in this paper for the enhancement of the imaging depth for LED-based photoacoustic imaging.

Bibliography

[1] S. Manohar and D. Razansky, "Photoacoustics: a historical review," *Adv. Opt. Photon.*, vol. 8, no. 4, pp. 586–617, Dec 2016.

[2] S. Singh, S. Paul, and A. Thomas, *Fundamentals of Photoacoustic Imaging: A Theoretical Tutorial*, 04 2020, pp. 3–21.

[3] Y. Zhu, T. Feng, Q. Cheng, X. Wang, S. Du, N. Sato, J. Yuan, and M. Kuniyil Ajith Singh, "Towards clinical translation of led-based photoacoustic imaging: A review," *Sensors*, vol. 20, no. 9, 2020.

[4] M. S. Singh, S. Paul, and A. Thomas, "Fundamentals of photoacoustic imaging: A theoretical tutorial," 2020.

[5] S. Srinivasan, B. W. Pogue, S. Jiang, H. Dehghani, C. Kogel, S. Soho, J. J. Gibson, T. D. Tosteson, S. P. Poplack, and K. D. Paulsen, "Interpreting hemoglobin and water concentration, oxygen saturation, and scattering measured in vivo by near-infrared breast tomography," vol. 100, no. 21, pp. 12 349–12 354, 2003.

[6] "Sources of absorption and scattering contrast for near-infrared optical mammography," *Academic Radiology*, vol. 8, no. 3, pp. 211–218, 2001.

[7] E. Z. Zhang, B. Povazay, J. Laufer, A. Alex, B. Hofer, B. Pedley, C. Glittenberg, B. Treeby, B. Cox, P. Beard, and et al., "Multimodal photoacoustic and optical coherence tomography scanner using an all optical detection scheme for 3d morphological skin imaging," Aug 2011.

[8] C. P. Favazza, L. V. Wang, O. W. Jassim, and L. A. Cornelius, "In vivo photoacoustic microscopy of human cutaneous microvasculature and a nevus," *Journal of Biomedical Optics*, vol. 16, no. 1, pp. 1 – 6, 2011. [Online]. Available: https://doi.org/10.1117/1.3528661

[9] Y. Zhu, G. Xu, J. Yuan, J. Jo, G. Gandikota, H. Demirci, T. Agano, N. Sato, Y. Shigeta, and X. Wang, "Light emitting diodes based photoacoustic imaging and potential clinical applications," *Scientific Reports*, vol. 8, 2018.

[10] Y. Zhu, X. Lu, X. Dong, J. Yuan, M. Fabiilli, and X. Wang, “Led-based photoacoustic imaging for monitoring angiogenesis in fibrin scaffolds,” *Tissue Engineering Part C: Methods*, vol. 25, 08 2019.

[11] T. N. Erpelding, C. Kim, M. Pramanik, L. Jankovic, K. Maslov, Z. Guo, J. A. Margenthaler, M. D. Pashley, and L. V. Wang, “Sentinel lymph nodes in the rat: Noninvasive photoacoustic and us imaging with a clinical us system,” *Radiology*, vol. 256, no. 1, pp. 102–110, 2010, pMID: 20574088.

[12] C. Kim, E. C. Cho, J. Chen, K. H. Song, L. Au, C. Favazza, Q. Zhang, C. M. Cobley, F. Gao, Y. Xia, and L. V. Wang, “In vivo molecular photoacoustic tomography of melanomas targeted by bioconjugated gold nanocages,” *ACS Nano*, vol. 4, no. 8, pp. 4559–4564, 2010, pMID: 20731439.

[13] S. L. Jacques, “Role of tissue optics and pulse duration on tissue effects during high-power laser irradiation,” *Appl. Opt.*, vol. 32, no. 13, pp. 2447–2454, May 1993. [Online]. Available: http://opg.optica.org/ao/abstract.cfm?URI=ao-32-13-2447

[14] J. Laufer, *Photoacoustic Imaging: Principles and Applications*. Cham: Springer International Publishing, 2018, pp. 303–324. [Online]. Available: https://doi.org/10.1007/978-3-319-65924-4_13

[15] P. Beard, “Biomedical photoacoustic imaging,” *Interface Focus*, vol. 1, no. 4, pp. 602–631, 2011.

[16] S. Schüpbach, A. Gertsch, M. Kitz, and M. Frenz, “Fourier reconstruction in optoacoustic imaging using truncated regularized inverse k-space interpolation,” *Inverse Problems*, vol. 23, p. S51, 11 2007.

[17] A. Hariri, J. Lemaster, J. Wang, A. S. Jeevarathinam, D. L. Chao, and J. V. Jokerst, “The characterization of an economic and portable led-based photoacoustic imaging system to facilitate molecular imaging,” *Photoacoustics*, vol. 9, pp. 10 – 20, 2018. [Online]. Available: http://www.sciencedirect.com/science/article/pii/S2213597917300204

[18] T. Allen, *High-Power Light Emitting Diodes; An Alternative Excitation Source for Photoacoustic Tomography*, 04 2020, pp. 23–43.

[19] E. S. Donkor, “Stroke in the21stcentury: A snapshot of the burden, epidemiology, and quality of life,” *Stroke Research and Treatment*, vol. 2018, pp. 1–10, Nov. 2018. [Online]. Available: https://doi.org/10.1155/2018/3238165

[20] M. Flaherty, B. Kissela, J. Khoury, K. Alwell, C. Moomaw, D. Woo, P. Khatri, S. Ferioli, O. Adeoye, and D. Kleindorfer, "Carotid artery stenosis as a cause of stroke," *Neuroepidemiology*, vol. 40, pp. 36–41, 10 2012.

[21] L. National Heart and B. Institute, "Carotid artery disease."

[22] M. M. Mughal, M. K. Khan, J. K. DeMarco, A. Majid, F. Shamoun, and G. S. Abela, "Symptomatic and asymptomatic carotid artery plaque," *Expert Review of Cardiovascular Therapy*, vol. 9, no. 10, pp. 1315–1330, 2011.

[23] R. Naylor, "Time to rethink management strategies in asymptomatic carotid artery disease," *Nature reviews. Cardiology*, vol. 9, pp. 116–24, 02 2012.

[24] C. C. Lambert, F. S. Gayzik, and J. D. Stitzel, "Characterization of the carotid and adjacent anatomy using non-contrast ct for biomechanical model development," *Biomed Sci Instrum.*, vol. 43, pp. 330–335, 2007. [Online]. Available: https://pubmed.ncbi.nlm.nih.gov/17487103/

[25] H. Sung, J. Ferlay, R. L. Siegel, M. Laversanne, I. Soerjomataram, A. Jemal, and F. Bray, "Global cancer statistics 2020: Globocan estimates of incidence and mortality worldwide for 36 cancers in 185 countries," *CA: A Cancer Journal for Clinicians*, vol. 71, no. 3, pp. 209–249, 2021.

[26] I. of Medicine and N. R. Council, *Mammography and Beyond: Developing Technologies for the Early Detection of Breast Cancer*, S. J. Nass, I. C. Henderson, and J. C. Lashof, Eds. Washington, DC: The National Academies Press, 2001.

[27] F. Pediconi, C. Catalano, A. Roselli, V. Dominelli, S. Cagioli, A. Karatasiou, A. Pronio, M. Kirchin, and R. Passariello, "The challenge of imaging dense breast parenchyma: is magnetic resonance mammography the technique of choice? a comparative study with x-ray mammography and whole-breast ultrasound," *Invest Radiol.*, vol. 44, no. 7, pp. 412–421, 2009.

[28] R. Hooley, L. Andrejeva, and L. Scoutt, "Breast cancer screening and problem solving using mammography, ultrasound, and magnetic resonance imaging," *Ultrasound quarterly*, vol. 27, pp. 23–47, 03 2011.

[29] J. Edney, J. Onesti, K. Bland, B. Pockaj, A. Chagpar, E. Nelson, and J. Moore, "Breast cancer tumor size: correlation between magnetic resonance imaging and pathology measurements discussion," *The American Journal of Surgery*, vol. 196, pp. 849–850, 12 2008.

[30] M. K. A. Singh, M. Dantuma, F. K. Joseph, S. Manohar, and W. Steenbergen, "Breast imaging using an LED-based photoacoustic and ultrasound imaging

system: a proof-of-concept study," in *Photons Plus Ultrasound: Imaging and Sensing 2021*, A. A. Oraevsky and L. V. Wang, Eds., vol. 11642, International Society for Optics and Photonics. SPIE, 2021, pp. 32 – 38. [Online]. Available: https://doi.org/10.1117/12.2578590

[31] D. Hanahan and R. Weinberg, "Hallmarks of cancer: The next generation," *Cell*, vol. 144, pp. 646–74, 03 2011.

[32] M. Xu and L. V. Wang, "Photoacoustic imaging in biomedicine," *Review of Scientific Instruments*, vol. 77, no. 4, p. 041101, 2006.

[33] S. Manohar and M. Dantuma, "Current and future trends in photoacoustic breast imaging," *Photoacoustics*, vol. 16, p. 100134, 2019. [Online]. Available: https://www.sciencedirect.com/science/article/pii/S2213597918300442

[34] R. Bulsink, M. Kuniyil Ajith Singh, M. Xavierselvan, S. Mallidi, W. Steenbergen, and K. J. Francis, "Oxygen saturation imaging using led-based photoacoustic system," *Sensors*, vol. 21, no. 1, 2021. [Online]. Available: https://www.mdpi.com/1424-8220/21/1/283

[35] S. Yan and Q. Fang, "Hybrid mesh and voxel based monte carlo algorithm for accurate and efficient photon transport modeling in complex bio-tissues," *Biomed. Opt. Express*, vol. 11, no. 11, pp. 6262–6270, Nov 2020. [Online]. Available: http://opg.optica.org/boe/abstract.cfm?URI=boe-11-11-6262

[36] Q. Fang and D. A. Boas, "Monte carlo simulation of photon migration in 3d turbid media accelerated by graphics processing units," *Opt. Express*, vol. 17, no. 22, pp. 20 178–20 190, Oct 2009. [Online]. Available: http://opg.optica.org/oe/abstract.cfm?URI=oe-17-22-20178

[37] T. Agano, N. Sato, and K. Awazu, "LED-based photoacoustic imaging system: why it achieves the same signal to noise ratio as solid-state-laser-based system: a review," in *Photons Plus Ultrasound: Imaging and Sensing 2020*, A. A. Oraevsky and L. V. Wang, Eds., vol. 11240, International Society for Optics and Photonics. SPIE, 2020, pp. 80 – 93. [Online]. Available: https://doi.org/10.1117/12.2544486

[38] P. Isola, J.-Y. Zhu, T. Zhou, and A. A. Efros, "Image-to-image translation with conditional adversarial networks," *CVPR*, 2017.

[39] F. K. Joseph, A. Arora, P. Kancharla, M. K. A. Singh, W. Steenbergen, and S. S. Channappayya, "Generative adversarial network-based photoacoustic image reconstruction from bandlimited and limited-view data," in *Photons Plus*

Ultrasound: Imaging and Sensing 2021, A. A. Oraevsky and L. V. Wang, Eds., vol. 11642, International Society for Optics and Photonics. SPIE, 2021, pp. 208 – 213. [Online]. Available: https://doi.org/10.1117/12.2577750

[40] J. Staal, M. Abramoff, M. Niemeijer, M. Viergever, and B. van Ginneken, "Ridge-based vessel segmentation in color images of the retina," *IEEE Transactions on Medical Imaging*, vol. 23, no. 4, pp. 501–509, 2004.

[41] H. Uhlirova, P. Tian, K. Kılıç, M. Thunemann, V. B. Sridhar, H. Bartsch, A. M. Dale, A. Devor, and P. A. Saisan, "Neurovascular network explorer 2.0: A database of 2-photon single-vessel diameter measurements from mouse si cortex in response to optogenetic stimulation," *Frontiers in Neuroinformatics*, vol. 11, 2017. [Online]. Available: https://www.frontiersin.org/article/10.3389/fninf.2017.00004

[42] J. Krejza, M. Arkuszewski, S. E. Kasner, J. Weigele, A. Ustymowicz, R. W. Hurst, B. L. Cucchiara, and S. R. Messe, "Carotid artery diameter in men and women and the relation to body and neck size," *Stroke*, vol. 37, no. 4, pp. 1103–1105, 2006.

[43] B. Müller, S. Lang, M. Dominietto, M. Rudin, G. Schulz, H. Deyhle, M. Germann, F. Pfeiffer, C. David, and T. Weitkamp, "High-resolution tomographic imaging of microvessels," *Proc SPIE*, vol. 7078, p. 70780B, 08 2008.

[44] B. E. Treeby and B. T. Cox, "k-Wave: MATLAB toolbox for the simulation and reconstruction of photoacoustic wave fields," *Journal of Biomedical Optics*, vol. 15, no. 2, pp. 1 – 12, 2010. [Online]. Available: https://doi.org/10.1117/1.3360308

[45] F. K. Joseph, A. Arora, P. Kancharla, M. K. A. Singh, W. Steenbergen, and S. S. Channappayya, "Generative adversarial network-based photoacoustic image reconstruction from bandlimited and limited-view data," in *Photons Plus Ultrasound: Imaging and Sensing 2021*, A. A. Oraevsky and L. V. Wang, Eds., vol. 11642, International Society for Optics and Photonics. SPIE, 2021, pp. 208 – 213. [Online]. Available: https://doi.org/10.1117/12.2577750

[46] ——, "Generative adversarial network-based photoacoustic image reconstruction from bandlimited and limited-view data," in *Photons Plus Ultrasound: Imaging and Sensing 2021*, A. A. Oraevsky and L. V. Wang, Eds., vol. 11642, International Society for Optics and Photonics. SPIE, 2021, pp. 208 – 213. [Online]. Available: https://doi.org/10.1117/12.2577750

[47] B. E. Treeby, T. K. Varslot, E. Z. Zhang, J. G. Laufer, and P. C. Beard, "Automatic sound speed selection in photoacoustic image reconstruction using an autofocus approach," *Journal of Biomedical Optics*, vol. 16, no. 9, pp. 1 – 4, 2011. [Online]. Available: https://doi.org/10.1117/1.3619139

[48] S. L. Jacques, "Optical properties of biological tissues: a review," *Physics in Medicine and Biology*, vol. 58, no. 11, pp. R37–R61, may 2013. [Online]. Available: https://doi.org/10.1088/0031-9155/58/11/r37

[49] A. Krainov, A. Mokeeva, E. Sergeeva, P. Agrba, and M. Kirillin, "Optical properties of mouse biotissues and their optical phantoms," *Optics and Spectroscopy*, vol. 115, pp. 193–200, 08 2013.

[50] A. N. BASHKATOV, E. A. GENINA, and V. V. TUCHIN, "Optical properties of skin, subcutaneous, and muscle tissues: A review," *Journal of Innovative Optical Health Sciences*, vol. 04, no. 01, pp. 9–38, 2011. [Online]. Available: https://doi.org/10.1142/S1793545811001319

[51] B. T. Cox, J. G. Laufer, P. C. Beard, and S. R. Arridge, "Quantitative spectroscopic photoacoustic imaging: a review," *Journal of Biomedical Optics*, vol. 17, no. 6, pp. 1 – 23, 2012. [Online]. Available: https://doi.org/10.1117/1.JBO.17.6.061202

[52] M.-L. Li, J.-T. Oh, X. Xie, G. Ku, W. Wang, C. Li, G. Lungu, G. Stoica, and L. V. Wang, "Simultaneous molecular and hypoxia imaging of brain tumors ¡emphasis emphasistype="italic"¿in vivo¡/emphasis¿ using spectroscopic photoacoustic tomography," *Proceedings of the IEEE*, vol. 96, no. 3, pp. 481–489, 2008.

[53] N. Bosschaart, G. Edelman, M. Aalders, T. van Leeuwen, and D. Faber, "A literature review and novel theoretical approach on the optical properties of whole blood," *Lasers Medical Science*, vol. 29, no. 2, pp. 453–79, 2014.

[54] A. N. BASHKATOV, E. A. GENINA, and V. V. TUCHIN, "Optical properties of skin, subcutaneous, and muscle tissues: A review," *Journal of Innovative Optical Health Sciences*, vol. 04, no. 01, pp. 9–38, 2011. [Online]. Available: https://doi.org/10.1142/S1793545811001319

[55] R. Michels, F. Foschum, and A. Kienle, "Optical properties of fat emulsions," *Optics express*, vol. 16, pp. 5907–25, 05 2008.

Appendix A

Angle approximation

The rough geometric optics approximation so that the distance between the LED arrays and placement of the arrays with respect to each other were also taken into account. These images are on scale.

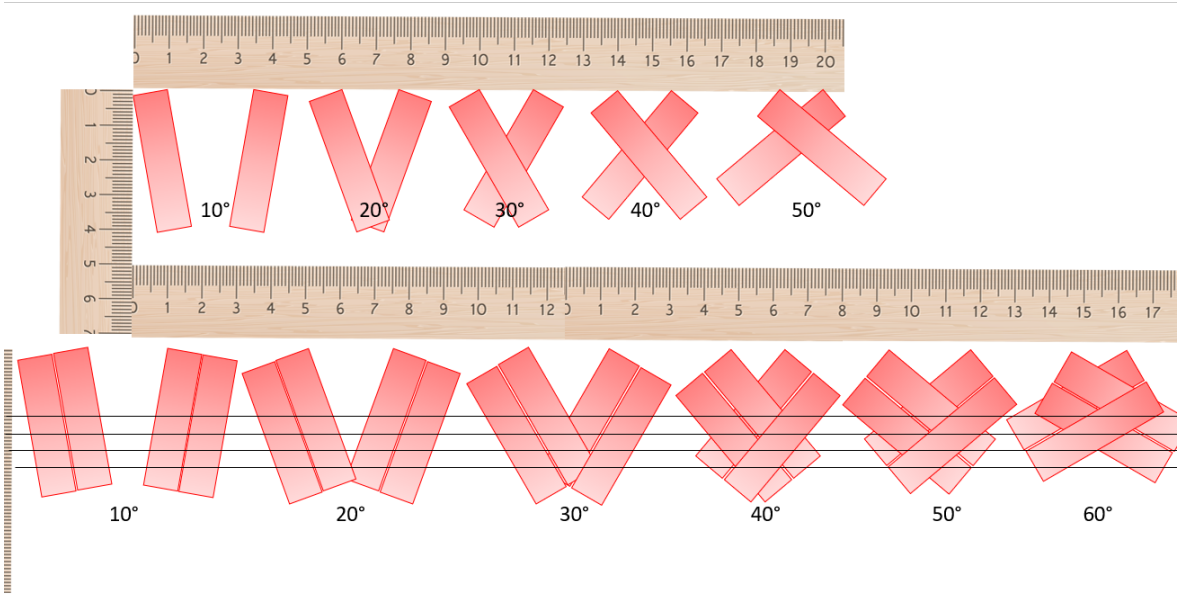

Figure A.1: Rough geometric optics approximation for parallel angles for the LED arrays on either side.

Combination table of all angles and number of threads visible by eye.

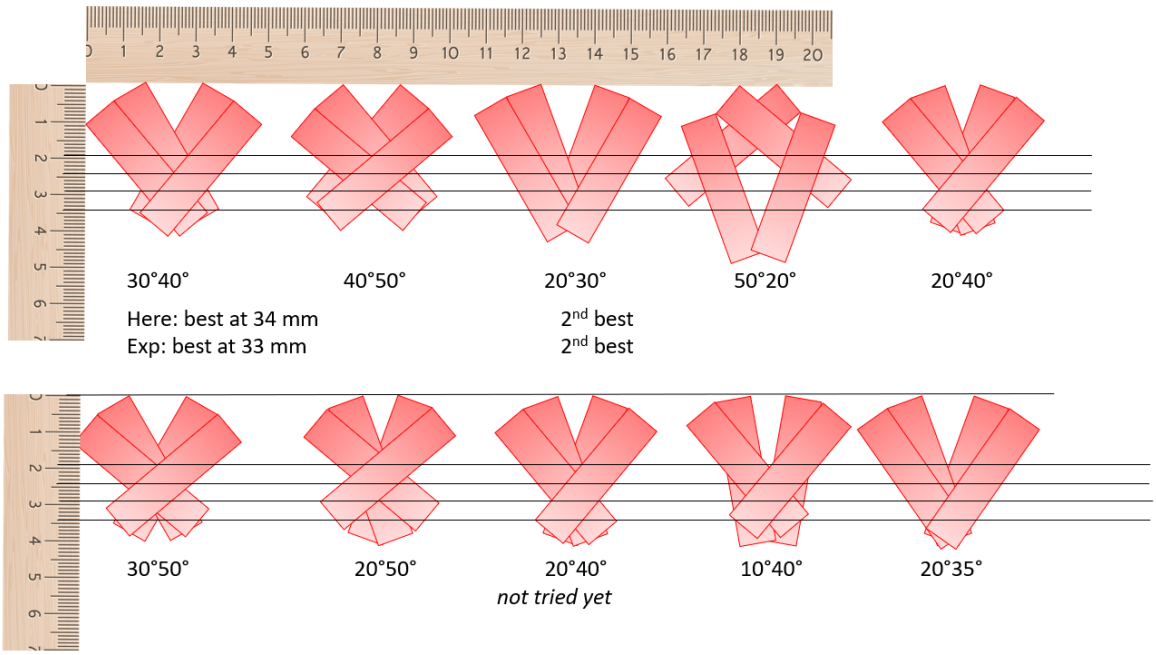

Figure A.2: Rough geometric optics approximation for non-parallel angles for the LED arrays on either side.

Appendix B

Developed probe design

To be able to experiment with the number and position of the LED arrays to eventually optimize light illumination and thereby increase imaging depth, a new set-up had to be designed. This set-up had to enable rotation, lateral and axial movement of the LED arrays. Moreover, the LED arrays must be able to be placed as close to the transducer and each other as possible, since the path of the light to the absorbing target should be as short as possible. If this path is too long, the light will already have been absorbed by the phantom solution before it reaches its absorbing target. Thus, the following demands hold

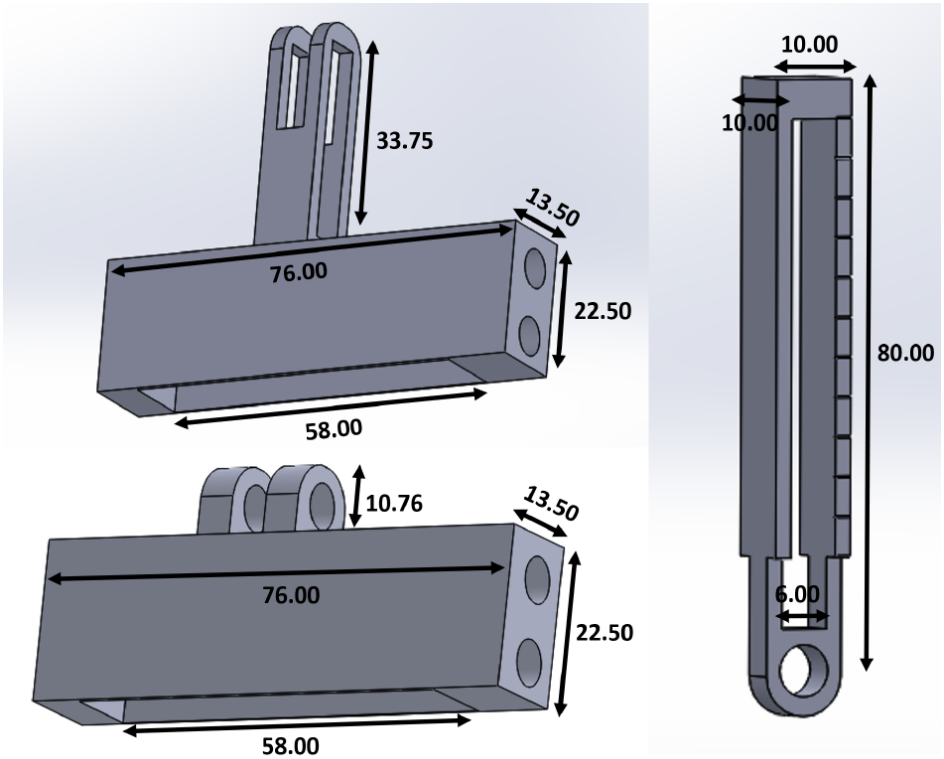

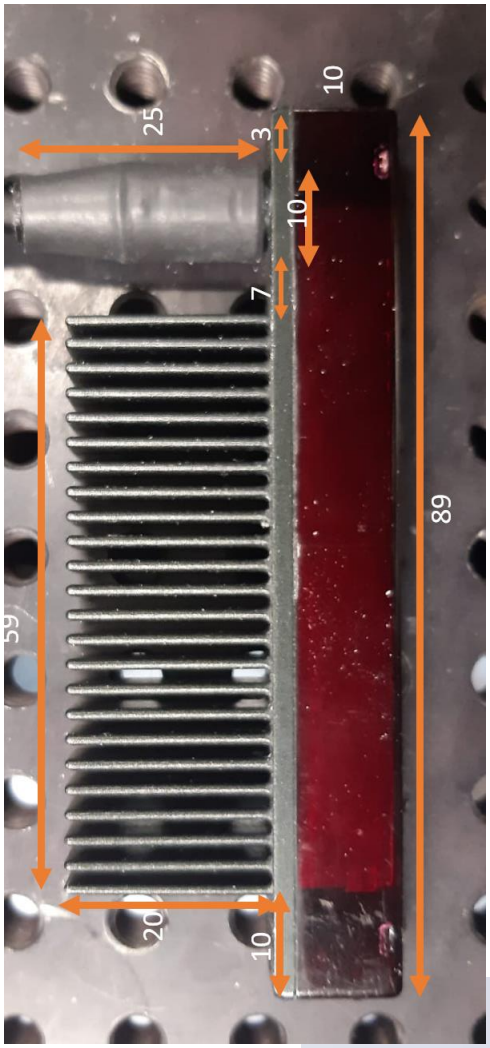
25
3
10
10
7
89
59
20
10

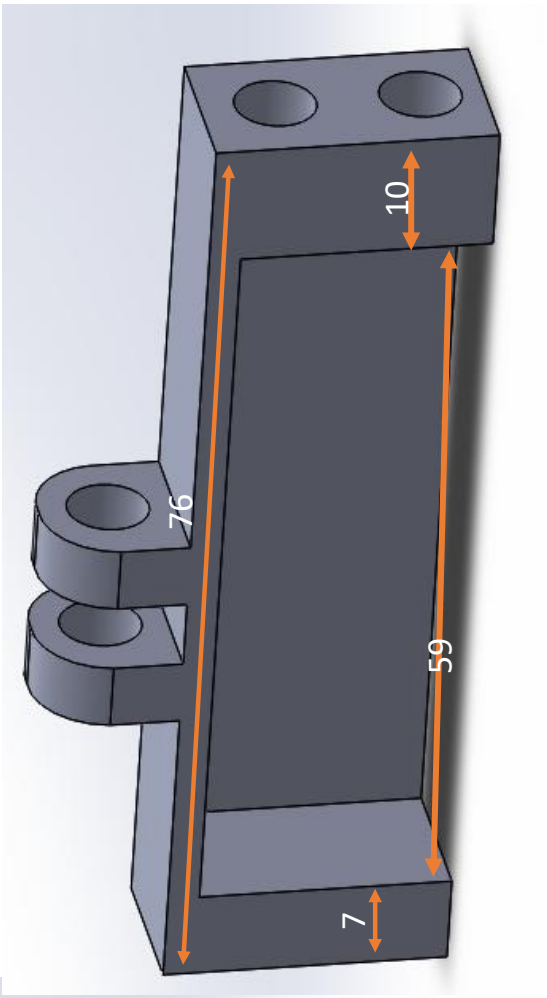
10
76
59
7

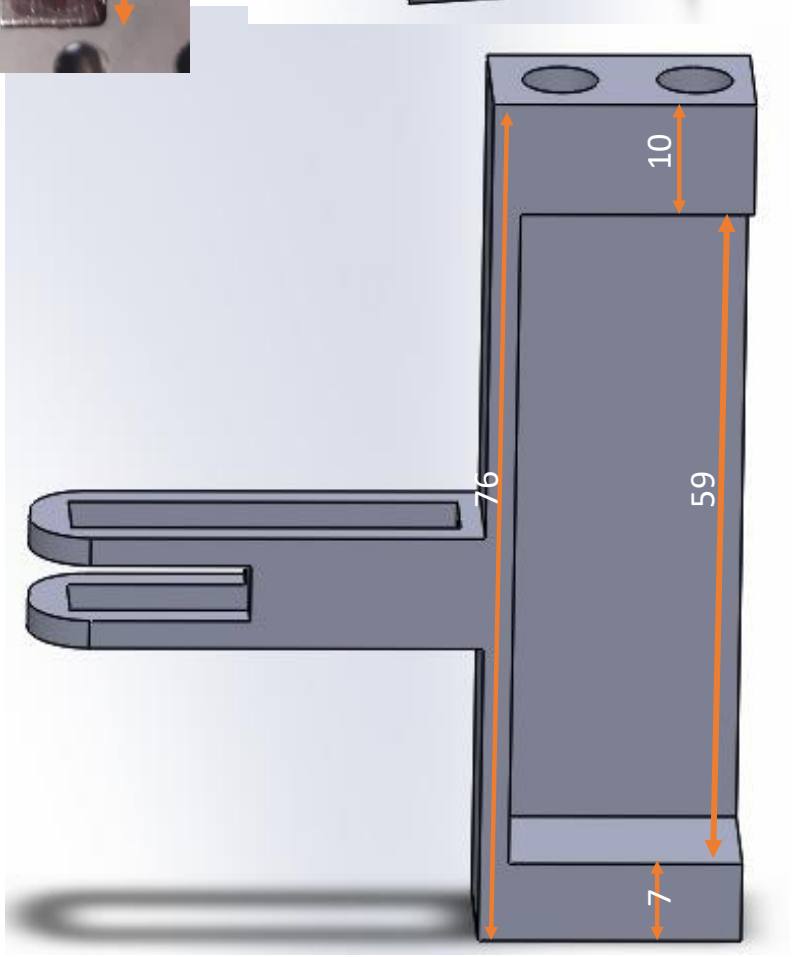
10
76
59
7

General idea: rails on both sides of the transducer. Adjusting the LED array in vertical, horizontal and diagonal direction.

1. Head of screw
2. Bolt at end of screw
3. “Long rod”
4. “Short rod”

5. LED array holder
6. LED array
7. Transducer
8. Screw

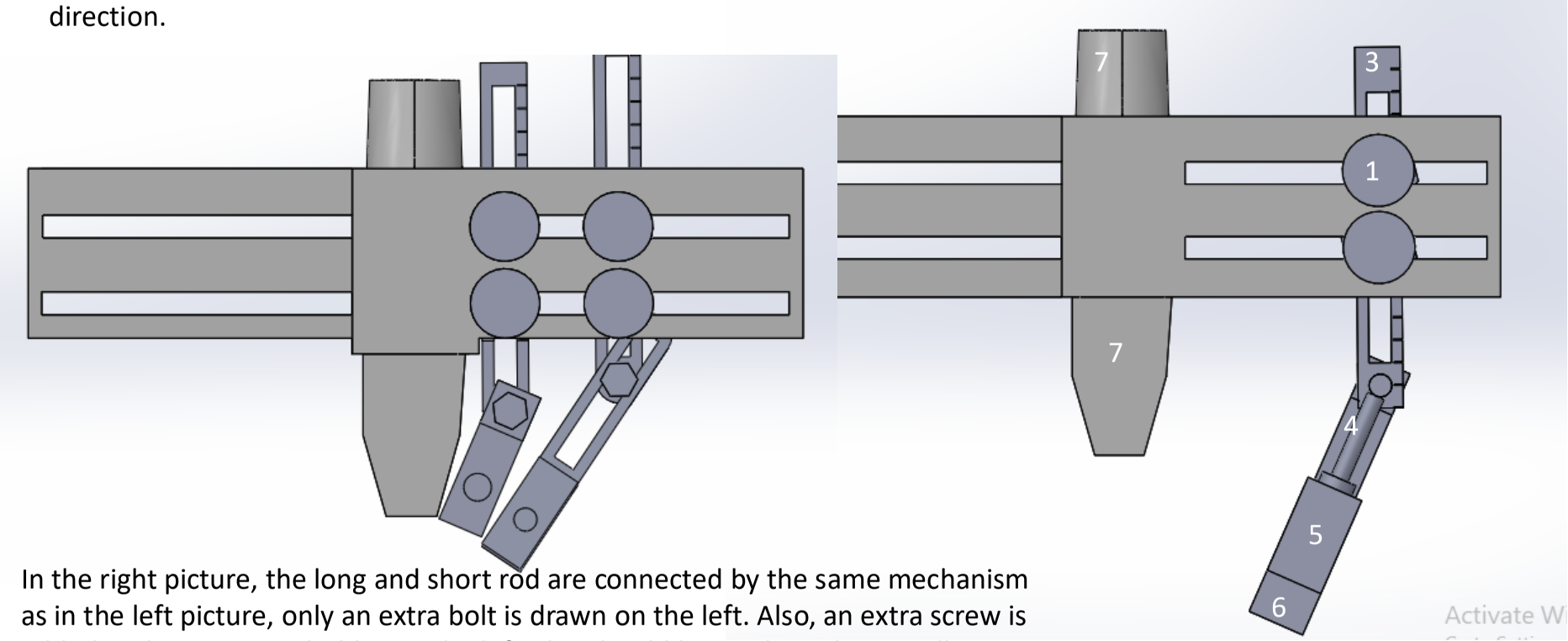

In the right picture, the long and short rod are connected by the same mechanism as in the left picture, only an extra bolt is drawn on the left. Also, an extra screw is added in the LED array holder on the left, this should be on the right as well.

Version 1: hold the long bars by clamping them with a screw and bolt.

1. Head of screw
2. Bolt at end of screw
3. “Long rod”
4. “Short rod”
5. LED array holder
6. LED array
7. Transducer
8. Screw

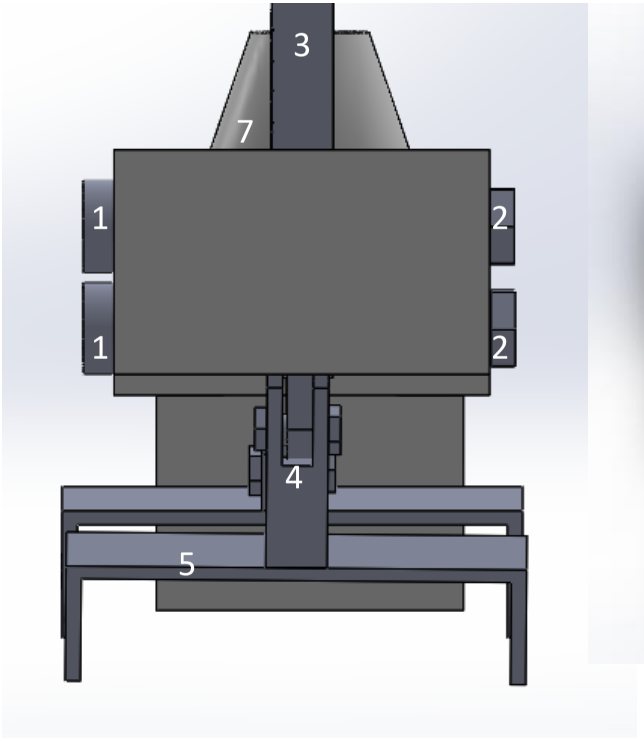

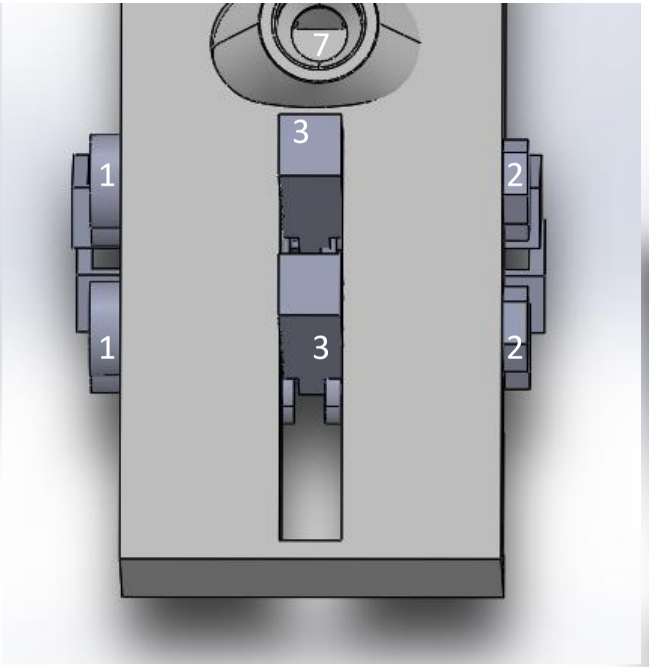

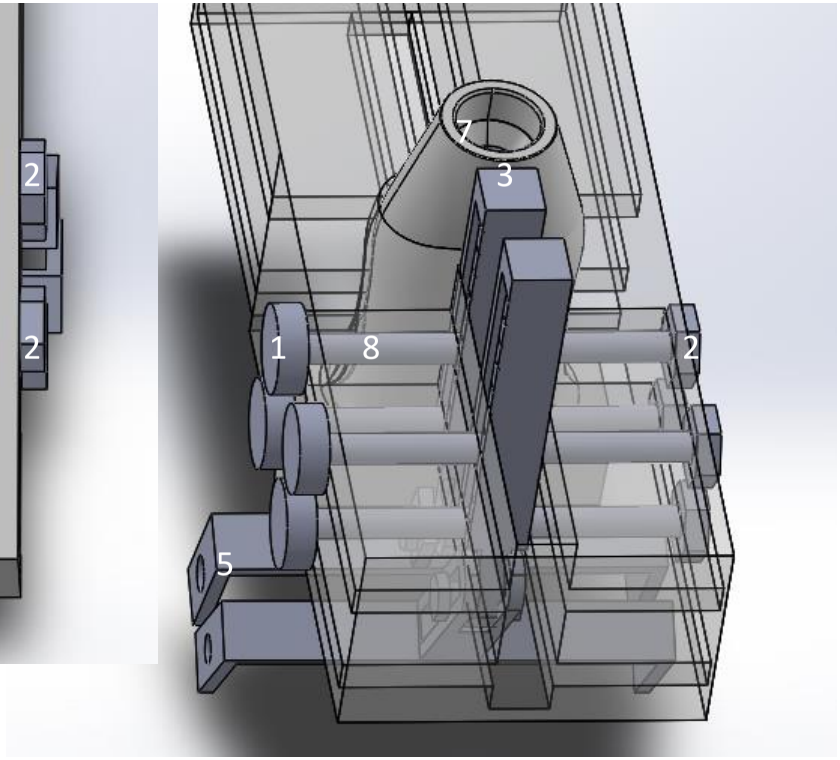

Version 2: hold the long bars by using a lead screw visualized as a screw with a bolt in the middle. The space where the long rod is placed is increased by 3 mm.

1. Head of screw
2. Bolt at end of screw
3. “Long rod”
4. “Short rod”
5. LED array holder

6. LED array
7. Transducer
8. Screw
9. Bolt visualizing the ‘platform’ of the lead screw

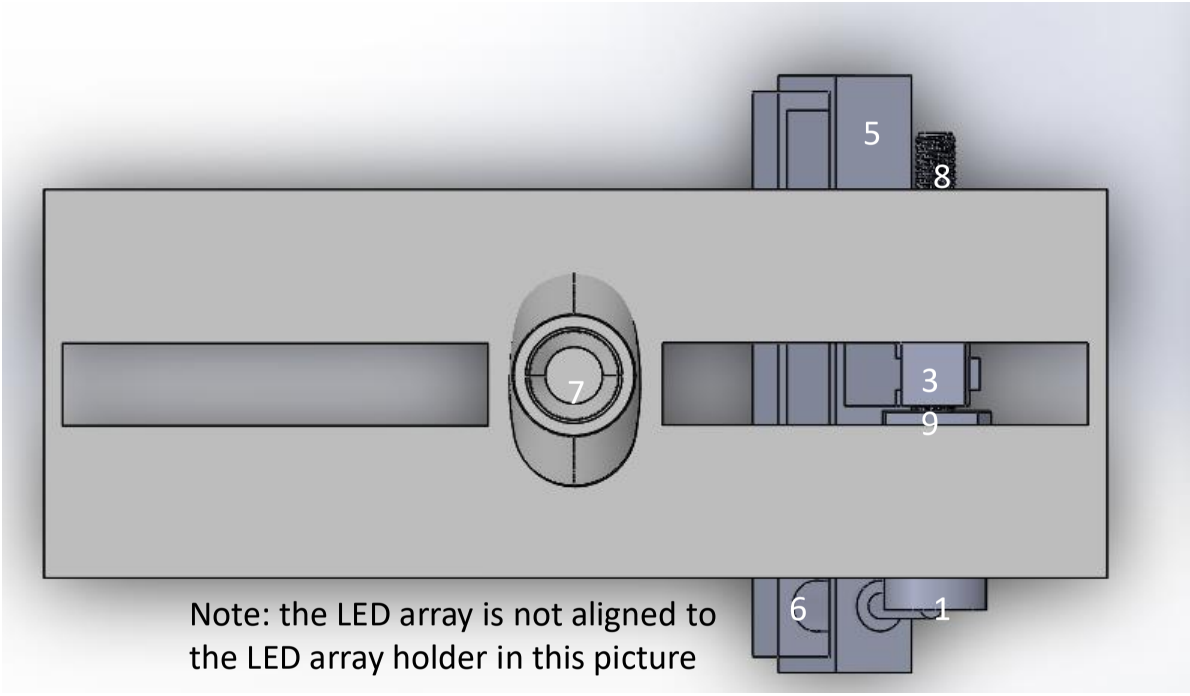

Note: the LED array is not aligned to the LED array holder in this picture

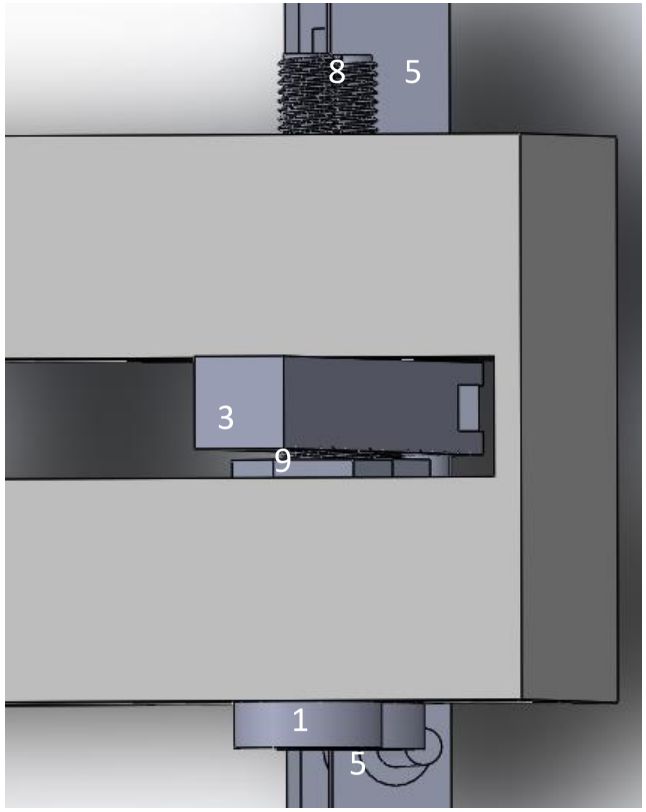

How to connect the outer LED array: I made a slot so that the short rod of the outer array can move up and down while moving diagonally. This way, the outer array can 'bend' around the inner array.

1. Head of screw
2. Bolt at end of screw
3. "Long rod"
4. "Short rod"
5. LED array holder
6. LED array
7. Transducer
8. Screw
9. Bolt visualizing the 'platform' of the lead screw

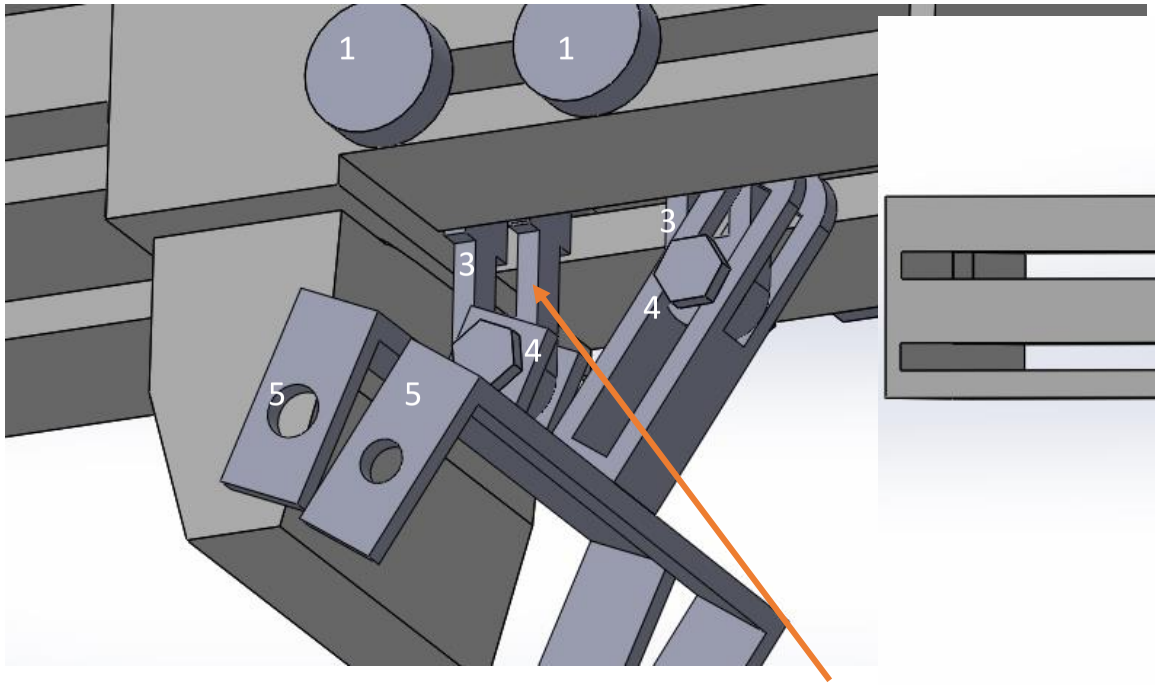

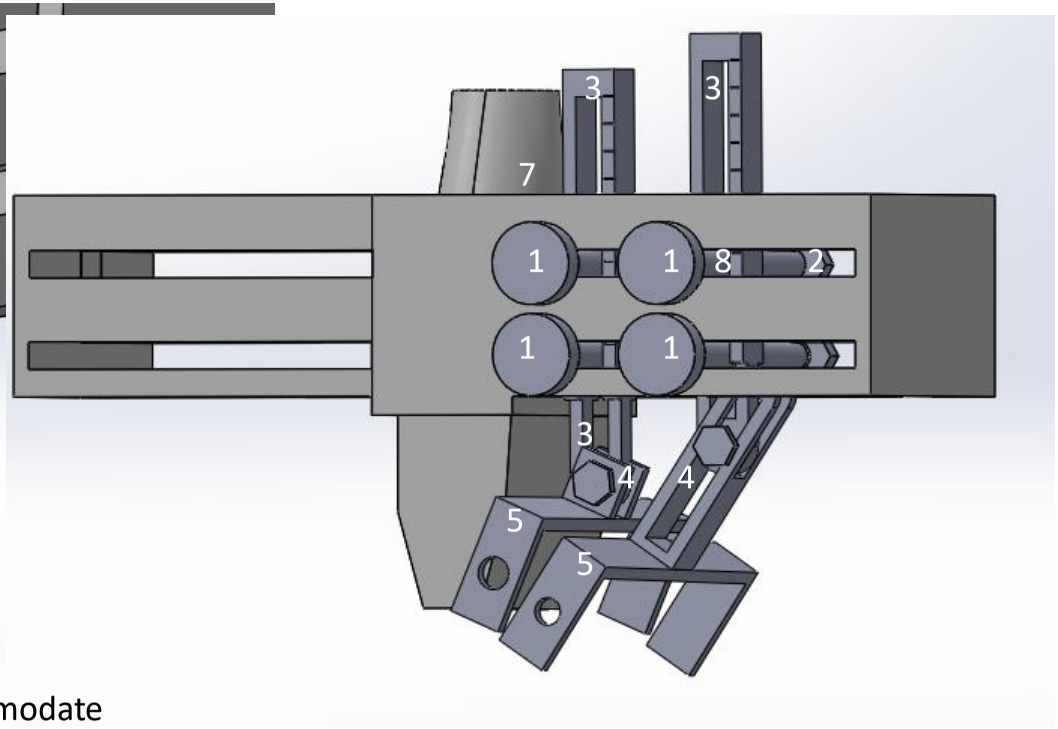

The long rod has a thinner part at the bottom to accommodate the rotating short rod of the outer LED array.

Appendix C

Phantom production

In order to make a phantom solution mimicking tissue, first the absorption coefficient of India Ink was calculated using various dilutions. Then, the percentage of India Ink necessary in the solution was calculated and the phantom solution was made.

C.1 Absorption coefficient India Ink

Since different batches of India Ink have slightly deviating absorption coefficients, the absorption coefficient of the batch used in the making of the phantom had to be calculated. This is done by measuring the absorption of a diluted sample of India Ink with Milli Q water. The India ink is diluted to form a solution that will be called solution 1. That solution consist of 810 l Indiana Ink with 90 ml Milli Q water. From this solution, 5 ml is taken, which is diluted with 45 ml Milli Q water. From this second solution, the absorbance is measured using a spectrophotometer and cuvettes. For a wavelength of 850 nm, the absorbance (A) of the second solution is 2.284. Using the equation, the absorption coefficient a2 of the second solution is calculated.

$$\mu_{a2} = \frac{ln(10^{A})}{t} = \frac{ln(10^{2.284})}{10} = 0.53mm^{-1} \tag{C.1}$$

Here a2 is the absorption coefficient of solution 2 inmm^{-1}, A is the absorbance and t is the thickness of the cuvette in mm. In this case, the cuvette was 10 mm. From this absorption coefficient, the absorption coefficient of the non-diluted India Ink is calculated. This is done by dividing the absorption coefficient of solution 2 by the concentration of solution 2. The concentration of solution 2, C2, is the amount of India Ink in this solution divided by the total volume of this solution:

$$C_2 = \frac{V_{ink}}{V_2} \tag{C.2}$$

The volume of the ink in solution 2 is calculated by multiplying the concentration of ink in solution 1 by the volume of solution 1 that was used to make solution 2. The concentration of Indiana Ink in solution 1, C1, is the volume of ink that is added, divided by the total volume of the solution.

$$C_2 = \frac{C_1 V_{1in2}}{V_2} = \frac{\frac{V_{ink1}}{V_1} V_{1in2}}{V_2} = \frac{\frac{V_{ink1}}{V_1} V_{1in2}}{V_2} \tag{C.3}$$

Here V1 is the total volume of solution 1, and V2 the total volume of solution 2. V1in2 is the volume of solution 1 that was used for solution 2. The absorbance A of the India Ink is:

$$A_{ink} = \frac{A}{C_2} \tag{C.4}$$

So the absorption coefficient μ_a of the India Ink is:

$$\mu_{aink} = \frac{ln(10^A)}{t} = \frac{ln(10^{2566.29})}{10} = 590.9 mm^{-1} \tag{C.5}$$

C.2 Mimicking absorption of tissue

For blood, the absorption coefficient taken is 0.40mm^{-1} [53]. In order to mimic this absorption in a phantom, Indiana Ink is added. The percentage India Ink that should be added in the phantom solution is:

$$\%_{ink} = \frac{1}{\frac{\mu_{aink}}{\mu_{blood}}} \cdot 100 \tag{C.6}$$

However, when this phantom was used in the chicken breast experiment, the absorption was too little to generate sufficient photoacoustic signal. Therefore, a solution with an absorption coefficient of 1.0 mm^{-1} was produced. For muscle, the absorption coefficient is 0.03 mm^{-1}at a wavelength of 850 nm [54]. The percentage India Ink that should be added in the phantom solution is 0.0051%

The final phantom solution was made by adding 225 l India Ink in 4 litres of MQ (0.0056%). The absorption coefficient was a = 0.033mm^{-1}

C.3 Mimicking scattering of tissue

To mimic the scattering in a tissue phantom, an Intralipid solution is used. This Intralipid is diluted by water. To calculate the percentage Intralipid of which the phantom solution should eventually exist out of, a calculation based on [55] is used. First, the anisotropy factor g is approximated by a linear function:

$$g = y_0 + a_g + \lambda \tag{C.7}$$

Here y_0 is the y-intercept, a_g the slope and λ the applicable wavelength, in this research 850 nm. Next, the scattering coefficient is approximated by a power function:

$$\mu_s = a_s \lambda^b \tag{C.8}$$

Here a_s is a coefficient and b the exponent. The value of the reduced scattering coefficient is calculated using

$$\mu_s' = \mu_s \cdot 10 * (1 - g) \tag{C.9}$$

The concentration Intralipid then follows from dividing the desired reduced scattering coefficient by the calculated reduced scattering coefficient from the Intralipid 20%. The values for y0, ag, as and b for Intralipid 20% can be seen in table C.1 [55]

Table C.1: Parameters for the calculation of the percentage Intralipid 20% needed to mimic scattering in a phantom solution. [55]

Parameter	Value
y_0	1.09
a_g	-6.81210^{-4}
a_s	3.87310^{8}
b	-2.397

For blood, the reduced scattering coefficient 0 s is 12.6 $cm^{-1}$for a wavelength of 850 nm [53]. To mimic scattering at a wavelength of 850 nm, 7.0% of the phantom volume should consist of Intralipid.

For muscle, the reduced scattering coefficient 0 s is 6.67 cm^{-1} at a wavelength of 850 nm [54]. Therefore, 3.7% of the phantom volume should consist of Intralipid.

Appendix D

Dataset examples

In this section, a small selection of the ground truth images in the two datasets; Drive dataset and NNE dataset are displayed, to give an impression what type of images are included in both datasets.

D.1 Drive

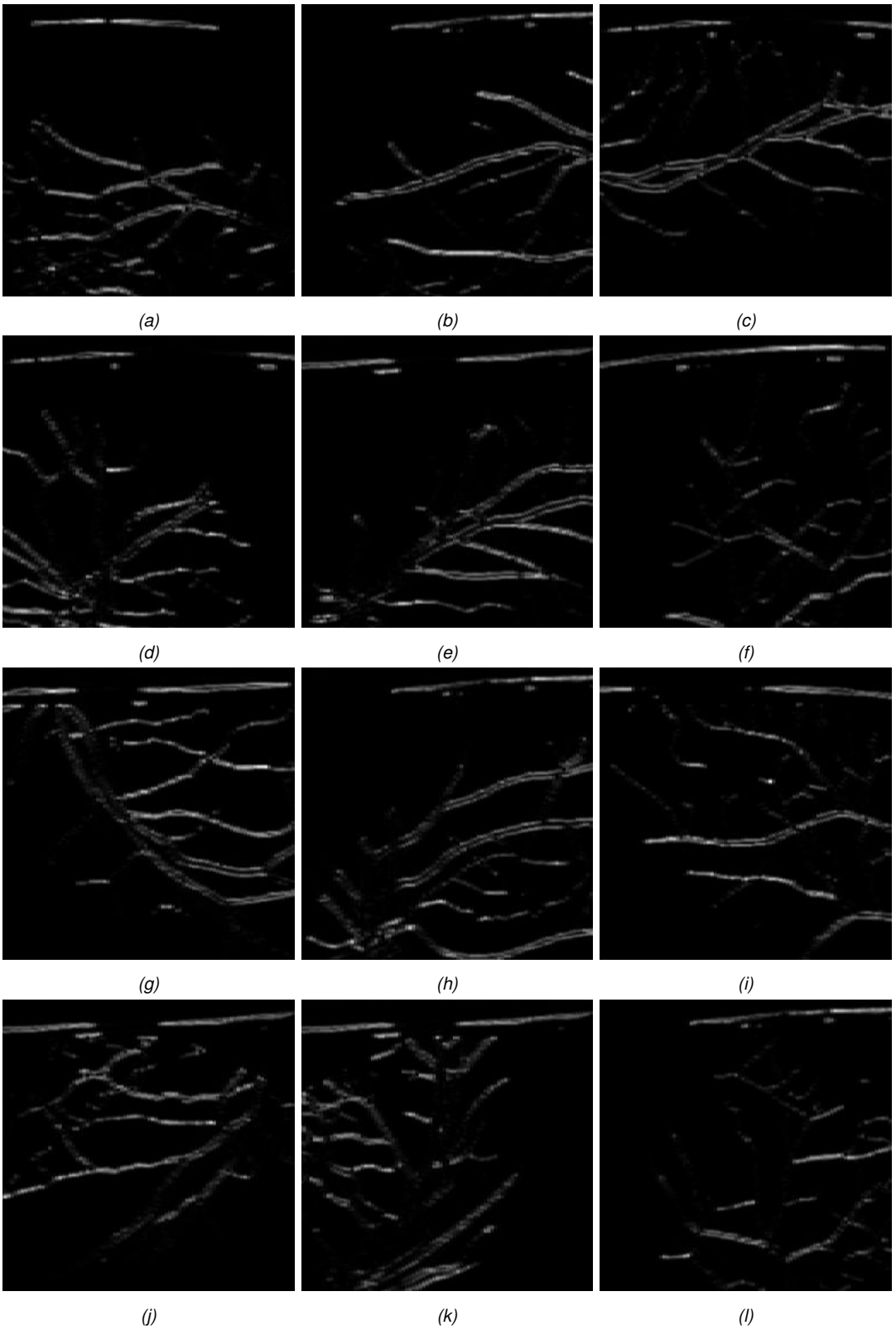

Figure D.1: Photoacoustic ground truth images generated from Drive dataset

D.2 NNE

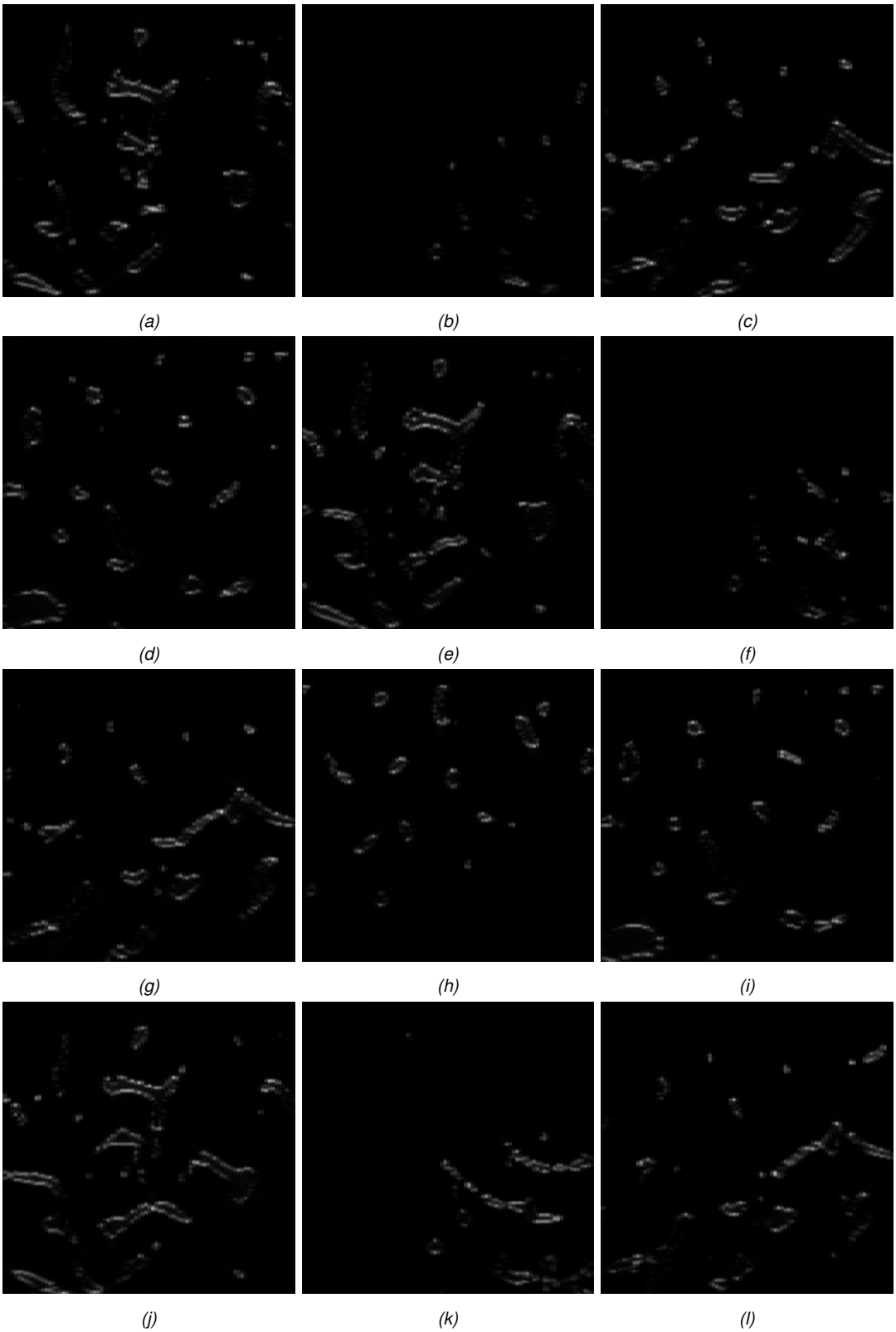

Figure D.2: Photoacoustic ground truth images generated from NNE dataset

Appendix E

Results experimental validation of GANs algorithm

In this section, the resuts of the validation experiment are shown. The experiment was excecuted for 4 different noise levels. All figures show on the right the signal of the PA system in water, in the middle the signal from the PA system in a tissue mimicking phantom and on the right the predicted image by the GANs algorithm.

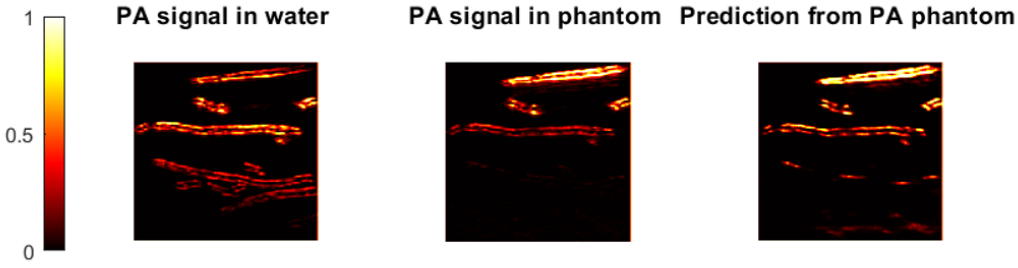

Figure E.1: P1 Averaging: 6400, gain water, 65 gain phantom 75

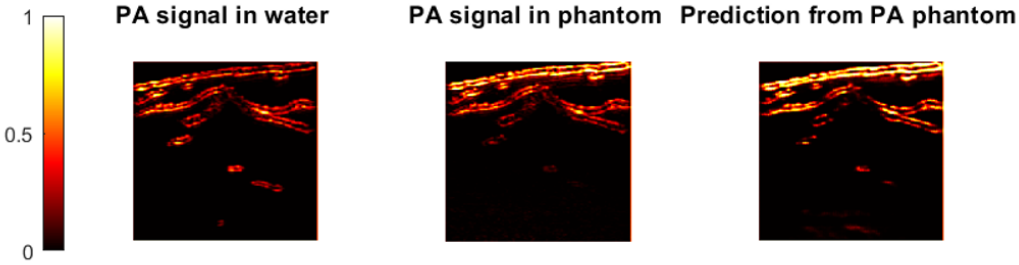

Figure E.2: P2 Averaging: 6400, gain water, 65 gain phantom 75

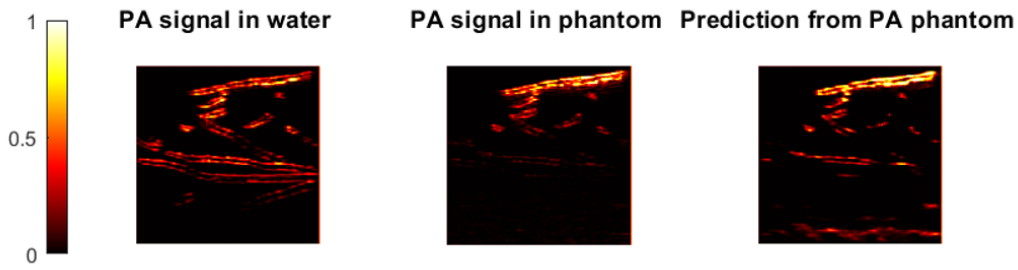

Figure E.3: P3 Averaging: 6400, gain water, 65 gain phantom 75

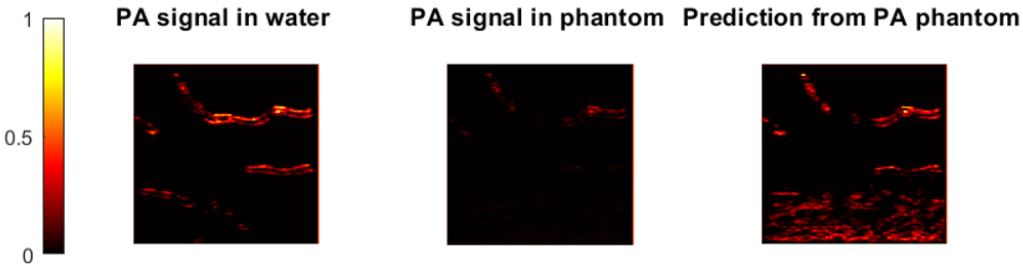

Figure E.4: P8 Averaging: 6400, gain water, 65 gain phantom 75

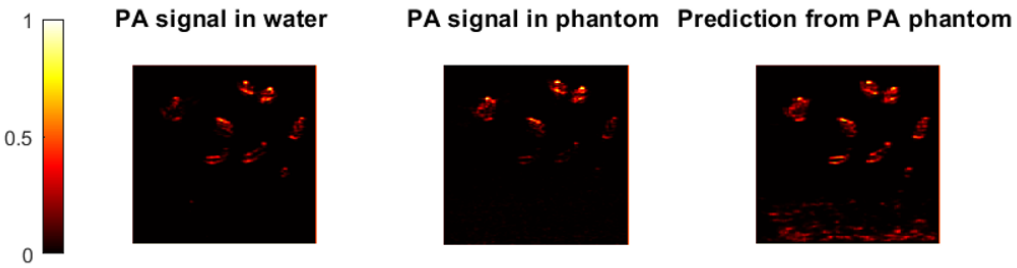

Figure E.5: P9 Averaging: 6400, gain water, 65 gain phantom 75

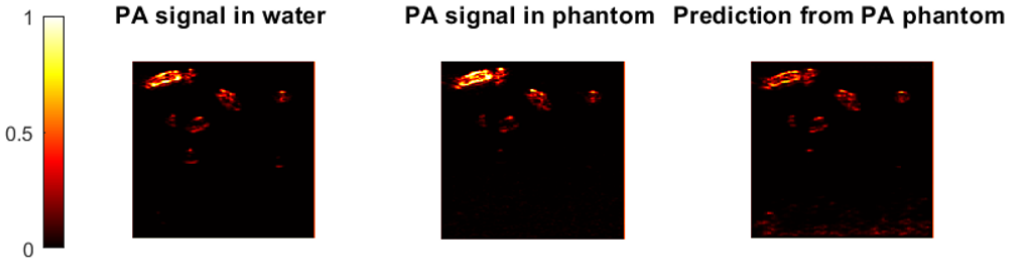

Figure E.6: P11 Averaging: 6400, gain water, 65 gain phantom 75

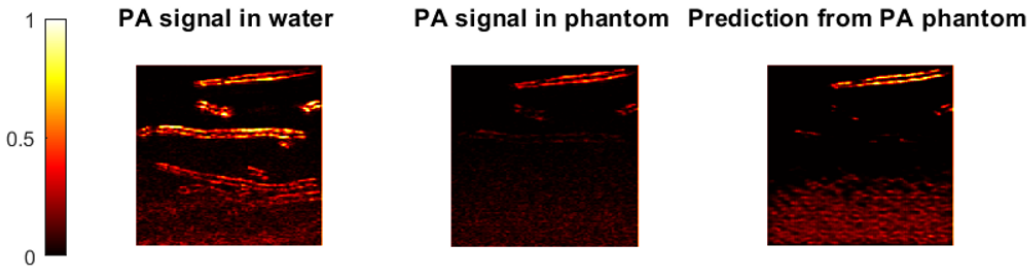

(a) averaging 128

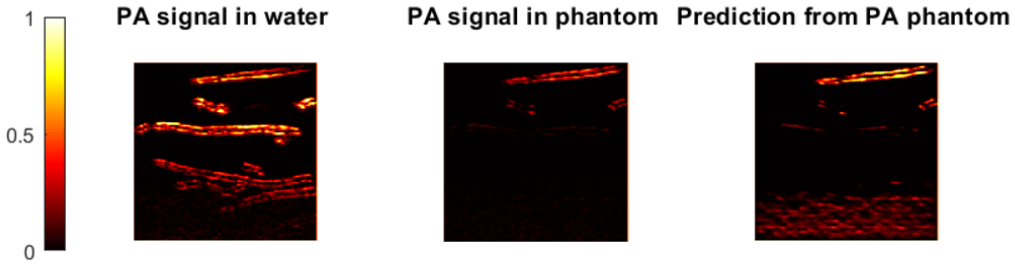

(b) averaging 384

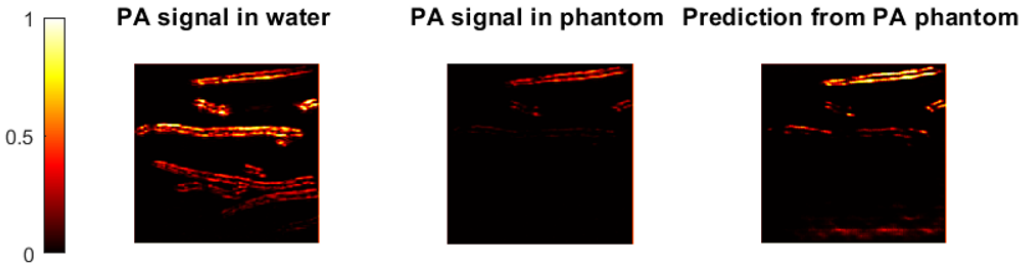

(c) averaging 1280

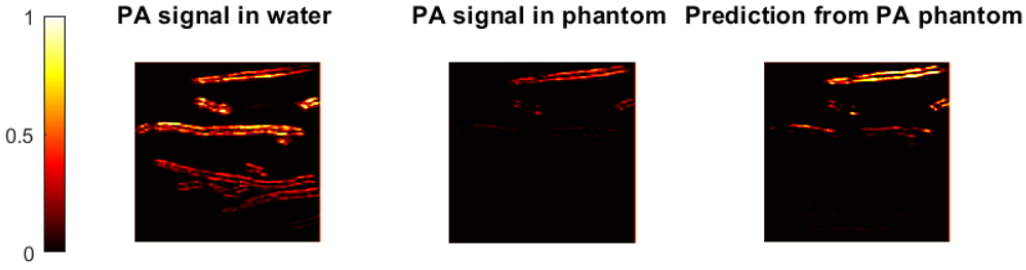

(d) averaging 6400

Figure E.7: P1

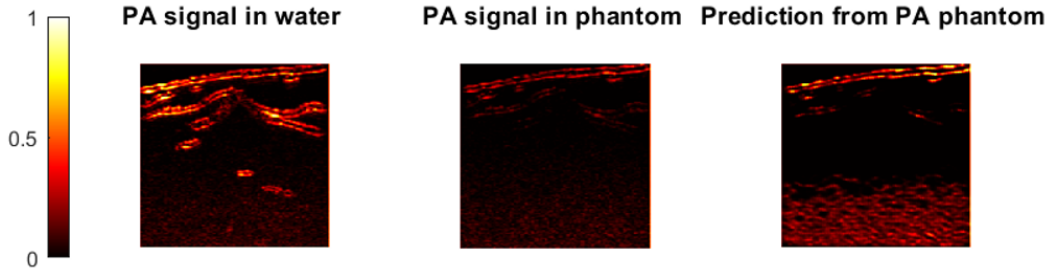

(a) averaging 128

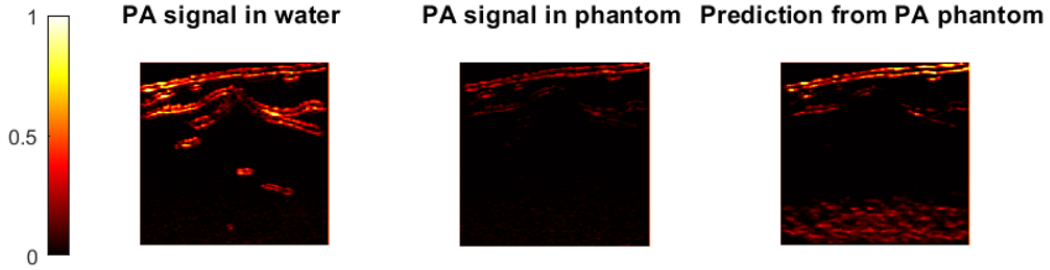

(b) averaging 384

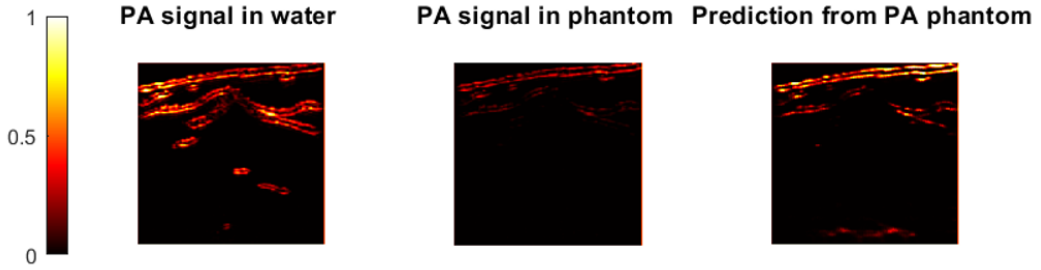

(c) averaging 1280

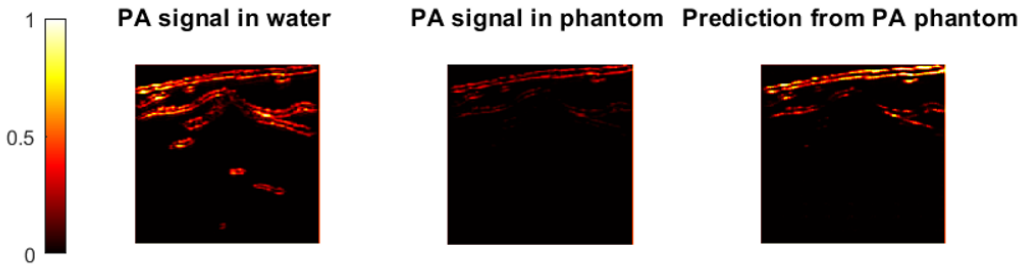

(d) averaging 6400

Figure E.8: P2

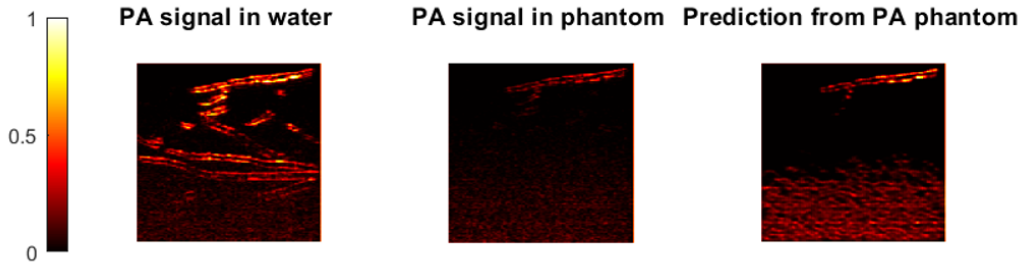

(a) averaging 128

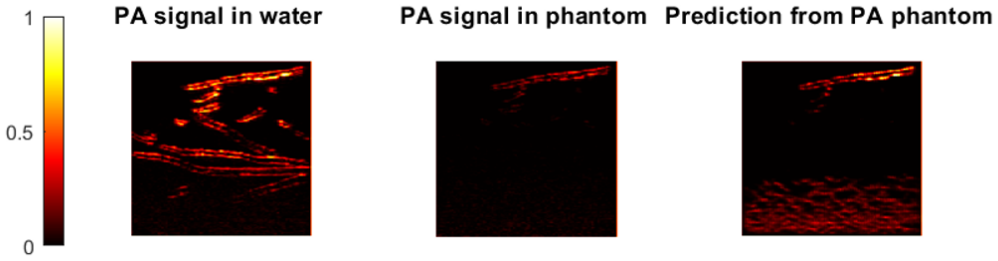

(b) averaging 384

(c) averaging 1280

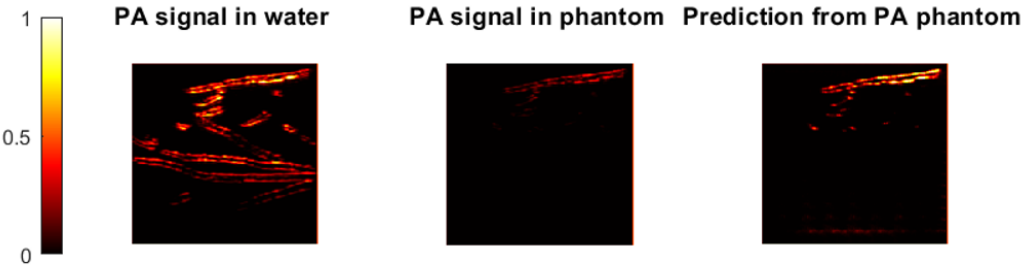

(d) averaging 6400

Figure E.9: P3

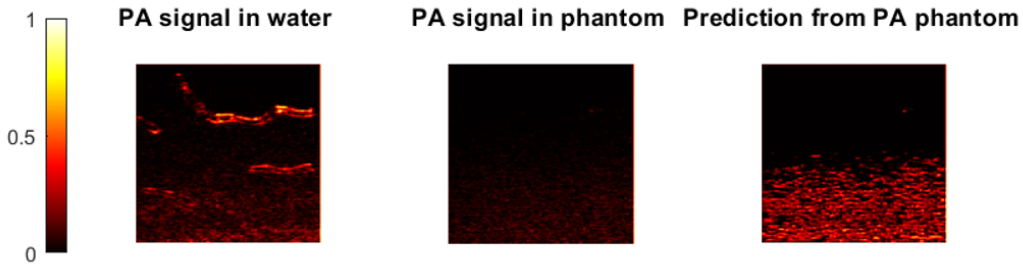

(a) averaging 128

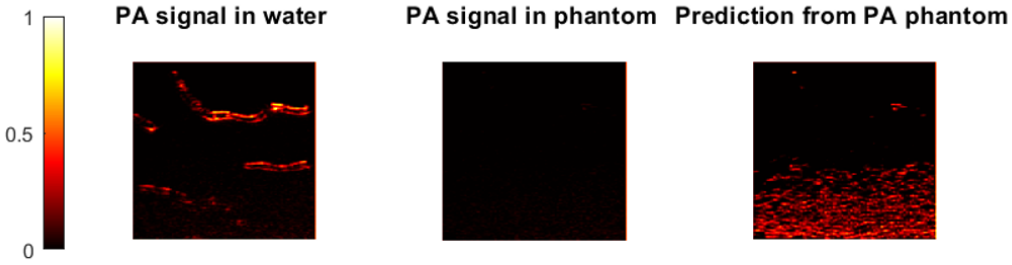

(b) averaging 384

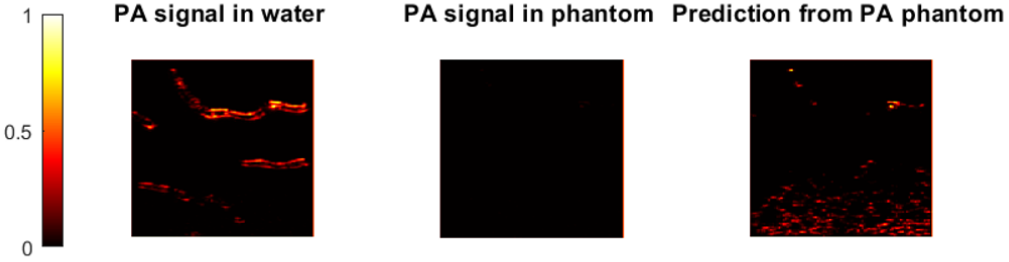

(c) averaging 1280

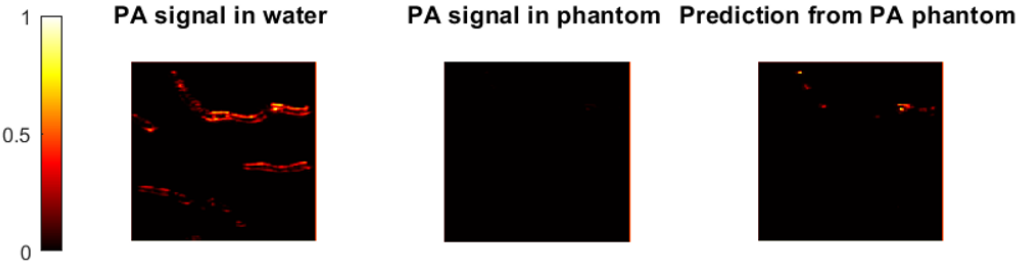

(d) averaging 6400

Figure E.10: P8

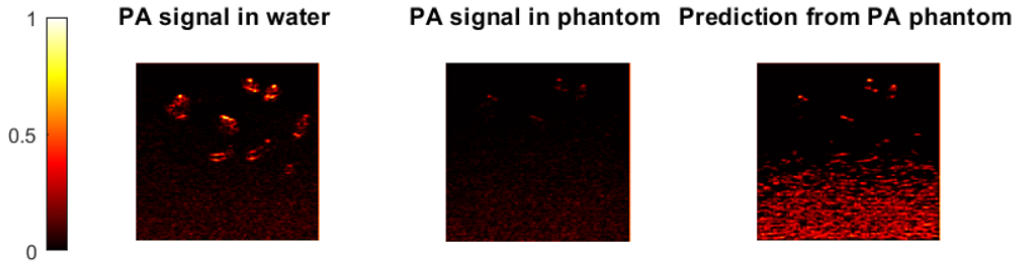

(a) averaging 128

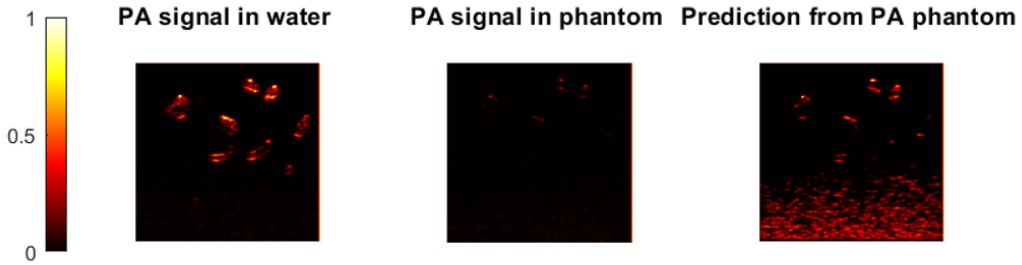

(b) averaging 384

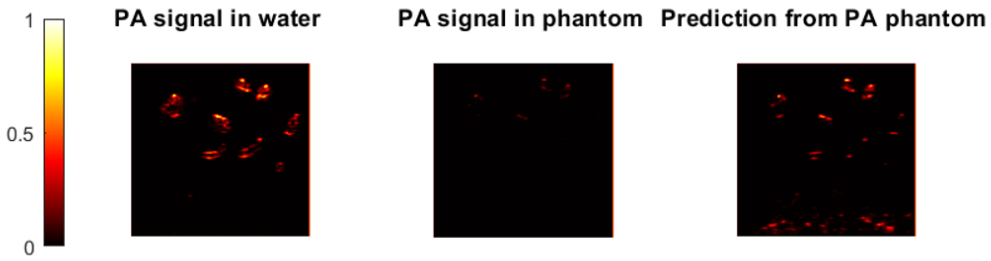

(c) averaging 1280

(d) averaging 6400

Figure E.11: P9

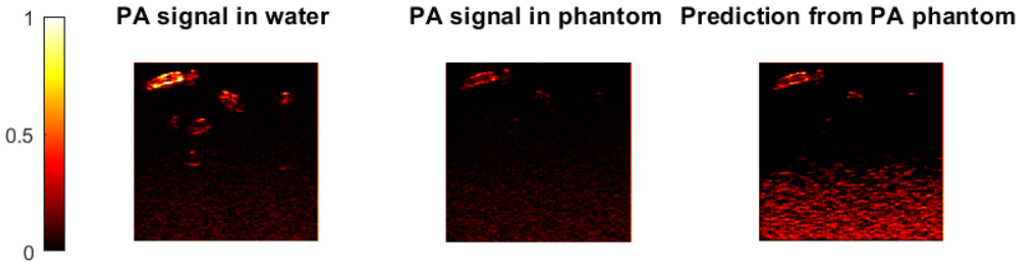

(a) averaging 128

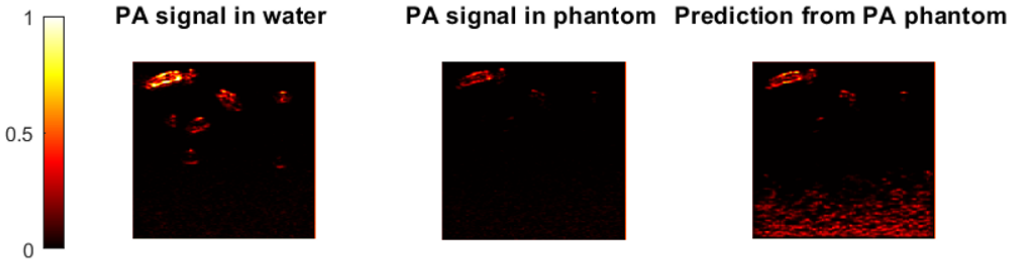

(b) averaging 384

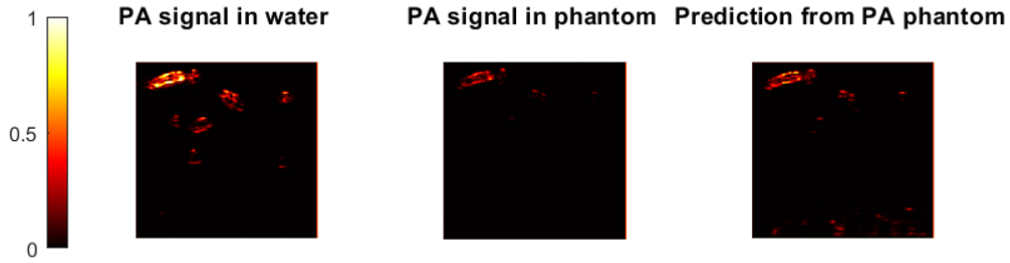

(c) averaging 1280

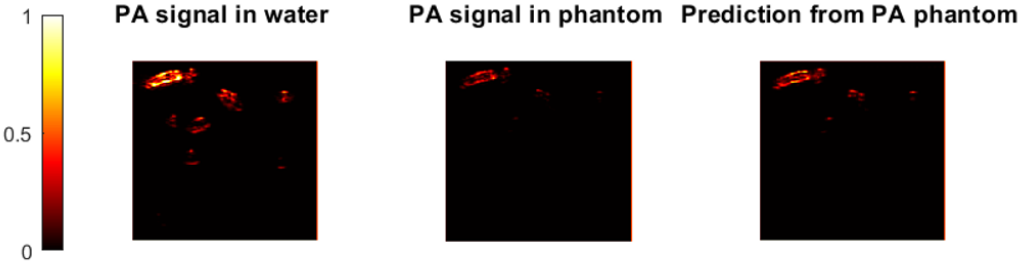

(d) averaging 6400

Figure E.12: P11